The Dissertation Committee for Meike Hauschildt certifies that this is the approved version of the following dissertation:

Statistical Analysis of Electromigration Lifetimes and Void Evolution in Cu Interconnects

Committee:

Paul S. Ho, Supervisor

Desiderio Kovar

Jack C. Lee

Llewellyn K. Rabenberg

Martin Gall

Statistical Analysis of Electromigration Lifetimes and Void Evolution in Cu Interconnects

by

Meike Hauschildt, M.S.

Dissertation

Presented to the Faculty of the Graduate School of
The University of Texas at Austin
in Partial Fulfillment
of the Requirements
for the Degree of

Doctor of Philosophy

The University of Texas at Austin
May 2005

Dedication

To my parents

Acknowledgements

First of all, I would like to express my gratitude to Professor Paul S. Ho for his guidance and support throughout my research work at the Laboratory for Interconnect and Packaging. I am deeply impressed by his ability to identify research topics that are technologically important as well as feasible. His positive spirit helped me significantly during several more difficult periods of this study. Additionally, I am very thankful for the opportunities given to me to present my research to the reliability community, which would have been impossible without his support.

I am greatly indebted to Freescale Semiconductor for the generous support of this research. Most importantly, Dr. Martin Gall provided constant guidance and support towards the completion of this work. He never hesitated to spend extra time discussing details of EM statistics. His vision made this work possible as well as enjoyable. I also thank him for serving on my dissertation committee. Furthermore, I truly appreciate the help of Dr. Patrick Justison, Stacye Thrasher and Richard Hernandez, who taught me a great deal about the details of EM experiments and analysis. I enjoyed all the time spend with them. Without the help of Dr. Lynne Michaelson and Matt Herrick this work would have been impossible for they were always ready to supply the right kind of samples as well as fruitful discussions and new ideas. I am grateful for their extraordinary help and friendliness. I want to thank Dr. Hisao Kawasaki and Dr. Koneru Ramakrishna for their support during this work.

I want to acknowledge the members of the Interconnect and Packaging group for helpful discussions and support. At the initial stages of my studies, the help of Dr. Ennis Ogawa was irreplaceable. From him, I have learned how to conduct research work properly. I am trying to follow his careful and thorough ways of always questioning every detail of the experiment. Special thanks to R. Scott Smith and Jo Ann Smith for being there for me.

I would like to thank Professor Llewellyn K. Rabenberg for teaching me transmission electron microscopy and for serving on my dissertation committee. Likewise, I want to thank Professor Desiderio Kovar and Professor Jack C. Lee for serving on my committee as well.

Finally I would like to thank my parents, my sisters and Milos for continuous support and love. Without their encouragement, the doctoral degree would have never become a reality. I send them a very special thank you.

Statistical Analysis of Electromigration Lifetimes and Void Evolution in Cu Interconnects

Publication No._____________

Meike Hauschildt, Ph.D.
The University of Texas at Austin, 2005

Supervisor: Paul S. Ho

The introduction of Cu and low-k dielectric materials and continuing scaling of on-chip interconnects raise reliability concerns on electromigration. Failures occur mainly by void growth at the line end. The corresponding failure times usually follow a lognormal distribution with the median lifetime depending on the quality of the interface, which controls the mass transport. Since electromigration experiments are conducted at higher current densities and temperatures compared to operating conditions, extrapolations are needed to assess reliability at operating conditions. The extrapolated lifetimes depend exponentially on the lognormal standard deviation sigma. The objective of this study is to identify intrinsic parameters that control the electromigration statistics and failure mechanism in Cu interconnects. To accomplish this task, lifetimes, void evolution and void size distributions were analyzed in detail as a function of failure criterion. Experiments were performed on 0.18μm wide Cu interconnects with tests terminated after certain amounts of resistance increases, or after a specified test time. Void size distributions of resistance-based and time-based electromigration tests were obtained using microscopy. The lifetime and void size distributions were found to follow lognormal distribution functions. The sigma values of these distributions decrease with increasing test time. The statistics of resistance-based void size distributions can be simulated by considering geometrical variations of the void shape. In contrast, the characteristics of time-based void size distributions require consideration of kinetic aspects of the electromigration process. For this purpose, a model was developed including geometrical and experimental factors of the electromigration test, as well as kinetic aspects of the mass transport process, such as differences in interface diffusivity between the lines. The variation in diffusivities at the line ends arises from differences in the interface structure as a result of varying Cu grain orientations. It will be shown that the statistics of electromigration lifetime distributions can be adequately modeled by combining the time-based and resistance-based void area measurements. To examine the validity of the model describing electromigration lifetime statistics, the effect of various process changes was analyzed. These include a variation in line height, a change in capping layer, and a comparison between single and dual damascene structures.

Table of Contents

List of Tables

List of Figures

Chapter 1: Introduction

The need for higher performance of modern integrated circuits leads to a continuous trend of ever increasing device density. As a result, the density of on-chip interconnects increases to establish the needed communication paths between devices. This, in turn, requires a decrease in both interconnect width and thickness. As a consequence, the operational current densities increase from generation to generation. Figure 1.1 represents the expected trend in current density at 105°C operating temperature, according to the 2004 International Technology Roadmap for Semiconductors [ITRS 2004].

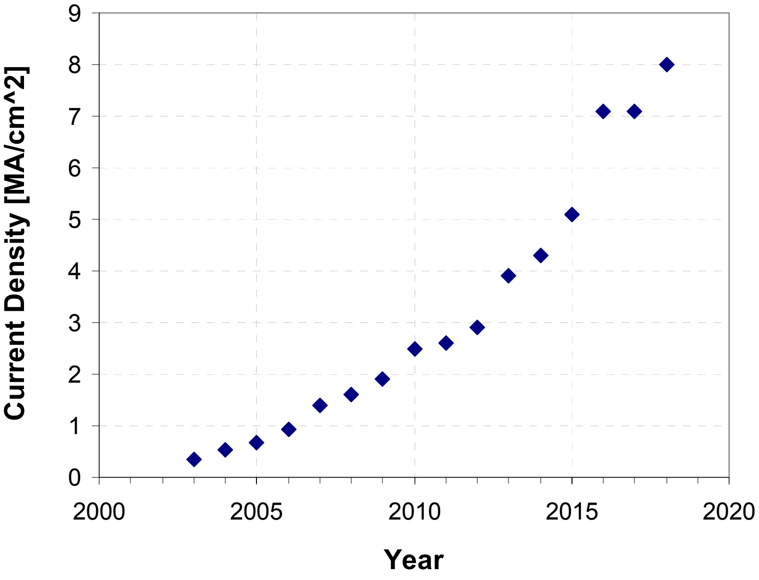

Figure 1.1 The current density as a function of year according to the ITRS 2004. The increase in operational current density with technology generation leads to an ever increasing driving force for EM in interconnects.

This continuing scaling of on-chip interconnects raises reliability concerns on electromigration (EM) and stress-induced voiding (SIV). With the current density in interconnect lines increasing, the driving force for EM constantly rises. Thus, the EM reliability concern is getting worse with every new chip generation. As a consequence, Cu has been introduced as the metallization of choice, replacing traditional Al(Cu)-based interconnects [Edelstein 1997, Venkatesan 1997]. Its superior EM resistance is accompanied by reduced specific resistivity, which improves the RC-delay. This quantity, describing the combination of resistance and capacitance for a specific interconnect architecture, is an important factor in achieving superior device performance. In addition to a reduction in resistivity, intra- and inter-layer capacitance is decreased through the introduction of low-permittivity (low-k) dielectrics. Due to the inferior thermo-mechanical properties of low-k materials, compared to traditional SiO_2-based dielectrics, new reliability concerns arise.

EM failures in Cu interconnects occur mainly by void growth at the cathode end of the line. With continuing void growth, the line resistance increases, eventually leading to failure of the line. The corresponding failure times usually follow a lognormal distribution with the median lifetime depending on the quality of the interface, which controls the mass transport [Hu 1999, Arnaud 2000, Hau-Riege 2001, Ogawa 2002b, Meyer 2002, Zschech 2004, Hauschildt 2004a, Hauschildt 2004b]. Since EM experiments are conducted at higher current densities and temperatures compared to operating conditions, extrapolations are needed to assess reliability at operating conditions. In addition, only a limited number of lines are being tested, whereas hundreds of millions of interconnects exist on each chip. Hence, the extrapolation needs to take into account how to assess on-chip reliability from the EM-tested sample population. The following equation, based on Black's initial work on EM [1969], describes the dependence of time-to-failure under operating conditions, TTF_{oper}, on experimental parameters:

$$TTF_{oper} = MTTF_{stress}\left({I_{stress}}\Big/{I_{oper}} \right)^{n} \exp\left[\frac{E_a}{k_B}\left(\frac{1}{T_{stress}} - \frac{1}{T_{oper}} \right) + N_{stdev}\sigma \right] \qquad (1.1)$$

where $MTTF_{stress}$ is the median time-to-failure as obtained in an EM experiment, I_{stress}, I_{oper} and T_{stress}, T_{oper} the currents and temperatures used during the EM test and under operating conditions, respectively, E_a the activation energy, k_B Boltzmann's constant, N_{stdev} the number of standard deviations and σ the lognormal standard deviation obtained from the EM experiment. The parameter n represents the current density exponent, which is close to 1 for Cu interconnects [Hu 1999, Rosenberg 2000]. The variable N_{stdev} is needed to extrapolate the time-to-failure value of very small failure percentiles, such as 0.01%, under operating conditions from the experimentally obtained 50% time-to-failure. Furthermore, it provides a link between the number of EM-tested samples and the on-chip interconnect population. As can be seen from Equation (1.1), the extrapolated lifetimes depend linearly on the measured median lifetime and exponentially on the activation energy of the diffusion process and the lognormal standard deviation σ (sigma). Thus, in order to enhance EM performance, these parameters need to be improved. In addition, it becomes clear that the influence of sigma can be more significant than the median lifetime. Figure 1.2 shows a schematic illustration of this effect. Two lognormal distributions with different median and sigma values have been randomly created using the following probability density function:

$$pdf(t) = \frac{1}{\sqrt{2\pi}\sigma t} \exp[-\frac{1}{2}\{\frac{\ln(t) - \ln(t_{50})}{\sigma}\}^2] \qquad (1.2)$$

where t is the time and t_{50} the median time-to-failure (MTTF). When extrapolating to operating conditions, it can be seen that for a time to about 0.1% cumulative failure and below, the distribution with the smaller sigma value is advantageous despite the smaller median time-to-failure. So far, most studies have focused on improving EM performance by increasing the lifetime. However, the exponential influence of sigma is generally neglected.

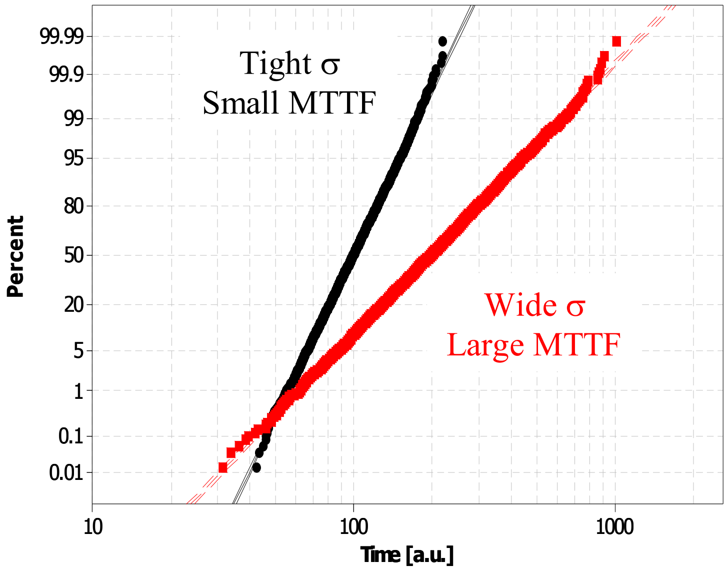

Figure 1.2 Schematic illustrating that the influence of sigma can be more significant than the median lifetime when extrapolating to operating conditions. Two lognormal distributions with different median and sigma values are shown. It can be seen that already for a time to 0.1% cumulative failure the distribution with the smaller sigma value is advantageous despite the smaller median time-to-failure.

Several recent studies have shown that the median lifetime of Cu interconnects can be improved significantly by strengthening the top interface. Such efforts include the insertion of a thin layer of CoWP between Cu and the passivation layer [Hu 2002, Hu 2003a, Hu 2003b, Hu 2004, Zschech 2004], as well as alloying Cu with small percentages of aluminum [Zschech 2004, Meyer 2004]. While these studies focus on reducing interfacial mass transport to improve the lifetime and possibly the activation energy, a better understanding of sigma is still needed. The magnitude of sigma is influenced by variations in processing, i.e. an immature process leads to large sigma values. The question arises whether there are any intrinsic properties of the interconnect which define EM statistics once processing is well controlled.

The objective of this study is twofold: first, to identify intrinsic parameters that control the EM statistics and failure mechanism in Cu interconnects, and second, to develop a kinetic model to evaluate the EM failure statistics taking into account the effect of microstructure on interface mass transport. A proper understanding of the causes for lifetime variations could potentially enable predictions of reliability concerns for future interconnect generations. To accomplish this task, lifetimes, void evolution and void size distributions have been analyzed in detail as a function of failure criterion and test time. In order to formulate the kinetic model, the observed void size and EM lifetime statistics were simulated by considering experimental, process and mass transport parameters.

This manuscript is divided into four major parts. First, the theory of EM and the status of current research activities are reviewed in Chapter 2. Subsequently, details on the experimental procedure as well as the simulation approach used in this study are described in Chapter 3. The third part presents the results obtained in this work. This part is divided into two chapters with Chapter 4 providing experimental data related to the analysis of lifetimes, void evolution and void size distributions. Chapter 5 contains the discussion of the experimental results including simulation results used to explain the observed statistics of void sizes and EM lifetimes. A kinetic model was established incorporating varying diffusivities between interconnects. In the fourth part of this manuscript, Chapter 6, additional experiments performed to study the effect of alternate processing schemes on EM statistics will be discussed. Dual damascene versus single damascene integrations, as well as the influence of a different over-layer will be examined. Finally, a summary and conclusions as well as suggestions for future work are given in Chapter 7.

Chapter 2: Theory of Electromigration

The phenomenon of EM has been known for over 100 years with initial observations reported already in 1861 [in D'Heurle 1978]. In this chapter, the basic fundamentals of EM will be reviewed as well as details pertaining to EM in interconnects with a focus on Cu metallization. Furthermore, current research efforts conducted to improve the EM performance of Cu interconnects will be summarized.

2.1 FUNDAMENTALS OF EM

EM describes the diffusion of atoms or ions in a metal under an applied electric field. Thermal energy leads to a vibration of atoms in the crystal between their equilibrium positions and the "saddle points". The impacts of a large number of electrons bias the probability that atoms cross the "saddle points" and move in one direction, thus leaving their original positions in the crystal and migrating along the direction of electron flow. The driving force for EM can be separated into two parts. The first results from the interaction of the inherent charge of each metal ion with the electric field, while the second is a consequence of the momentum transfer of electrons onto the metal ions. Combining both the electrostatic and the "electron wind" effects, the effective driving force can be written as a sum of both:

$$F_e = F^{es} + F^{ew} = (Z^{es} + Z^{ew})eE = Z^*_{eff}eE \qquad (2.1)$$

where Z^{es} is the charge number of the metal ion, Z^{ew} the charge number corresponding to the electron wind, e the electric charge, and E the electric field. The charge numbers have been combined to the parameter Z^*_{eff}, the apparent effective charge number. Its value depends significantly on the details of the particular diffusion mechanism. Since the atomic arrangement is different for interfaces, grain boundaries or the bulk of the metal, electron/ion interactions vary accordingly, resulting in different Z^*_{eff} values.

The driving force creates a mass flux in the direction of the electrons, which can be described by

$$J = N\mu F_e = N\mu Z^*_{eff} eE \tag{2.2}$$

where J is the atomic flux, μ the atomic mobility and N the atomic density. While the electric field can be expressed as a multiplication of the metal resistivity, ρ, and the current density, j, the mobility can be obtained from the Nernst-Einstein relation:

$$\mu = \frac{D_{eff}}{kT} \tag{2.3}$$

where D_{eff} is the effective diffusivity of the metal ion, k Boltzmann's constant, and T the absolute temperature. Substituting Equation (2.3) into Equation (2.2) yields

$$J = N\frac{D_{eff}}{kT} Z^*_{eff} e\rho j \tag{2.4}$$

The latter part of this equation represents the drift velocity, v_d, of the moving ions as a result of the electromigration driving force:

$$v_d = \mu F_e = \frac{D_{eff}}{kT} Z^*_{eff} e\rho j \tag{2.5}$$

2.2 EM IN INTERCONNECTS

While the equations described above provide a general description of EM in bulk materials as well as in thin films, they have to be modified to account for EM in interconnect lines. Blech *et al.* reported in 1967 that EM was causing failure in Al interconnect lines used in integrated circuits [Blech 1967]. A divergence of atomic flux within the EM mass flux leads to local accumulation or depletion of atoms. The depletion of atoms produces a void, and the accumulation of atoms promotes hillock growth. Both mechanisms can cause line failure. With the increase in importance of integrated circuits, research of EM in interconnects increased significantly. The objective of these studies was to understand the EM failure mechanism in line structures with small dimensions and varying geometries.

2.2.1 The "Blech"- effect

In interconnects, Equation (2.5) needs to be modified to account for the effect of stress-induced backflow of ions [Blech 1976]. During EM, the metal ions deplete the cathode end and accumulate at the anode end. Thus, the atomic density increases slightly at the anode leading to a stress gradient from one end of the line to the other. This gradient drives metal atoms back towards the cathode end resulting in mass transport opposing that of the current driving force. This phenomenon is called the "Blech"-effect. Considering the backflow stress, the drift velocity can be written as:

$$v_d = \mu(F_e - \Omega\frac{\Delta\sigma}{\Delta x}) = \frac{D_{eff}}{kT}(Z_{eff}^* e\rho j - \Omega\frac{\Delta\sigma}{\Delta x}) \tag{2.6}$$

where Ω is the atomic volume and $\Delta\sigma/\Delta x$ the stress gradient. From this equation, it can be inferred that for short lines or low current densities, the EM induced mass transport can be suppressed entirely. As a consequence, the net drift velocity is zero. In this case, a product of length and current density can be used to identify the critical length for a certain current density:

$$(jl)_c = \Omega \frac{\Delta\sigma}{Z_{eff}^{*} e \rho} \tag{2.7}$$

where l_c is the critical line length of the particular test structure. The value of the stress gradient depends on the material properties of the metal as well as the surrounding dielectric. The Blech-effect can be useful as a guideline in the design of complicated interconnect architectures, since the use of line lengths less than l_c can significantly reduce the risk of EM failures. It is important to mention that the interconnects used in this study were purposefully chosen to be very long so that the backflow effect can be neglected here. The drift velocity can be simplified to the product of mobility and driving force as defined in Equation (2.5).

2.2.2 The Transition from Al(Cu) to Cu

While initially pure Al was the material of choice used for interconnects, already in the early 1970s the addition of a few percent of Cu into Al was shown to retard EM [Rosenberg 1972]. Subsequently, in addition to examining the details of the EM mechanism in Al(Cu) lines, significant research activity dealt with the effect of scaling on EM. Several papers can be found summarizing EM research in Al(Cu) technology, such as Ho and Kwok [1989] and Hu *et al.* [1995]. Parallel research focused on identifying a suitable material for future interconnect generations as well as possible processing schemes. IBM and Motorola announced the full incorporation of Cu in a microchip in 1997 [Edelstein 1997, Venkatesan 1997]. Replacing Al(Cu) with Cu provided several obvious advantages as well as a variety of new challenges. The major advantage of Cu is its lower bulk resistivity compared to Al(Cu), which provides faster signal travel and shorter switching times, thus reducing RC delay. Additionally, Cu proved to have superior EM performance as shown already in studies in the early 1990s [Kang 1992, Tao

1993, Wong 1995]. Comparing the EM behavior in Al(Cu) with a variety of differently processed Cu interconnects showed generally much improved lifetimes for Cu samples.

However, the transition from Al(Cu) interconnects to Cu lines required a new integration scheme, which is fundamentally different than the process used for Al(Cu). Al(Cu) interconnects are fabricated by a subtractive etch process as schematically shown in Figure 2.1. First, a barrier layer, commonly consisting of a Ti/TiN bi-layer film, is deposited, followed by the deposition of a layer of Al(Cu). Usually, another layer is deposited for anti-reflective coating purposes, such as TiN. This entire film stack is then patterned with conventional photolithographic procedures. Reactive ion etching (RIE) forms the Al(Cu) lines. The gaps between the lines are filled with dielectric, e.g. $SiO_{2,}$ and then planarized. The conventional subtractive etch process cannot be used for Cu due to the lack of an accurate etching process for Cu. Thus, a reversed process has been developed, called the Damascene process. Figure 2.1(b) shows a schematic of the process flow. A dielectric layer, such as fluorinated SiO_2 (F-TEOS), is first deposited on the oxidized Si wafer. This layer is subsequently patterned by conventional photolithographic methods and reactive ion etching, so that trenches are formed in the dielectric. A Ta-based barrier layer is deposited, covering the sides and the bottom of the unfilled lines. Subsequently, the trenches are filled with Cu in a two-step process. First, a Cu seed layer is deposited. This layer functions as a contact layer for the following electro-chemical filling of the trenches. Electroplating has evolved as the preferred deposition process used for Cu, since it shows very good trench filling capability even for high aspect ratios and is a low cost process with a high throughput. Finally, the top surface of the wafer is polished by chemical mechanical polishing (CMP) to remove the excess Cu and planarize the structure for subsequent processing steps. Finally, the whole structure is capped with a dielectric. The use of the Damascene process provides a variety of changes, which lead to differences in the EM behavior between the Al(Cu) and Cu technologies. For instance, the Cu deposition into existing trenches leads to a different microstructure influenced by the side walls. Furthermore, the interfaces used in Cu metallization are very different compared to Al(Cu) integration. The influence on the reliability behavior of both these effects, as well as of other changes, needs to be examined carefully. In the following, certain aspects of EM pertaining to Cu interconnects will be summarized. While not analyzing Al(Cu) technology in detail, specific differences to Cu processing will be pointed out during the course of this dissertation. Several reviews about the state of EM research in Cu interconnects can be found in the literature [for instance: Rosenberg 2000, Ogawa 2002b, Tu 2003].

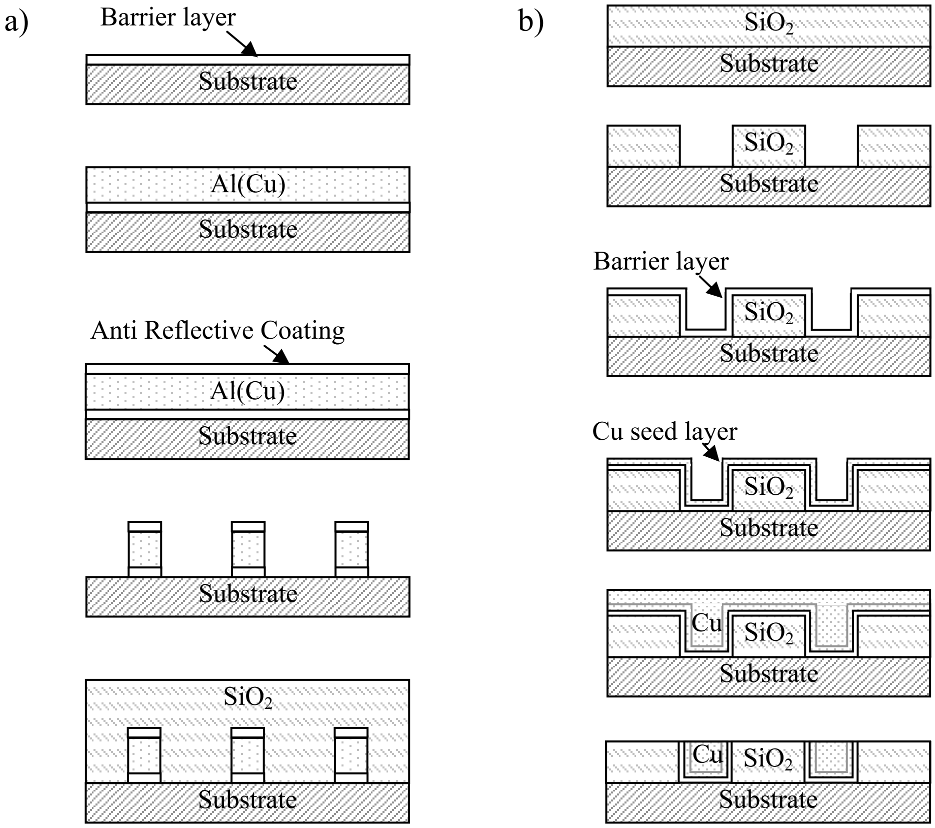

Figure 2.1 (a) Subtractive etch process used for Al(Cu) interconnects; (b) Damascene process used to fabricate Cu interconnects.

2.2.3 Details of the EM-Induced Diffusion Mechanism in Cu Lines

The EM phenomenon in any metal depends on the details of the diffusion mechanism. The effective diffusivity is a combination of individual diffusivities corresponding to all possible diffusion paths, such as diffusion through the bulk, along the top interface, the barrier layer interface, the grain boundaries and dislocation cores. It can be expressed as:

$$D_{eff} = n_B D_B + \frac{\delta_i}{h} D_i + \delta_{Bi}(\frac{2}{w} + \frac{1}{h}) D_{Bi} + \frac{\delta_{GB}}{d}(1 - \frac{d}{w}) D_{GB} + \rho_{disl} d^2 D_{disl} \qquad (2.8)$$

where the subscripts *B*, *i*, *Bi*, *GB* and *disl* indicate bulk, top interface, barrier layer interface, grain boundary and dislocation core properties, respectively. The parameters h and w are the line height and width, respectively, δ_x the effective width of the corresponding diffusion path, d the average grain size, ρ_{disl} the dislocation density, and n_B the fraction of ions diffusing through the bulk of the line. Due to typically small dislocation density, the influence of mass transport through dislocations can be neglected. Likewise, the activation energy of bulk transport is large, preventing any significant contribution to the EM mass flux. For the structures analyzed in this study, the major EM diffusion path appears to be the interface between Cu and the SiN_x passivation layer [Hu 1999, Arnaud 1999, Hau-Riege 2001, Ogawa 2002b, Liniger 2002, Meyer 2002, Hauschildt 2004a, Hauschildt 2004b, Zschech 2004]. Most studies infer the dominant diffusion path by analyzing the influence of varying process parameters on the EM behavior, such as line cross-section or Cu microstructure. In-situ EM experiments in a scanning electron microscope (SEM) on fully encapsulated Cu interconnects performed by Zschech *et al.* [2002] directly showed void formation and evolution at the top interface of the line. It has been observed that the activation energy of the mass transport along the passivated interface correlates with the measured adhesion energy of that interface [Lane 2003], indicating that interfacial bonding and purity have a significant influence on the EM mechanism. Since the structure of the interface between a Ta-based barrier layer and Cu is known to be much denser than the interface between Cu and the SiN_x passivation, significant mass flux along the barrier layer/Cu interface is not expected. Grain boundaries remain as a possible diffusion path. However, the activation energy for grain boundary diffusion is larger compared to the activation energy for diffusion along the top interface, i.e. approximately 1.2eV vs. 1eV [Kaur 1989]. Furthermore, in submicron interconnects, a near-bamboo microstructure has been observed, i.e. most grains span the entire line. Thus, only a minority of grain boundaries are parallel to the electron wind, while the majority of grain boundaries are inclined significantly towards the current flow direction. As a result, the EM driving force is relatively small in most grain boundaries. It needs to be pointed out that in wide lines with polycrystalline grain structure, the influence of grain boundaries on mass flux can be significant [Arnaud 2003]. While a major contribution of grain boundaries towards the EM mass flux is not expected in submicron lines, an influence on the determination of the initial flux divergence sites is likely. The above discussion indicates that all other possible diffusion paths next to the top interface can be neglected here, reducing Equation (2.8) to:

$$D_{eff} = \frac{\delta_i}{h} D_i \tag{2.9}$$

Similar to the diffusivity, the effective charge number varies depending on the active diffusion path, since it depends on the local electronic structure surrounding each atom. Thus, in Cu interconnects passivated with SiN_x, the drift velocity can be written as

$$v_d = \frac{\delta_i}{h} \frac{D_i}{kT} Z_i^* e\rho j \tag{2.10}$$

2.2.4 Influence of Microstructure on EM

The influence of metal microstructure on EM behavior has long been under investigation. Most of these research efforts focused on Al(Cu), however, some reports based on Cu have been published. This topic is a challenging one, since it is usually quite difficult to isolate the effect which caused an observed EM improvement. When analyzing the effect of microstructure, usually differences in processing are required to produce a variety of microstructures. Whether these processing differences change other significant properties of the interconnect besides the microstructure, such as interface quality or metal purity, is sometimes difficult to assess.

In polycrystalline lines, grain boundary diffusion was considered to be a significant contribution leading to EM failure and grain boundary triple points provided flux divergence sites leading to void formation. It was seen in Al-based as well as Cu lines that larger grains and a stronger (111) texture in interconnects resulted in longer lifetimes and tighter standard deviation values due to a reduction of flux divergence sites and fast diffusion paths [for instance: Attardo 1970, Ryu 1998]. Likewise, Vaidya *et al.* [1981] found that the electromigration resistance depends on a variety of microstructure factors such as grain size, its distribution and the texture of the metal, which can be expressed in an empirical relationship of the form $(s/\sigma_g^2)\log(I_{111}/I_{200})^3$. The parameters s and σ_g represent the median value and the lognormal standard deviation of the grain size distribution, and I_{111} and I_{200} are the intensities of (111) and (200) texture components. Again, this relationship appears to be followed in wide metal lines with polycrystalline structure.

However, the influence of microstructure on EM performance decreases with increasing level of bamboo structure for two reasons: first, the removal of the grain boundary network eliminates a fast diffusion path and second, grain boundary triple junctions cannot serve as flux divergence points any more. Several studies have shown that in Al(Cu) technology with near-bamboo grain structure interfacial diffusion, along the edges of the lines, plays a more significant role in the transport of metal ions compared to grain boundaries [for instance: Hu 1993a and 1993b, Atakov 1994]. Likewise, as discussed above, the top interface serves as a major diffusion path in Cu interconnects.

The influence of microstructure on the resulting void formation process has been examined by several researchers, for instance Longworth [1992], Hu [1993a], Toyoda [1998], Hauschildt [1998], Hasunuma [1999], Buerke [1999]. Flux divergence sites were found to be either at the edge of the cathode end, simply because no atom replacement is possible, or at intersections near the line end where a grain boundary and the interface between metal line and passivating dielectric meet. The latter critically depend on the local microstructure at the cathode end, which is different from line to line. Dependences of void formation on local grain misorientation as well as grain boundary properties, such as high energy versus low energy boundary and inclination towards the line, have also been observed.

Another effect of the microstructure on the EM behavior in Cu interconnects seems to be the dependence of Cu diffusion along the interface on the orientation of individual Cu grains. It has been observed in in-situ EM experiments on Cu interconnects by Meyer *et al.* [2002], Liniger *et al.* [2002] and Zschech *et al.* [2004] that the rate of void growth is not constant indicating that the interface structure can vary depending on Cu grain orientation leading to differences in Cu diffusivity. This argument has been used as well in simulations analyzing the variations in EM lifetimes [Fayad 2001, Hauschildt 2004a, Hauschildt 2004b].

Since it appears that the void formation mechanism depends on microstructural features, it seems possible that the characteristics of the EM lifetime distribution depend on the microstructure. It has been observed that polycrystalline lines as well as bamboo lines show monomodal lognormal failure distributions, whereas lines with bimodal grain size distribution and near bamboo lines show bimodal or multimodal failures [Thompson 1993, Knorr 1994]. Additionally, as just mentioned, Fayad *et al.* [2001] used a simulation involving differences in interface diffusivity due to different grain orientations to explain the lognormal standard deviation in lifetimes. Unfortunately, in this study, no direct correlation to experimentally observed EM data was shown. Furthermore, the question why the lifetime distribution appears to follow lognormal characteristics has not been answered. However, a possibility exists that the lognormality is correlated to microstructure features [Gall 1999, Gall 2001].

2.2.5 Recent EM Improvements

As seen in Chapter 1, in order to enhance EM performance, the median time-to-failure of an EM experiment, the activation energy of the corresponding diffusion process as well as the standard deviation of the EM lifetime distribution need to be improved. Most research efforts to increase EM reliability have focused on slowing mass transport at the top interface to extend the median lifetime [Hu 2002, Meyer 2002, Hu 2003a, Hu 2003b, Hu 2004, Meyer 2004, Zschech 2004]. Hu *et al.* analyzed a variety of different coating layers instead of SiN_x, such as CoWP, CoSnP, Pd and Ta/TaN. All of these showed a significant improvement of EM lifetimes due to reduced mass transport. In addition, EM activation energies were observed to increase from a value of approximately 1eV for a SiN_x structure to 1.4eV for a Ta-based cap and 2eV for CoWP coated Cu lines. Another approach to slow mass transport is interface strengthening by alloying the top layer of the Cu line with Al [Meyer 2002]. Zschech *et al.* performed in-situ EM experiments on alloyed samples as well as samples coated with CoWP. In both cases, in addition to void formation at the top interface, void evolution occurred on the bottom of the trenches. Hence, mass flux at the top interface was suppressed to the extent that the contribution of the Cu/barrier layer interface could not be neglected any further. Furthermore, various Cu surface treatments before the deposition of the SiN_x cap led to improved EM performance [Vairagar 2004].

It is clear that the median time-to-failure as well as the activation energy of the diffusion process depend directly on the EM mass transport mechanism. Thus, improving the top interface which serves as the major diffusion path appears to be the most promising approach to enhance EM performance with regard to these parameters. In contrast, a better understanding of the origins of the standard deviation are still needed. It is expected that the lifetime variations increase when processing control is immature. However, the question of the causes of sigma in a well-controlled process remains unanswered. It has been argued that in Al-based interconnects the sigma value is related to the number of diffusion mechanisms participating in void formation, to the variation of the diffusivities within a certain diffusion mechanism as well as to the number and distribution of possible flux divergence sites [Attardo 1970, Thompson 1993]. These relationships were inferred from analyzing interconnects with different microstructures, which resulted in different sigma values. While qualitatively identifying significant contributions to the sigma value, a more quantitative analysis was not performed in either case. Examining Cu interconnects, Hu *et al.* [2004] observed a decrease in sigma of EM lifetime distributions with increasing resistance failure criterion. This phenomenon was attributed to an increase in chance of growing similar void sizes in all samples when having a longer void growth time. Again, a more quantitative approach to explain the sigma values was not attempted. More quantitative approaches were performed by Oates [1996 and 1998], Fayad *et al.* [2001] Dwyer [2004], and He [2004]. The former presented a model for the calculation of the sigma value of EM lifetimes as a function of processing parameters, such as line cross-section variations, as well as EM testing conditions, namely temperature and current density. It was suggested that this model could explain the increase of sigma as a function of testing temperature. Likewise, it described the increase in sigma with the current density decreasing and thus approaching the critical current density for the lines examined in that study. However, details of the effect of reduced mass transport with the current density approaching the critical value due to the Blech-effect were not examined. Additionally, the influences of microstructure as well as detailed diffusion characteristics were not analyzed. Fayad *et al.* used a simulation involving differences in interface diffusivity due to different grain orientations to explain the variations in lifetime. A shortfall of this study, as mentioned above, is the lack of a correlation to experimental data. Furthermore, no additional parameters inherent to the EM experiment were taken into account. Dwyer presented a simulation of median time-to-failure as well as standard deviation based on the random distribution of failure-units within the interconnect, with failure-units being polycrystalline segments of a certain length. Again, this study does not show a direct correlation to experimental data, and it excludes the influence of experimental parameters on the EM lifetime distribution. He *et al.* [2004] investigated the behavior of sigma as a function of current density, line length and temperature using a deterministic model and Korhonen's approach [Korhonen 1993]. Under the assumption that the statistics of the critical void volume can be correlated with the observed lifetimes, the behavior of sigma was deduced. However, the origin of the lognormal sigma of an EM lifetime population and its value were not explained in detail.

An analysis of the effect of experimental factors of the EM experiment as well as of processing variations on the sigma value of EM lifetimes will be examined in this study. Additionally, the influence of the details of mass transport will be included. The approach is experimental, accompanied by Monte-Carlo type simulations. As mentioned above, the objective of this study is to identify intrinsic parameters that control the EM characteristics in Cu interconnects and to develop a kinetic model that explains the measured statistical variation in EM lifetimes. A proper understanding of the parameters inducing lifetime variations, accompanied by an appropriate kinetic model, enable predictions of EM statistics for future interconnects.

Chapter 3: Experimental Procedure

In this chapter, the experimental details pertaining to this study will be discussed. First, the processing sequence used to fabricate the samples is explained. These samples are subjected to EM test conditions. EM testing is an accelerated lifetime test using current density and temperature as acceleration factors. Details about the EM experiments are described including information about the test structures, EM testing conditions and the test system. Subsequently, a section about data analysis provides information about the analysis of the electrical data and microscopic failure analysis of tested samples. The following section about microstructure characterization includes the experimental procedure as well as results on grain size and texture measurements. Finally, the simulation procedure used to model the experimental data will be explained.

3.1 SAMPLES AND PROCESSING SEQUENCE

Current interconnect structures consist of several metal levels in order to provide enough connections for all active devices. As a result, a large number of processing steps are required to finish the backend fabrication. The individual steps are very similar for each metal level. In the following, these will be explained in detail.

The Cu interconnects used in this study were prepared by Freescale Semiconductor using the mask set K79W. The Cu lines were surrounded by a thin Ta barrier layer on the bottom and on the sidewalls, and capped by SiN_x on top. The dielectric material in between Cu lines was fluorinated SiO_2 (F-TEOS). The line structures were produced using the Damascene process as described in Chapter 2. The barrier layer is deposited by physical vapor deposition (PVD). The purpose of this layer is to prevent Cu from diffusing into the surrounding Si and SiO_2, where it destroys the active devices or creates shorts to adjacent metal lines. Extensive research has been done to find a suitable barrier to impede the diffusion of Cu and to provide good adhesion at the interface. Best results were obtained using Ta-based barriers, such as pure Ta, Ta_xN_y and amorphous ternary alloys, for example $Ta_xSi_yN_z$. [Kolawa 1991, Holloway 1992, Wang 1993, Nicolet 1995]. Bilayers of these materials are being used as well. In this study, pure Ta has been used with thicknesses of approximately 20nm and 10nm on the bottom of the interconnect and on the trench sidewalls, respectively. After deposition of the barrier layer, a PVD Cu seed layer was deposited without a vacuum break. Subsequently, the plating process of 0.8µm Cu was conducted in a commercially available fountain plater. After the electroplating, the wafers were annealed in forming gas at 250 °C for 30 min. Since the lines are only approximately 0.3µm deep, the top surface of the wafer needs to be polished by chemical mechanical polishing (CMP) to remove the excess Cu and planarize the structure for subsequent processing steps. The dielectric cap used for the majority of samples was 50nm of SiN_x, processed with chemical vapor deposition (CVD). The described processing sequence was repeated for all needed metal levels.

Additional experiments were performed on samples with varying processing conditions. First, samples with smaller line height were examined. The height was reduced by ~30-35% from 0.3µm to 0.21µm by additional chemical mechanical polishing. Secondly, in addition to a SiN_x passivation layer, another capping layers, SiC, was analyzed. The SiC layer is produced by a CVD process.

3.2 EM TEST STRUCTURES

EM test structures consisted of two metal levels connected by vias as indicated in Figure 3.1. The current flowed from a wide metal M1 line through the via into the metal

M2 line, which was the line of interest in this case. The test structure had a target line length, width and height of 250µm, 0.18µm and 0.3µm respectively. Only one line was tested for each device under test (DUT).

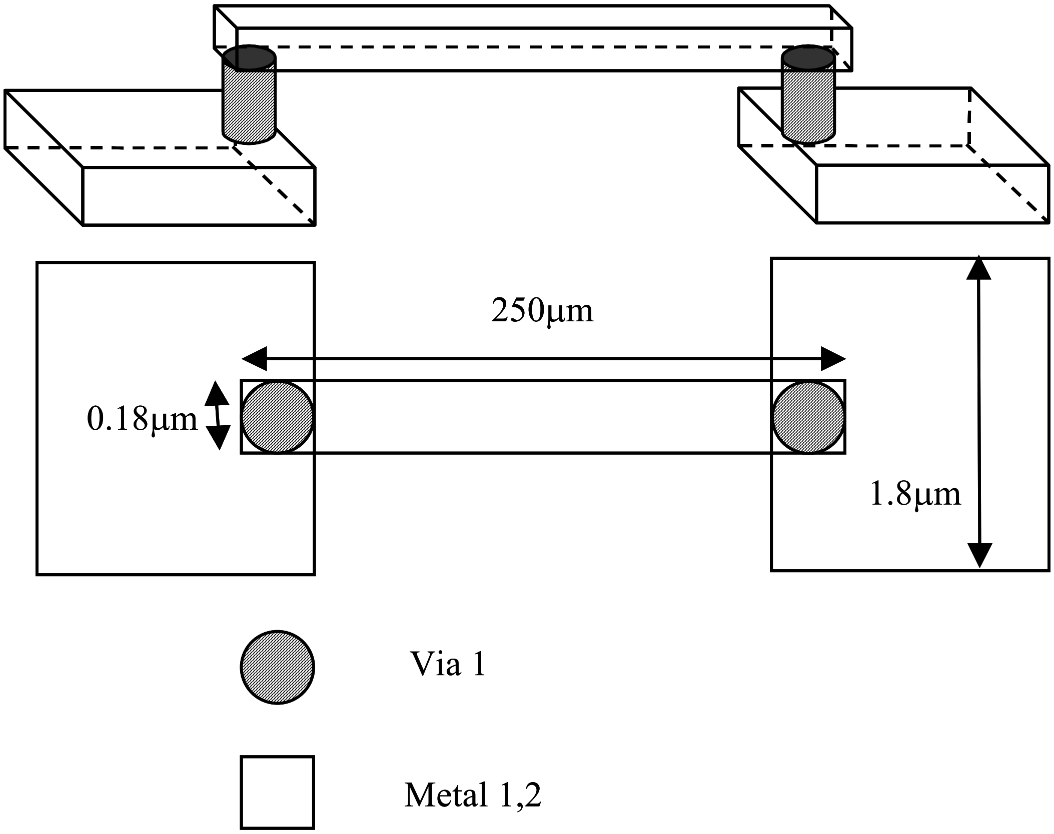

Figure 3.1 A schematic view of the V1M2 structure used for EM experiments. The 0.18µm wide M2 line is connected by vias to the underlying 1.8µm wide M1 supply lines.

Most EM experiments were performed on single damascene interconnects, i.e. the Cu line is separated from the underlying vias by a barrier layer as illustrated in Figure 3.2(a). The processing sequence for the via level is identical to the one described above for the lines. Furthermore, experiments were conducted on dual damascene samples. A schematic view of a dual damascene structure is shown in Figure 3.2(b). In this case, no barrier layer exists between the Cu in the via and in the line. The metal deposition of both levels is conducted at the same time, including barrier, seed and line filling processes. This process sequence is desired, since it reduces processing steps, and thus manufacturing costs. Additionally, the resistance of the structure is reduced by eliminating the barrier layer above the via. However, significant challenges arise by processing vias and trenches at the same time, for instance the via holes are much deeper, which creates problems for the etch as well as metal filling processes. Furthermore, since the Cu in the via is not enclosed, but directly in contact with the Cu in the trench, the via is susceptible to EM damage. Void formation in the via has been observed to contribute to early failure in EM experiments impacting the statistics of the lifetime data [Ogawa 2001, Ogawa 2002a, Gill 2002, Lai 2001].

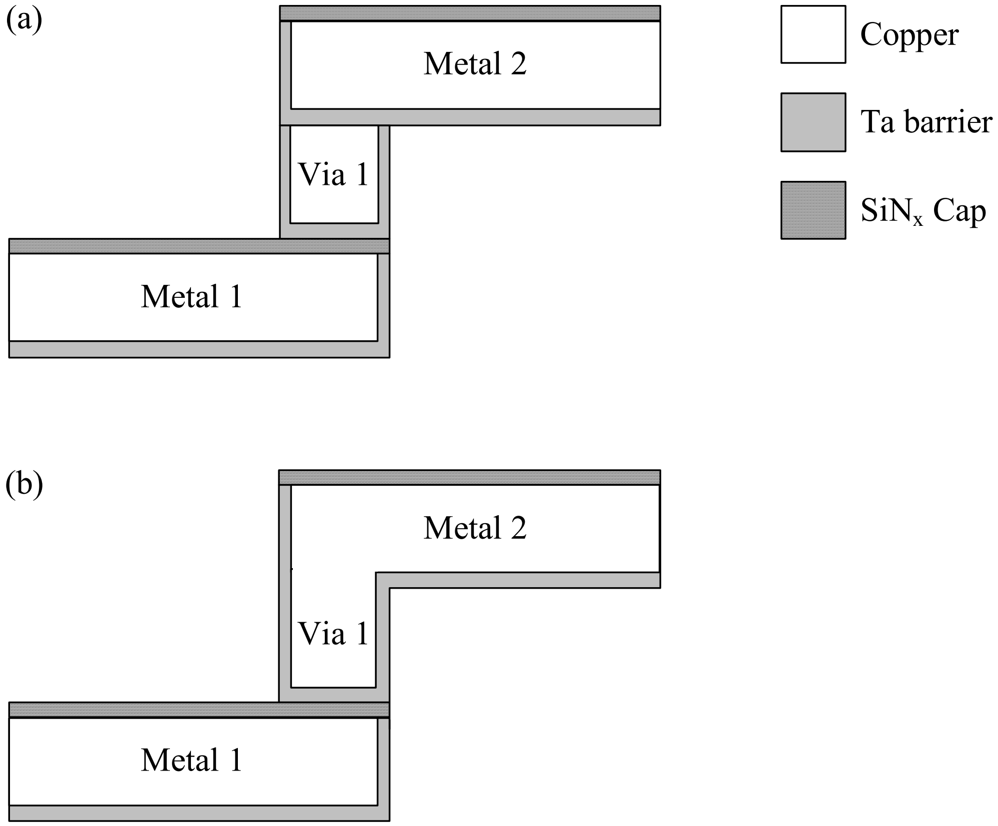

Figure 3.2 Schematic views of (a) a single-damascene V1M2 structure and (b) a dual-damascene V1M2 lay-out. The basic difference between these structures is the barrier layer between V1 and M2, which exists in (a), but not in (b).

3.3 EM TESTING CONDITIONS

All EM tests performed in this study were package-level tests. Testing was performed in QualiTau^{TM} semiconductor reliability testing systems [QualiTau, Inc]. Each testing system could be loaded with 10 high temperature socket boards, which provided the electrical connections from the packages to the electronics of the test system. Two different types of ovens were used. In one system, the socket boards provided space for 6 packages each, while in the other oven, each board could hold 12

DUTs. Thus, depending on the oven, the testing capacity was 60 or 120 samples per test, respectively.

For sample packaging, wafers were diced using a diamond saw, so that dies containing the EM test structure could be removed. The individual dies were attached to 16-pin dual inline packages using silver paste. Aluminum (Al) wirebonds provided the electrical connections between the bonding posts of the package and the bonding pads of the test structure. The upper bonding pads of each test structure consisted of Al to avoid any corrosion issues with exposed Cu and intermetallic reactions between Al wires and Cu pads. The packages were inserted in the sockets of the boards, which in turn were loaded into the EM test system.

The electrical measurement was a 2-point measurement on the die. 2 bond pads of the test structure were connected to 2 bonding posts of the package serving as current input and output. A 4-point measurement was taken at the bonding posts of the package. The two posts connected to the package were connected to two additional bonding posts. The difference between a 4-point measurement at the package and at the die is negligible, since the Al wirebonds have a resistance of only approximately 0.1Ω each at room temperature, thus contributing only about 0.1% to the total resistance of the test structure. A constant current was sent through the samples while the voltage was recorded over time. Thus, the resistance behavior of each sample was monitored.

The oven temperature was set to 300°C. The tests were conducted with an approximate current density of 1.5MA/cm^2, referenced to the Cu portion of the entire interconnect cross-section. Thus, the current employed for regular height samples was 0.67mA, whereas only 0.47mA was sent through the reduced line height samples. Experiments were either stopped after a certain test time or after a specified resistance increase had been reached. The former case will be referred to as “time-based EM tests”, whereas the latter case will be called “resistance-based EM tests”. Five EM tests with different times were conducted, namely 18.75h, 37.5h, 150h, 300h, and 1000h. For resistance-based EM tests, the current for each line was turned off individually when that particular line reached the specified resistance change, such as 10%, 30%, 50% or 100%. These tests were computer controlled. Additionally, one EM test was monitored on a daily basis to manually turn off the current to samples when the first resistance increase was observed.

3.4 DATA ANALYSIS

The EM lifetimes were extracted from resistance versus time curves. For each sample, the time needed to reach a certain resistance increase was acquired. Thus, the EM lifetime distributions were obtained as a function of resistance increase criterion. A lognormal distribution function was used to fit the lifetime data.

In order to examine the correlation between EM lifetimes and void sizes, the void areas of at least 10 samples for each EM condition were obtained using focused ion beam (FIB) cross sectioning together with scanning electron microscope (SEM) imaging. The microscope used is a FEI Strata™ DB235, which is a dual beam SEM/FIB system [FEI Company]. It combines a SEM with a thermal emission tip for high resolution imaging and a FIB with a gallium metal ion beam source for cutting. First, a box is cut adjacent and parallel to the EM-tested line using the ion beam with a high current at 30kV. Using reduced current, the box is slowly extended towards the line until it reaches into the line showing the cross-section of the void at the cathode end. Cutting is stopped approximately in the middle of the line. The cut shows the cathode end with the via connecting M1 and M2 metal levels and extends 20-30μm down the line, thus exposing about 10% of the total line length. Figure 3.3 displays an SEM image showing a complete cut. SEM images were taken at various magnifications with a high resolution detector applying a voltage of 5kV. Since the electron and ion guns are arranged with an angle of 52° between them, all SEM images were taken under that angle. Thus, any measurements taken from the images need to be corrected using basic trigonometry.

Void size measurements were performed using Image Pro Plus Software [Media Cybernetics, Inc.]. After calibration using the scale bar on the SEM images, the void area was outlined as illustrated in Figure 3.4, and the area was obtained. Additional measurements include the void lengths on top of the void and adjacent to the via and the void inclination angle with respect to the line. The positions of these measurements are indicated in Figure 3.4. As mentioned above, the measurements need to be corrected for the imaging angle.

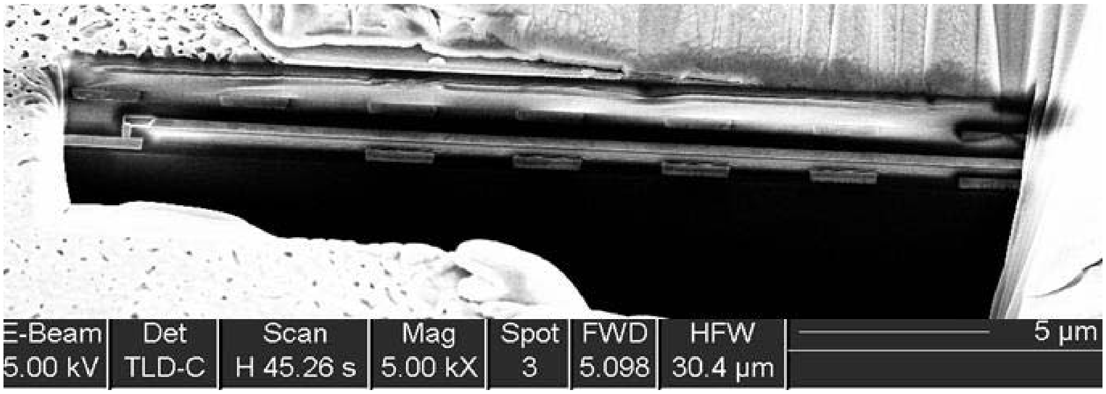

Figure 3.3 FIB image showing the cathode end of an EM tested V1M2 structure together with approximately 25µm of M2. Structures belonging to metal level 3 can be seen above the M2 line.

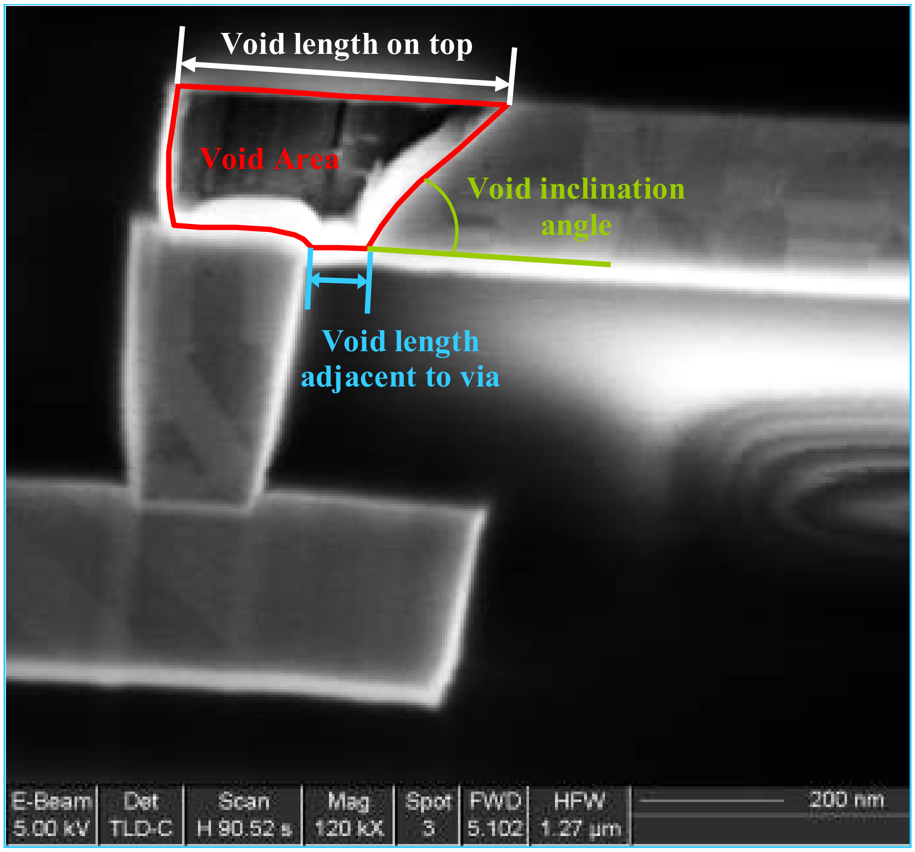

Figure 3.4 FIB image of a voided interconnect. The void outline is traced to obtain the void area. Additionally, the void length on top and adjacent to the via, as well as the angle between void and line are measured as indicated.

3.5 MICROSTRUCTURE ANALYSIS OF CU INTERCONNECTS

The influence of microstructure on EM behavior in interconnects has been reviewed in Chapter 2.2.4. It has been seen in several studies, that the reliability in interconnects can depend on the microstructure in the lines. Thus, in order to examine the influence of microstructure on the statistical behavior of EM lifetimes the microstructure of the Cu lines has been analyzed including determination of grain size and its distribution and texture.

3.5.1 Grain Size Analysis using TEM

The grain size in lines has been measured from plan view Transmission Electron Microscopy (TEM) images.

3.5.1.1 Samples and Sample Preparation

The microstructure in Cu interconnects has been analyzed using large arrays of parallel lines. These samples have been selected over the EM structure, since the sample preparation for microscopic analysis is much simpler and a larger amount of data can be obtained per sample. However, the results are expected to be representative for the EM samples, because the line arrays have identical dimensions, and the same processing sequence was used. Samples were taken from lots U28477, U32381 and D59459. These are K19Y wafers processed only through Metal 1, which again facilitates sample preparation significantly. A cross section of the wafer stack can be seen in Figure 3.5. In addition to samples with 0.18µm line width, samples consisting of line arrays with 1.8µm wide lines were prepared. Furthermore, one sample was prepared from a different lot made with mask set L85P, which had an array of 0.12µm line width.

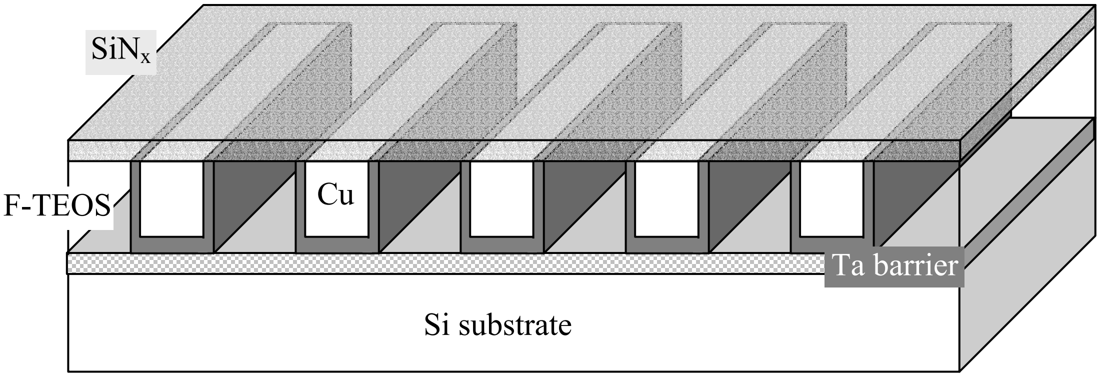

Figure 3.5 Schematic cross section of wafer stack used for microstructure analysis.

Most samples were prepared by wedge polishing using a tripod holder and subsequent ion milling. As a comparison, a sample, which was obtained with an FIB, was analyzed. All samples had a large number of electron transparent lines providing a substantial amount of information, even though the wedge polished samples were by far exceeding the FIB-prepared one. Figure 3.6 shows a comparison of the grain size distributions obtained from differently prepared samples from the same wafer. Even though the distributions seem to be identical for small grains, significant differences are observed for large grains. This discrepancy arises because the sample preparation methods produce samples from different positions along the height of a line. SEM cross-sections of Cu lines show that the trenches are tapered with increasing width from bottom to top. Typical cross-sections will be displayed in a later part of this chapter. In the FIB method, the line is cut approximately in the middle, whereas wedge polishing leads to cuts from the top of the line. Hence the analyzed TEM samples have different line widths leading to the observed larger grain sizes in wedge polished samples from the wider top of the line. The main objective of this study is to analyze EM characteristics. Since the major diffusion path for EM is at the top interface of the Cu line, all grain size data reported in the following sections stems from wedge polished samples.

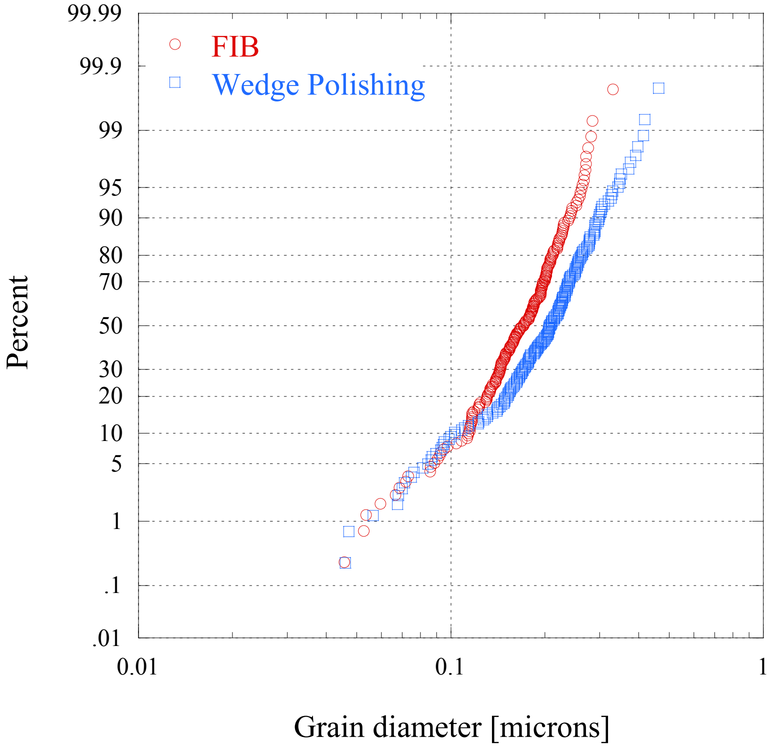

Figure 3.6 Comparison of grain size distributions obtained from a wedge polished sample and an FIB prepared sample.

In order to examine whether wedge polishing generates TEM samples with reproducible results, two samples from the same die of one wafer were prepared and analyzed. Figure 3.7 shows the distributions of two samples from the same center die. Clearly, no statistical differences can be observed between different samples from the same die. Both distributions appear to be identical showing bimodal behavior with values larger than the line width exhibiting a smaller sigma value.

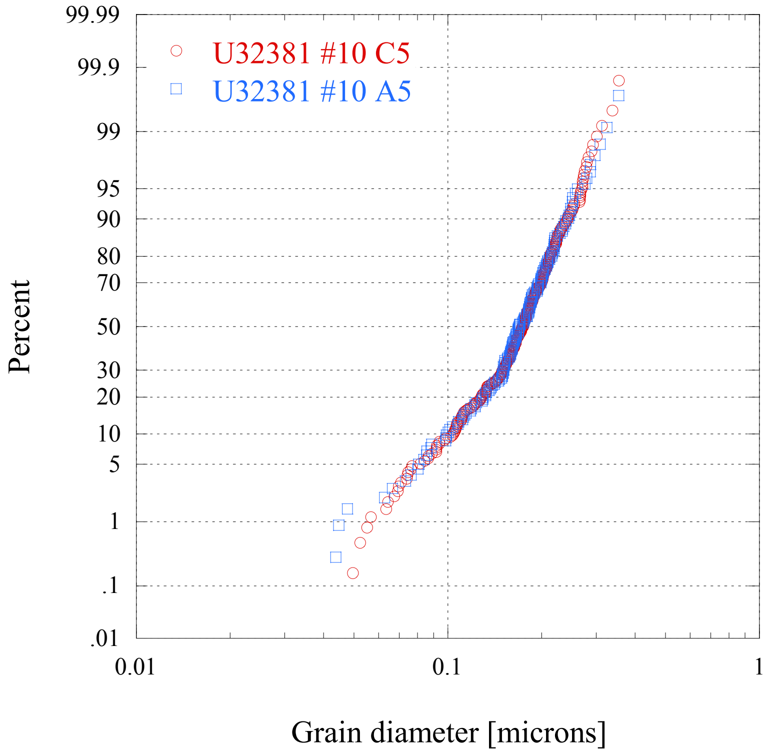

Figure 3.7 Grain size distributions of two samples from the same center die of one wafer.

3.5.1.2 Imaging and Image Analysis

TEM imaging was performed at 200kV in a JEOL2010 microscope located at Pickle Research Center, UT Austin [JEOL USA, Inc]. Figure 3.8 shows a bright field TEM image. In order to facilitate the identification of grains, a series of images of the same location with varying sample tilt were recorded. Tilting the sample leads to changes in diffraction conditions enhancing the shapes of differently oriented grains. The grains were outlined on the non-tilted image by comparing with tilted images.

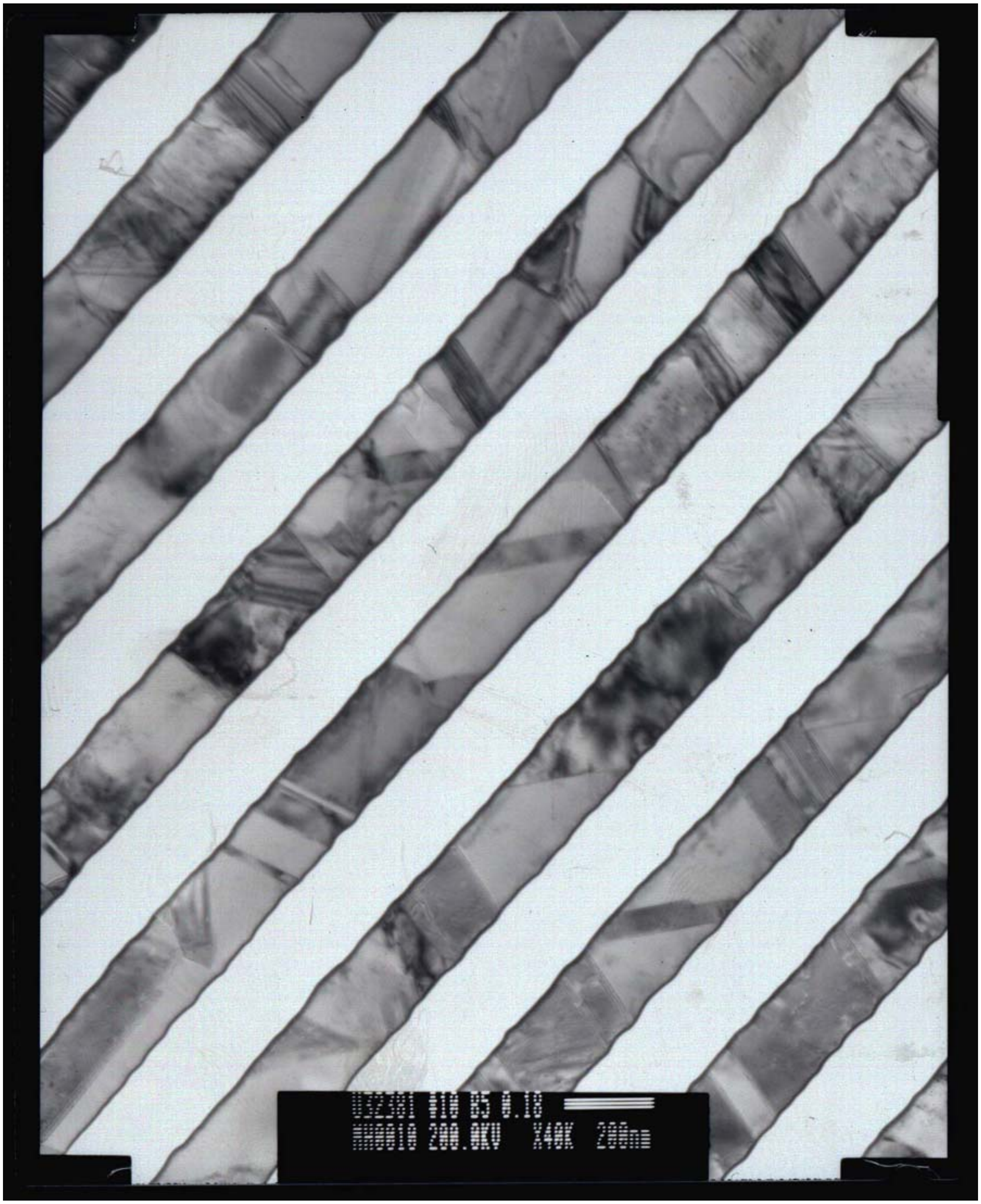

Figure 3.8 TEM plan-view image of Cu lines in F-TEOS

The grain size analysis was performed by two different methods. In the first method, the dimensions along (x) and across (y) the line for each outlined grain were measured by hand. The grain diameter, d, was taken as the mean of both measurements. Results of this method can be seen in Figure 3.9, which shows the grain size distribution in each direction as well as the diameter d. Figure 3.9(a) shows data from 0.18µm wide lines, while Figure 3.9(b) shows data from 1.8µm wide lines of the same wafer. In the 0.18µm wide lines, an upper threshold in the y-direction due to the line dimension is observed, whereas in the x-direction no upper threshold could be detected. In the wider lines, the grain sizes in x- and y-directions seem to be very similar with deviations showing only for large grains. In the case of large grains, the line width again imposes a limit on grain growth across the line. The mean of both directions appears to be a reasonable definition for grain size.

In the second grain size analysis method, the grain size distributions were obtained by scanning the grain outlines and obtaining the areas of each outlined grain using Image Pro Plus Software [Media Cybernetics, Inc.]. Grain diameters are calculated assuming circular grain shapes. Figure 3.10 shows a comparison of grain size distributions obtained by both methods for 0.18µm as well as 1.8µm wide lines. The results do not seem to be significantly different.

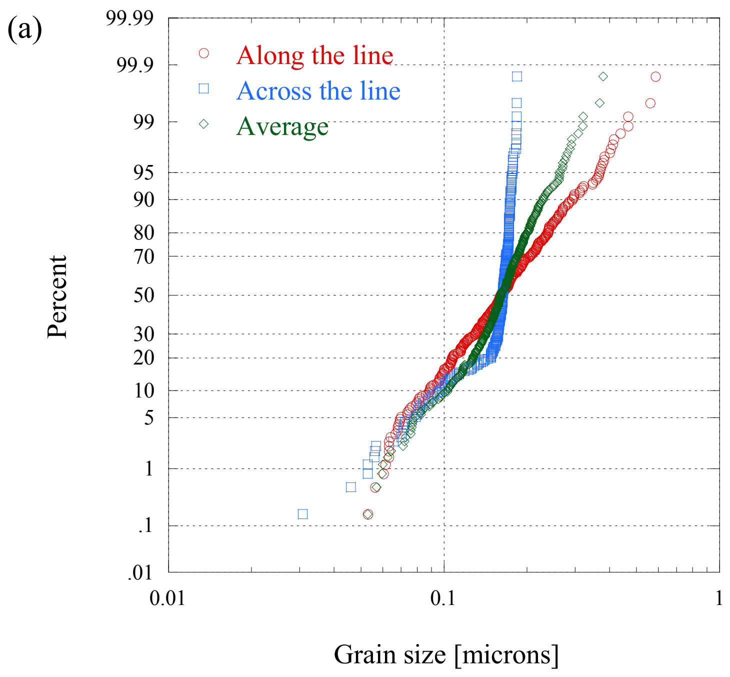

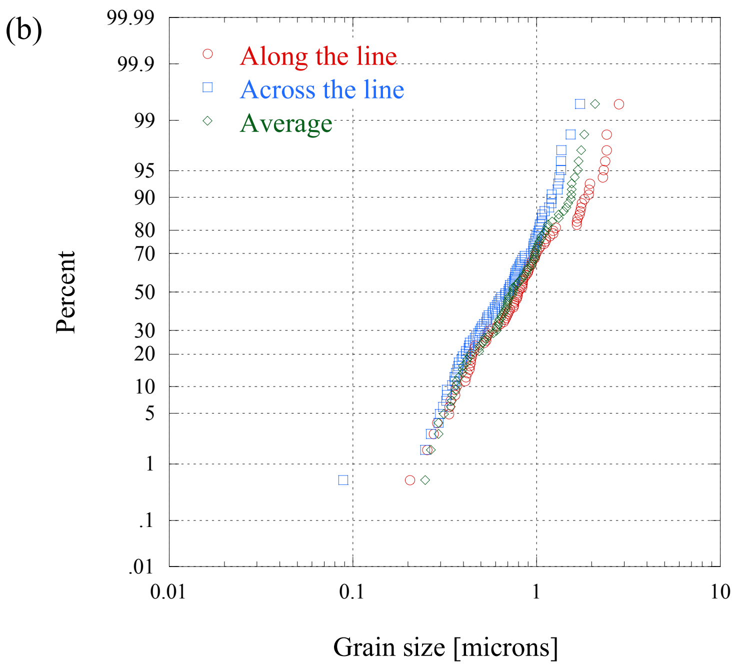

Figure 3.9 Grain size distributions of (a) 0.18µm and (b) 1.8µm Cu lines of the same wafer. Distributions obtained from measuring the dimensions of each grain along (x) and across (y) the line are shown as well as the grain diameter distribution. The grain diameter is defined as the median of x and y.

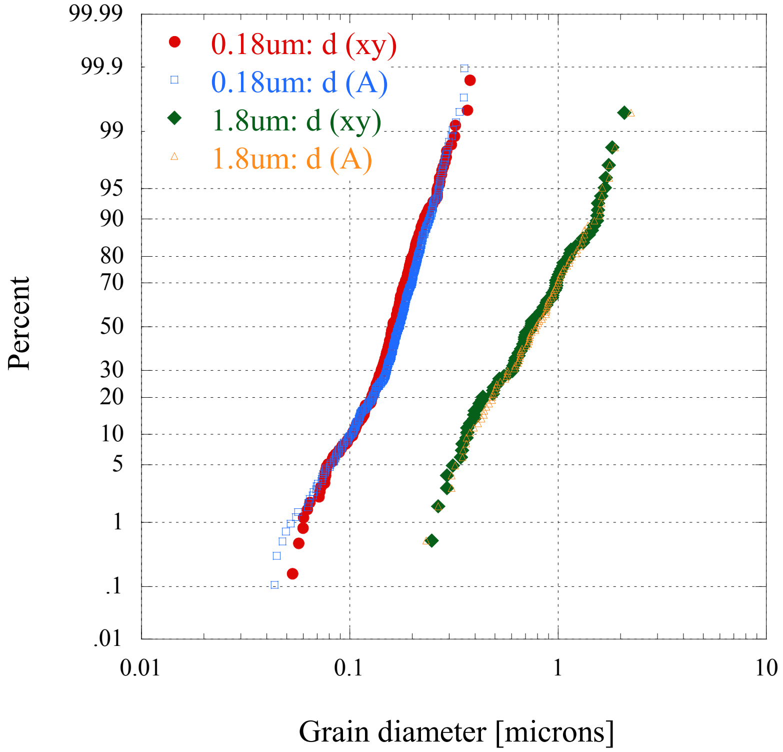

Figure 3.10 Grain size distributions of 0.18µm and 1.8µm Cu lines. Grain diameter distributions obtained from the x/y and from the area method are compared.

For most of the grain size analysis, twins were not counted as separate grains, since their grain boundaries are not considered to be fast diffusion boundaries contributing significantly to EM mass flux. However, it has become clear that the major EM diffusion path is at the top interface. The diffusivity at the interface could be influenced by the grain orientation, which defines the interface structure. Thus, the interface structure is expected to be different for twins compared to their "parent" grain leading to differences in Cu diffusivity. Hence, for a selected number of images, twins were counted as separate grains. The result of this analysis will be presented later in this section.

3.5.1.3 Influence of Die Location on Cu Grain Size Distribution

In order to analyze the influence of die location on the wafer on the Cu grain size distribution, samples prepared from a center die and an edge die of the same wafer were compared. The grain size distributions of both dies are displayed in Figure 3.11. The number of grains contributing to each distribution is 348 for the center die and 277 for the edge die, respectively. Clearly the edge die sample has a larger average grain size. Its distribution seems to be simply shifted to larger grains, i.e. the slopes of the distributions are similar for large as well as small grains. Deviations in line dimensions between wafer center and wafer edge might be responsible for these differences. The line width of the edge die has been measured to be approximately 0.175µm, whereas the trenches in the center die are only about 0.148µm wide. The line width is defined as the Cu portion of a line. When scaling the data to a line width of 0.16µm as shown in Figure 3.12, the distributions of center and edge die are alike. Hence, in edge dies, larger grains can grow due to less growth restrictions. An additional contribution to the grain size differences in edge and center dies could arise from temperature non-uniformity across the wafer during annealing or passivation layer deposition, which might induce different grain growth behavior.

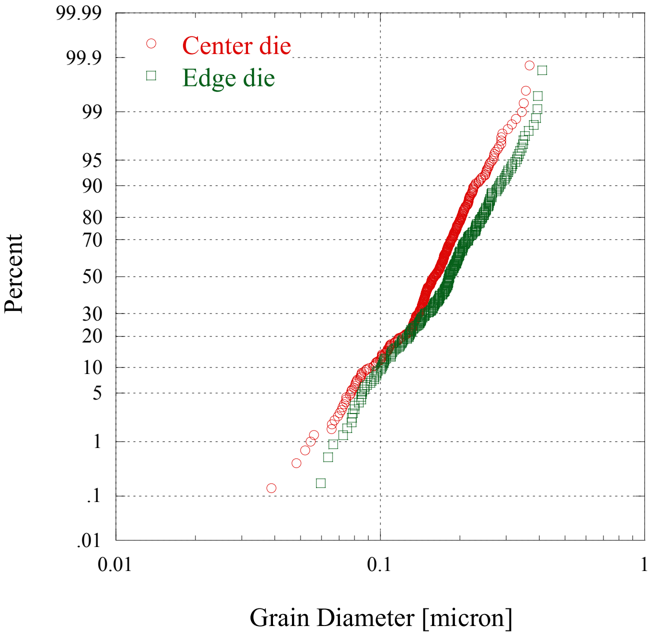

Figure 3.11 Grain size distributions of 0.18µm Cu lines from a center and an edge die of the same wafer.

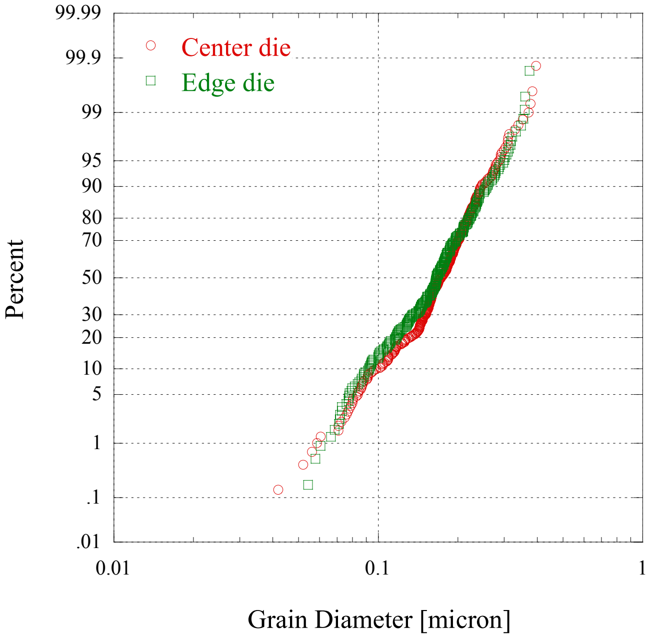

Figure 3.12 Grain size distributions of 0.18µm Cu lines from a center and an edge die of the same wafer scaled to 0.16µm average Cu line width.

3.5.1.4 Influence of Line Width on Grain Size Distribution

Figure 3.13 shows the grain size distributions for three different line widths, namely 0.12µm, 0.18µm and 1.8µm. The grain size in the lines increases with increasing line width due to less growth restrictions. All distributions show a bend in the curve at approximately the line width. This bimodality is caused by grains spanning the whole line. For all line widths, the small grain distribution has a larger sigma value compared to the larger grain distribution. Small grains can grow freely in three dimensions, whereas larger grains, which are constrained by the trench walls, can only grow in the direction along the line. These growth restrictions might promote a tighter grain size distribution. The distribution in 0.12µm lines has the bend at a very low percentage of grains indicating that most grains span the whole line. The bend occurs at larger percentages with increasing line width. The grain size distribution in 1.8µm lines shows the bend only at approximately 90% demonstrating that most grains in these lines do not cover the line width. It has been shown in thin films that grains grow only to a certain multiple of the film height. Thus, the line height provides growth restrictions for the plan view grain size in addition to the line width. In general, the characteristics of the grain size distribution scale with line width reflecting the growth restrictions imposed by finite line dimensions.

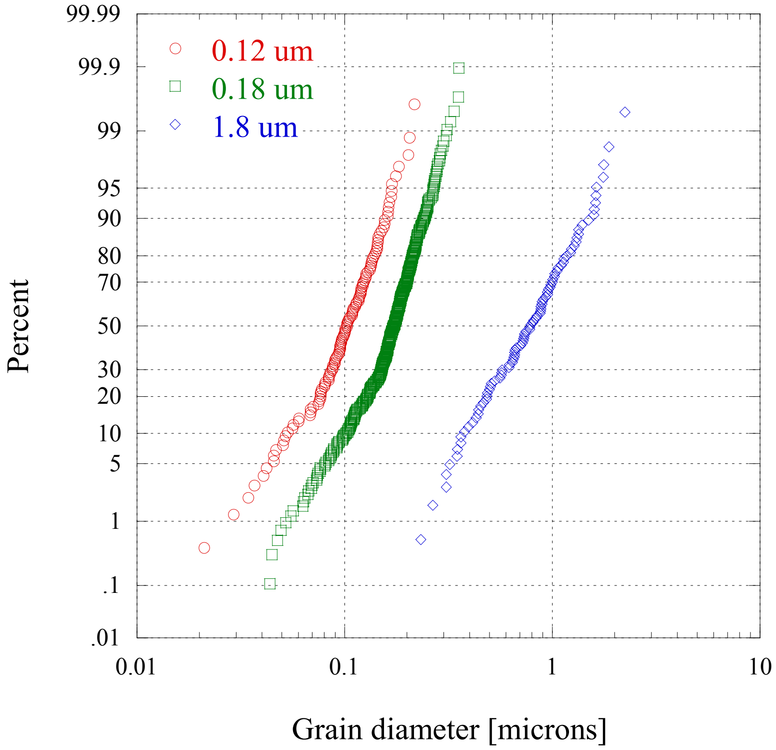

Figure 3.13 Grain size distributions of 0.12μm, 0.18μm and 1.8μm Cu lines.

3.5.1.5 Statistical Analysis of Grain Size Data

In order to analyze the statistical nature of the grain size distribution in detail, a large number of grains are needed. Figure 3.14 shows grain area as well as diameter distributions of 0.18μm Cu lines obtained from data of various lots with the same processing condition. The total number of grains included in the distribution is approximately 1600. Both grain size distributions show the characteristic bend in the distribution. Attempts to fit the total grain size distribution by a variety of monomodal distribution functions, such as normal, lognormal and Weibull distributions, failed. Using Monte Carlo simulation, a bimodal lognormal distribution was fitted to the distribution. The simulation consisting of 1600 data points has been overlaid on the experimental data in Figure 3.14. For the grain diameter, a bimodal lognormal distribution with a median grain size of 0.098µm and a sigma of 0.42 for grains smaller than the line width and a median grain size of 0.185µm and a sigma of 0.26 for grains larger than the line width led to a good fit to the experimental data. Likewise, median values of 0.0076µm^2 and 0.028µm^2 and sigmas of 0.7 and 0.53 were found for the grain areas belonging to the smaller and the larger grain distributions, respectively. It appears that only 20% of the grains belong to the small diameter distribution, while the majority of the grains have diameters exceeding the line width. Thus only approximately 320 grains have been measured from the former distribution, while about 1280 grains have been analyzed from the latter distribution. This provides a problem for sound statistical analysis, since according to Kurtz *et al.* [1980b] the number of grains, *N*, required to distinguish between distribution functions is quite large. It can be calculated according to

$$N = \left(\frac{200 * coef.\mathrm{var}iation}{\%accuracy}\right)^2 \tag{3.1}$$

Kurtz *et al.* [1980a] showed theoretically that normal grain growth leads to lognormally distributed grains. Experimental support was provided by various researchers, even though Fayad *et al.* [1999] observed a better fit using a Weibull distribution. Assuming lognormality, the coefficient of variation is

$$coef.\mathrm{var}iation = (e^{\sigma^2} - 1)^{\frac{1}{2}} \tag{3.2}$$

where σ (sigma) is the lognormal standard deviation. Assuming 2% accuracy, Equation (3.1) reduces to

$$N \cong 10000(e^{\sigma^2} - 1) \tag{3.3}$$

Hence the number of grains required for sound statistical analysis is approximately 1000 if sigma equals 0.3 and about 1700 if sigma equals 0.4. From these values, it is clear that the number of grains in the small diameter distribution needs to be increased significantly in order to improve the accuracy of these results, while the amount of data obtained for large grains is already sufficient. In general, however, the fit of the experimental data provided by a bimodal lognormal distribution appears to be very good. Thus, it is very likely that this is the correct choice for a distribution function needed to describe grain size distributions in Cu interconnects. Again, different grain growth mechanisms as a result of geometrical restrictions are expected to be responsible for the bimodal grain size distribution.

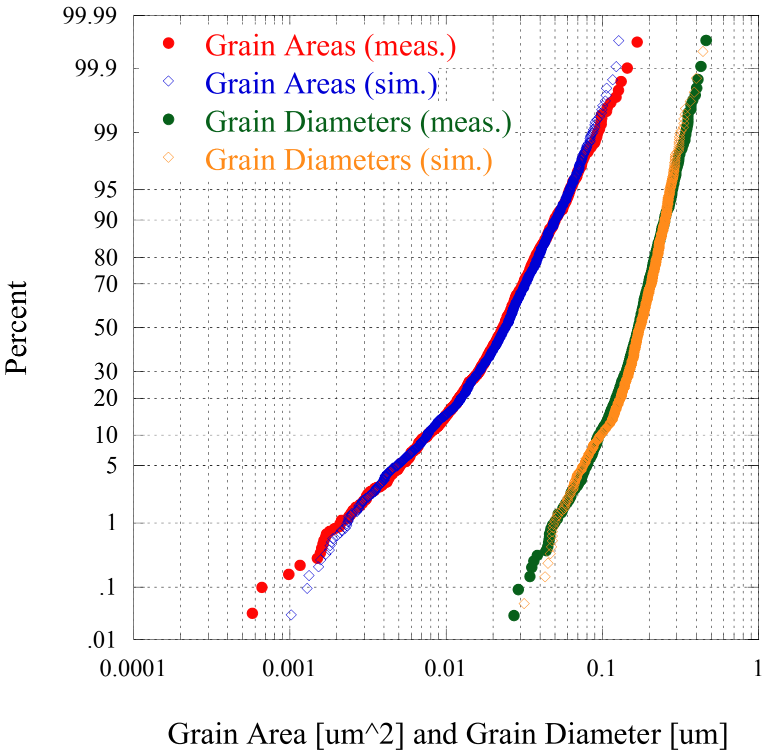

Figure 3.14 Grain size distribution in 0.18μm Cu lines. A bimodal lognormal distribution has been fitted to the experimental data using Monte Carlo simulation.

3.5.1.6 Grain Size Distributions with Twins as Separate Grains

As mentioned above, the interface area of the grains at the top of the line appears to be an important microstructural parameter when analyzing EM behavior in 0.18µm Cu interconnects. Since the interface structure of twins is potentially different compared to their parent grains, twins were counted as separate grains for a selected amount of images. The area of approximately 900 grains was obtained. Three grain size distributions are plotted in Figure 3.15. One distribution shows only the twins, another contains the non-twinned and "parent" grains and the third one all grains. The latter two grain size distributions show the typical bend in the distribution with smaller grains having a larger sigma and larger grains a smaller one. In contrast, the median grain size of the twins is significantly smaller leading to an almost straight distribution. With 311 of the total 900 grains being identified as twins, the number percentage of twins is 34%. However, due to their small size, their percentage of the total area is only 15%. The distribution of all grain sizes is plotted again in Figure 3.16 together with a fit using Monte Carlo simulation. Again, a bimodal lognormal distribution was fitted to the experimental distribution. The simulation consisted of 2800 data points. The simulation indicated that the small grain distribution has median and sigma values of 0.0038µm^2 and 0.95, respectively, whereas the large grain distribution has a median of 0.0168µm^2 and a sigma of 0.6. The latter consists of approximately 65% of the data. This grain area distribution will be used in Chapter 5 for the analysis of mass transport variations.

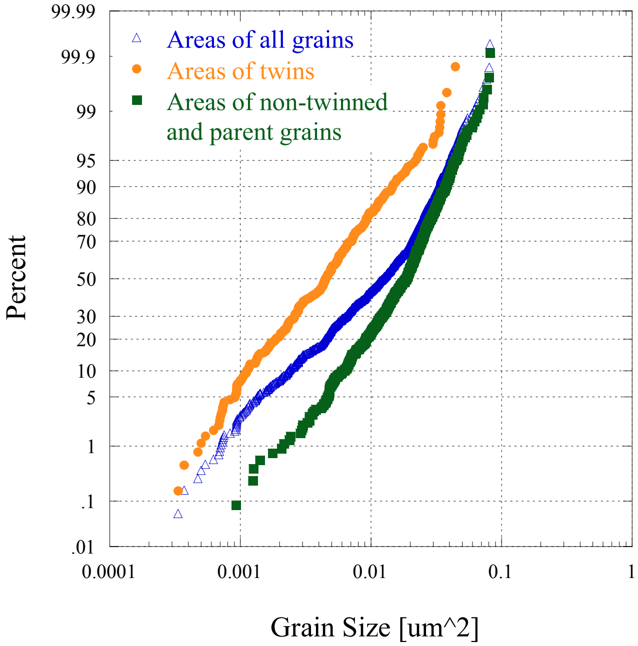

Figure 3.15 Grain size distributions of twins, non-twinned and "parent" grains and all grains combined.

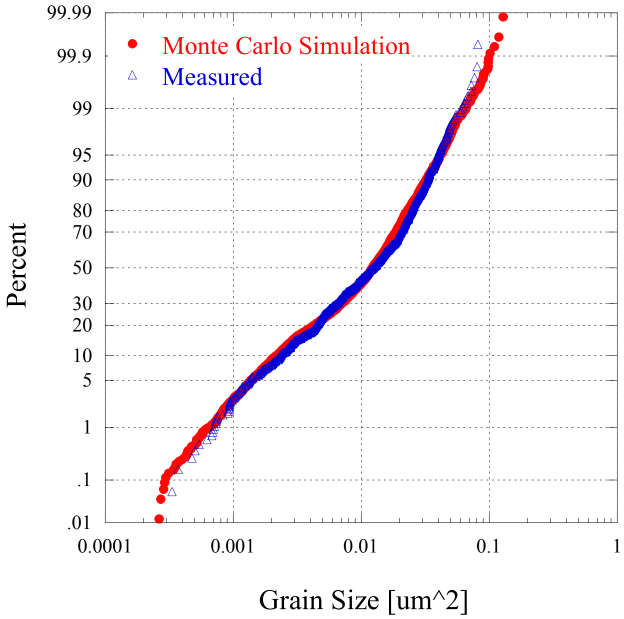

Figure 3.16 Grain size distribution in 0.18µm Cu lines with twins counted as separate grains. A bimodal lognormal distribution has been fitted to the experimental data using Monte Carlo simulation.

3.5.2 Texture Analysis

Unfortunately, texture analysis has not been performed on these 0.18µm Cu interconnects. However, several researchers measured the texture on lines with 0.25µm line width produced under very similar processing conditions [Vanasupa 1999, Hauschildt 2001, Besser 2001]. It has been observed that mainly four texture components occur in these Cu lines. {111} orientations are the main component. In addition, orientations due to sidewall nucleation and due to twinning, and a random component exist. Unfortunately, most of these results are qualitative and do not provide accurate volume fractions for each texture component. Various volume fractions for the {111} orientations have been reported depending strongly on processing condition [Tracy 1993, Rosenberg 2000, Proost 2000]. The samples closest to the test structures used in this study showed approximately 40% of {111} oriented grain interfaces and 20-25% sidewall orientations. As obtained from grain size analysis, approximately 15% of the grain interfaces have a twin orientation. Thus, the random component is assumed to be between 20% and 25%.

3.6 SIMULATION PROCEDURE

The observed void size and EM lifetime statistics were simulated by considering experimental, process and mass transport parameters. All of these parameters are statistically distributed, i.e. their values follow a distribution function with certain median and standard deviation values. Their variations need to be examined, since they contribute to the variations in void sizes and lifetimes. These parameters include the temperature as well as current variation in the EM oven and the variation in line dimensions. Results on their analysis are included in the following. The experimentally obtained statistics of each parameter were used to create random distributions using the appropriate distribution function. All simulated distributions consisted of 500 data points. These random distributions were then included in the simulation using the appropriate mass transport equations together with additional distributions describing mass transport variations.

3.6.1 Test System Characterization

Variations in temperature as well as in electrical stressing current occurring in the EM ovens might influence EM behavior in submicron interconnects. Thus, an analysis of their statistics is required.

Resistive thermal devices (RTDs) as well as thermocouples (TCs) were used to examine the temperature variation in the EM ovens. Four different ovens were used in this study. However, most experiments were performed in one oven, which was selected for a detailed temperature characterization. This oven was heated several times to a nominal value of 300°C to examine the variation of temperature over time, as a function of location within the oven and between heating cycles. TCs were inserted into the oven with the measurement tip freely suspended in the heated chamber. Their temperature reading was recorded manually at random times during each test consistently showing 300°C ± 1°C. Since the accuracy of TCs is less compared to RTDs and the recording has to be done manually, RTD measurements were performed for a more detailed analysis.

The RTDs manufactured by Omega® are thin film elements made from platinum (Pt), which have a resistance of 500Ω at 0°C [OMEGA Engineering, Inc]. They were packaged similarly to the EM samples, so that their resistance value could be recorded automatically over time. The temperature can be extracted from the resistance values. The temperature traces of two RTDs, which were at different locations during the same heating cycle, are included in Figure 3.17. It can be seen that the temperature remains very stable. Sudden temperature adjustments lead to jumps in the resistance curve as seen at about 445h. These jumps are the result of outside influences, for instance it has been observed that they sometimes coincide with the start of a new experiment in a neighboring oven. Still, these temperature adjustments are rather small. A normal distribution fit through the data points results in mean temperatures of 294.6°C and 293.6°C and standard deviations of only 0.15°C and 0.18°C for DUT 14 and DUT 43, respectively.

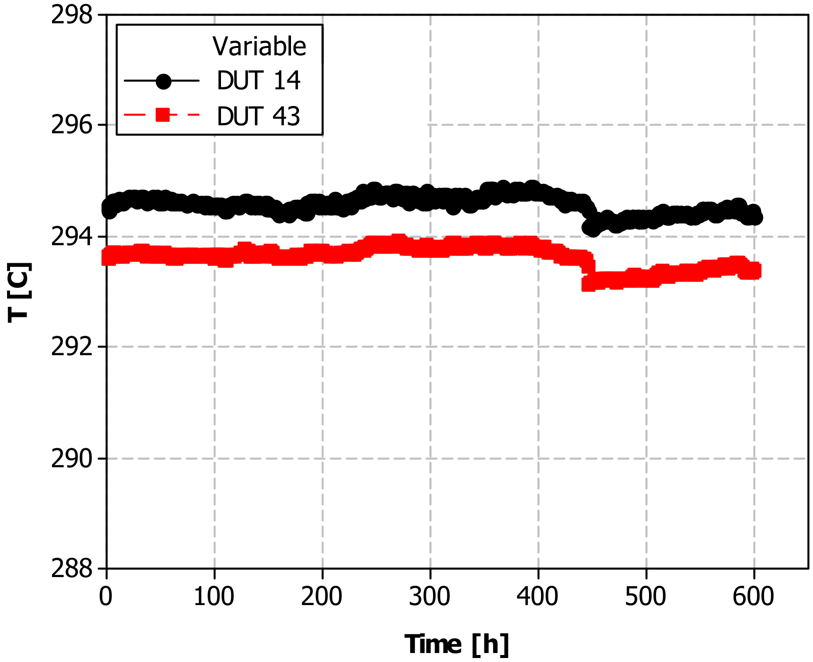

Figure 3.17 Temperature traces of two RTDs, which have been at different locations during the same heating cycle.

Interestingly, the mean values of the RTDs were consistently lower compared to the TCs. Since the packages are attached to boards, which could transfer heat to the outside, it is possible that the temperature in the oven is higher than directly in the packages. Whether the packaging process affects the measurement of the RTDs has been evaluated by comparing two packaged RTDs with two unpackaged RTDs, which were inserted into zero force insertion boards. Since these boards are only available for a low temperature oven, this experiment was performed at 175°C. The resistance traces are shown in Figure 3.18. Obviously, no statistical difference resulting from packaging could be observed between these RTDs. Hence, the difference between RTDs and TCs is most likely the result of the above mentioned thermal conduction of the boards.

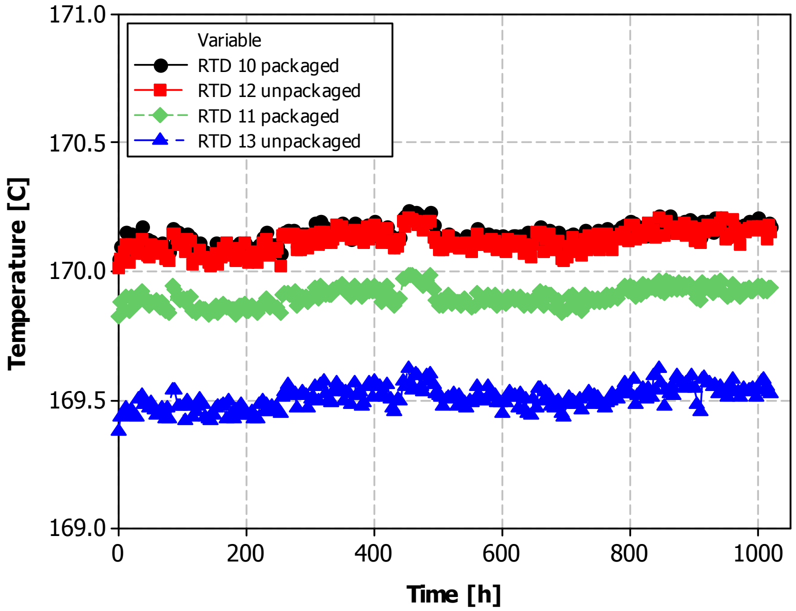

Figure 3.18 Temperature traces of two packaged and two unpackaged RTDs. No statistical differences could be observed between them.

The repeatability between different heating cycles has been tested by keeping 5 RTDs in the same positions for approximately 5 heating cycles to the nominal value of 300°C. The temperature traces for one DUT for 6 cycles are included in Figure 3.19. The mean temperatures for each experiment are obtained by considering measurements after 2 hours, when the temperature appears to be stabilized. Figure 3.20 shows the distributions of the mean temperatures for all 5 RTDs. The repeatability appears to be excellent with the mean values of different heating cycles having small standard deviations between 0.2°C and 0.73°C.

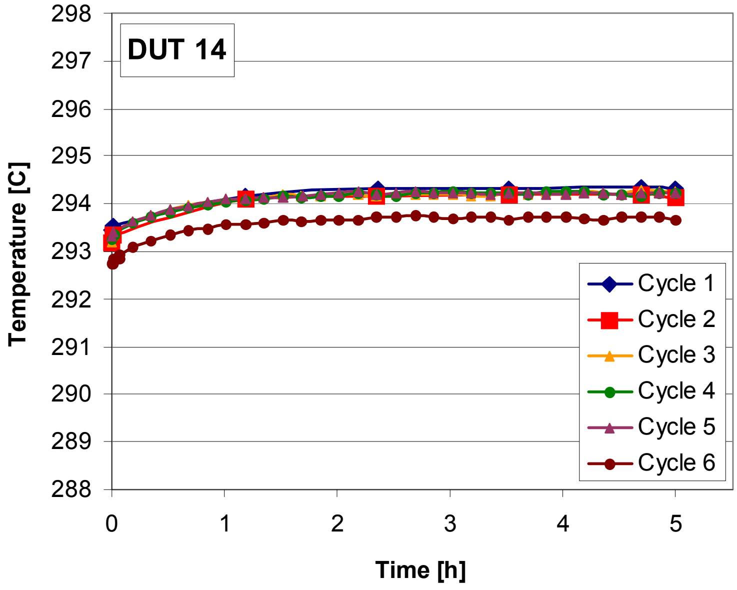

Figure 3.19 Temperature traces for one DUT located in the same position in one oven for 6 heating cycles.

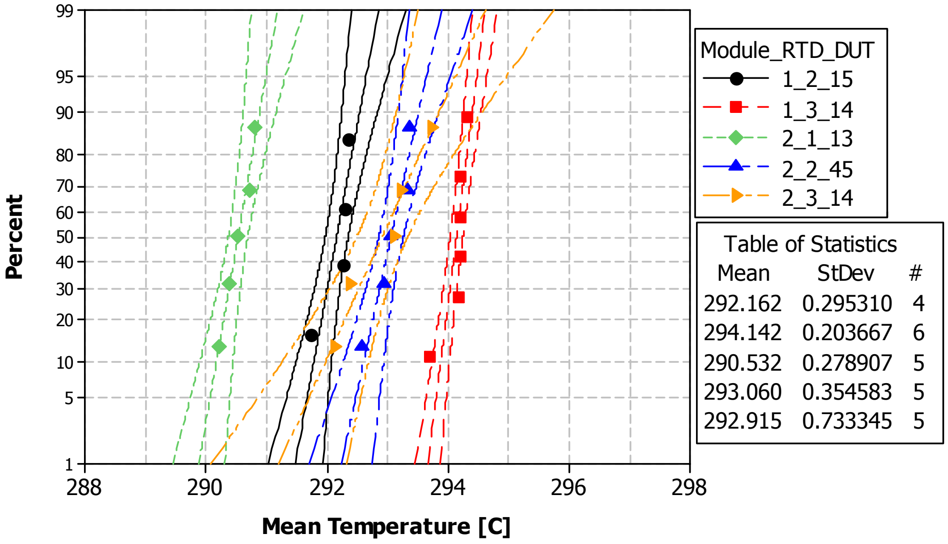

Table of Statistics

Mean	StDev	#
292.162	0.295310	4
294.142	0.203667	6
290.532	0.278907	5
293.060	0.354583	5
292.915	0.733345	5

Figure 3.20 Distributions of mean temperature values for five DUTs. Each DUT was located in the same position in one oven for approximately 5 heating cycles.

The largest variations in temperature result from different oven positions and above mentioned temperature adjustments over time. The former has been examined by cycling the RTDs through various oven positions. Figure 3.21 displays the temperature traces obtained for 19 different oven positions. In total, 43 different positions have been measured out of 60 existing ones. The mean temperature values of these are plotted in Figure 3.22. A normal distribution fit through the data results in a standard deviation of approximately 0.94°C.

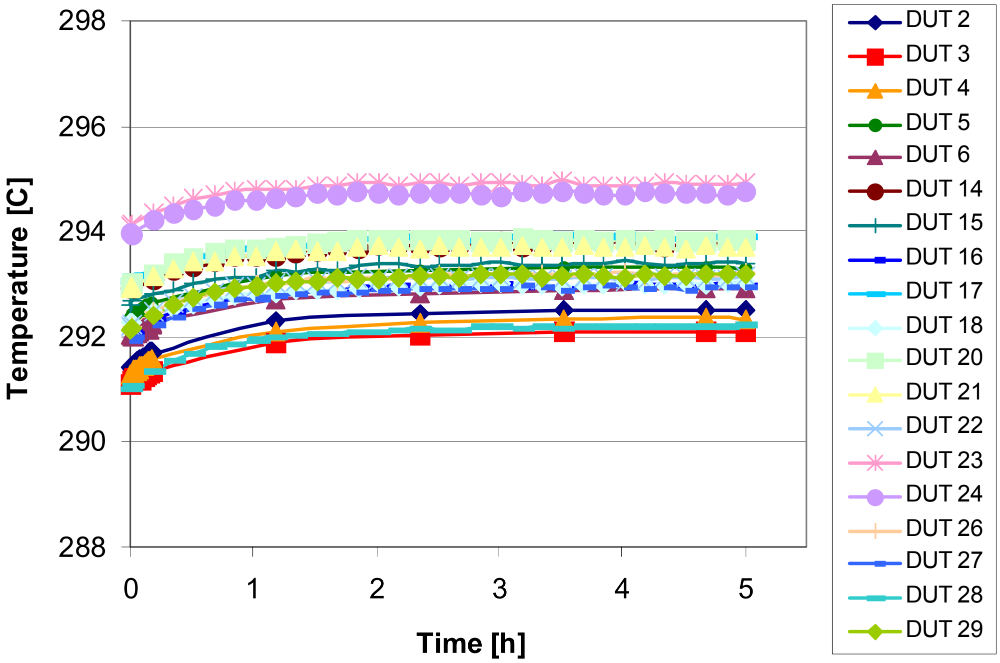

Figure 3.21 Temperature traces for 19 DUTs located in different positions within one oven.

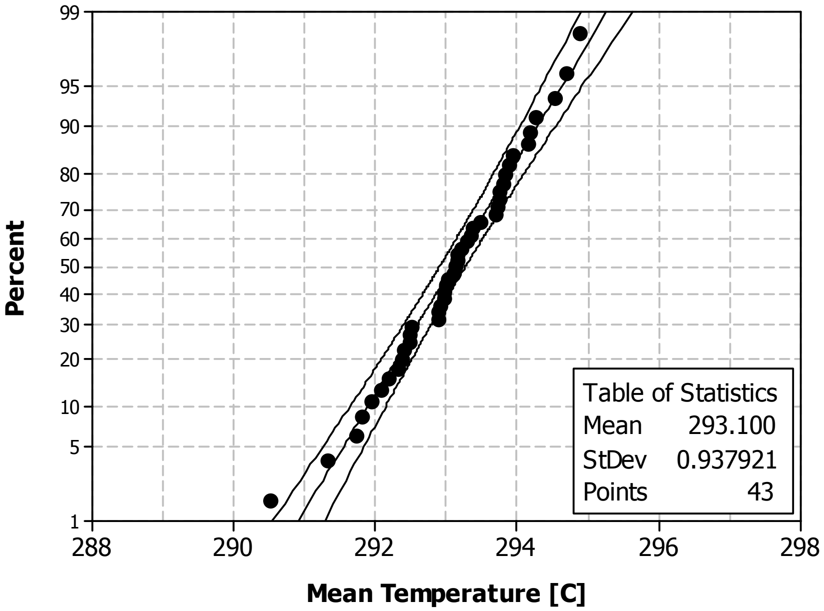

Figure 3.22 Distribution of mean values of temperature measurements of different oven positions. The temperature measurements at 43 different positions are included.

Unfortunately, the difference in temperature between ovens has not been characterized by RTD measurements yet. However, TCs, which were included in all tests, showed 300°C ± 1°C for all ovens. Hence, it is expected that the variation between ovens is not very large, which is reasonable, since all ovens were calibrated using TC measurements.

The mean values of all RTD temperature measurements are included in Figure 3.23. The standard deviation increases to approximately 1.25°C. The temperature ranges from just above 290°C to just below 297°C with the average of all temperature means being 293.1°C. The vendor specified the temperature range to be approximately 1% of the target temperature. Hence, in the case of 293°C, a deviation of ±3°C is expected, which agrees well with the experimentally observed data. In this study, values for the mean and standard deviation have been chosen to be 293°C and 1.5°C, respectively. The slightly higher standard deviation of 1.5°C - as compared to the measured value of 1.25°C - was chosen since not all 60 possible DUT positions across all used ovens were characterized in this study.

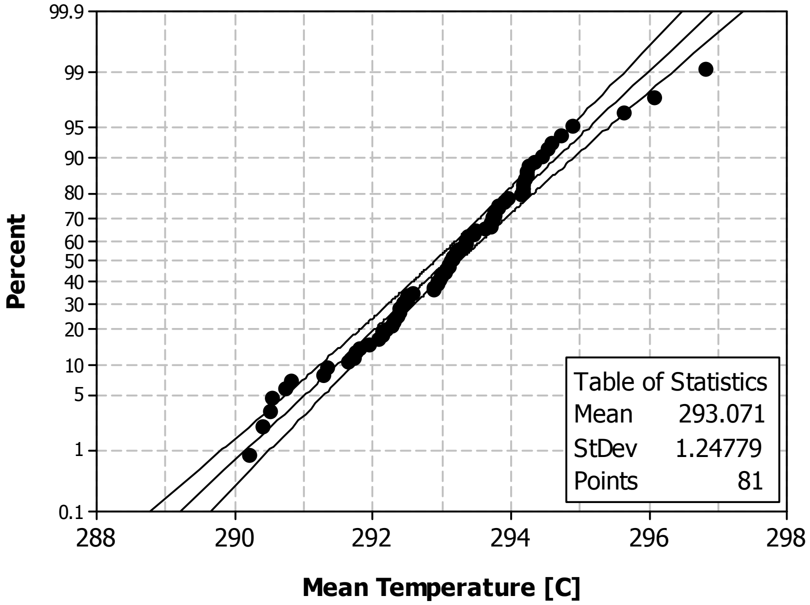

Figure 3.23 Distribution of mean values of all RTD temperature measurements.

The electronic stability of the system has not been analyzed in detail. However, the vendor specifies the current source to have a resolution of 2.5µA in the range of currents used in this study. Since the majority of experiments were performed with a current of 0.67mA, the range is less than ±0.4%. Due to this small value, the variation of testing currents has been neglected in this study. It is generally accepted that electrical stressing currents in commercially available test systems are well controlled.

3.6.2 Variations in Line Dimensions

Since a large number of samples were needed for the statistical analysis of variations in EM lifetimes, samples were used from 5 different lots for the EM experiments, namely D62375.1, D62429.1, D63327, U31275 and D76814. All lots received identical processing conditions, but the desired processing variations explained above. The EM behavior of all these lots is comparable. However, the cross sectional areas of barrier layer and Cu have a variation induced by process variations. Since these areas define the current density in the line as well as influence the size of the final void, approximately 120 cross sections were measured to obtain their statistics. For the characterization of dimensional variation, samples were taken from 4 lots only, since most experiments were performed using these lots. Several measurements of samples from the 5th lot, D76814, showed comparable results to lot D62375.1. Hence its dimensional statistics were used in future calculations involving samples from D76814.

SEM images of two cross sections are included in Figure 3.24 with (a) and (b) showing samples from lots D63327 and U31275, respectively. Distributions of Cu cross-sectional area, Ta cross-sectional area, line height, average line width, and line width on top of the line are shown in Figures 3.25 to 3.29. The latter three include only the Cu portion of the line excluding the barrier layer. The average line width has been obtained from measurements of the trench width at the bottom, the middle and the top. Since the lines are tapered, the width increases from bottom to top, showing a smaller value for the average line width compared to the width on top. A normal distribution function with 80% two-sided confidence bounds has been used to fit the dimensional parameters. It is obvious that all dimensions show variations within the lot as well as between lots. The corresponding statistics of the dimensional parameters as a function of lot are included in

Tables 3.1 through 3.5. Although none of these variations are large, they cannot be neglected when examining the statistics of EM lifetimes.

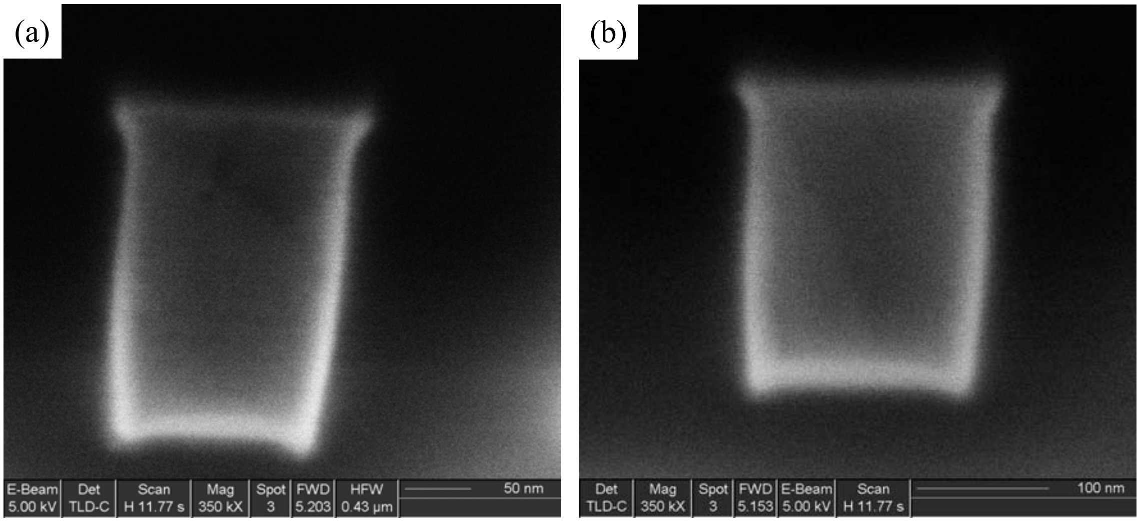

Figure 3.24 SEM images of interconnect cross sections. The samples were taken from (a) lot D63327 and (b) lot U32175.

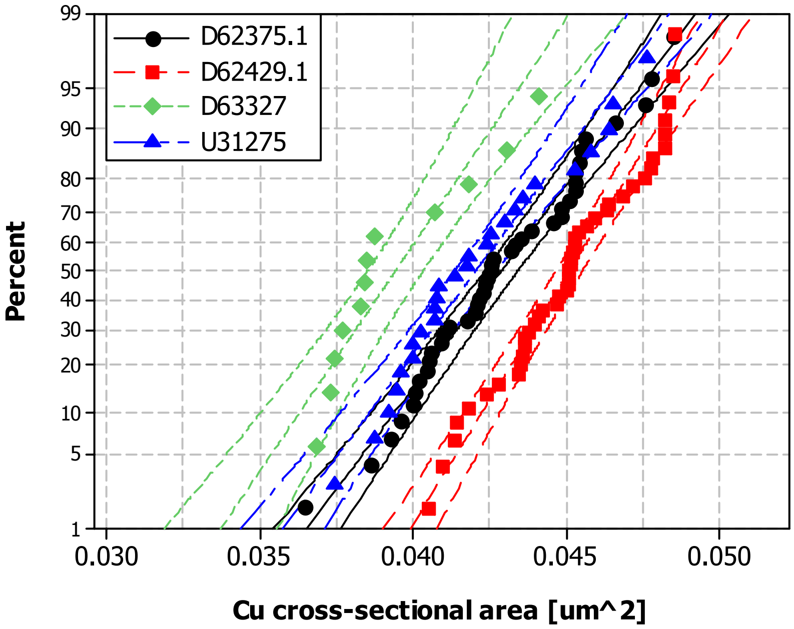

Figure 3.25 Distributions of Cu cross-sectional area as a function of lot.

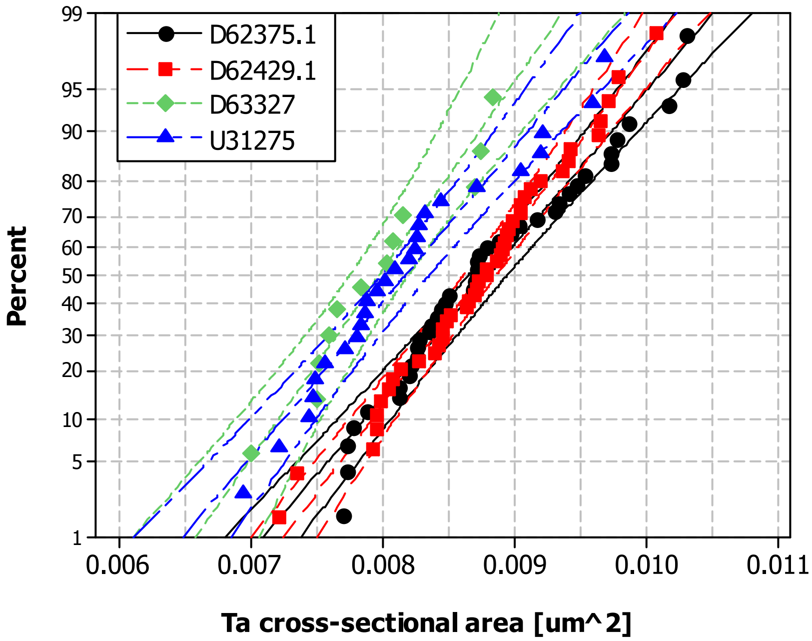

Figure 3.26 Distributions of Ta cross-sectional area as a function of lot.

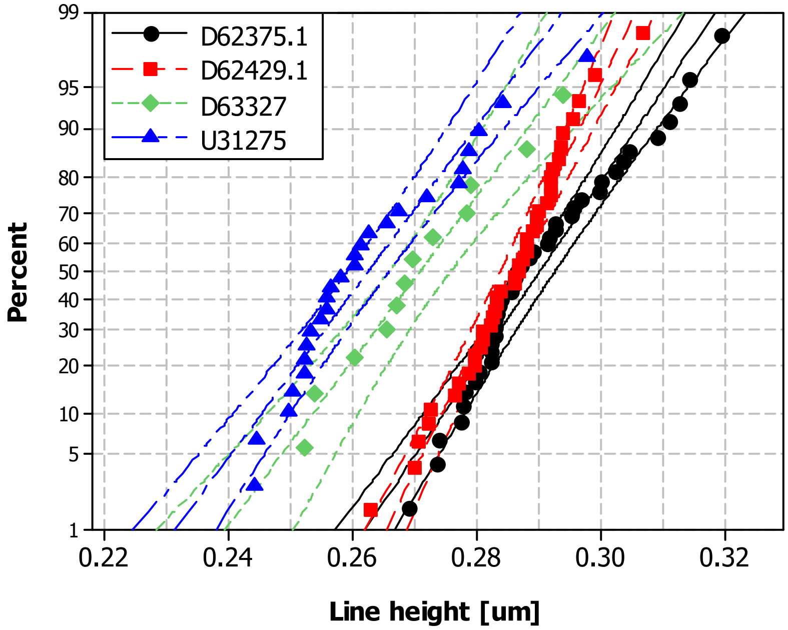

Figure 3.27 Distributions of Cu line height as a function of lot.

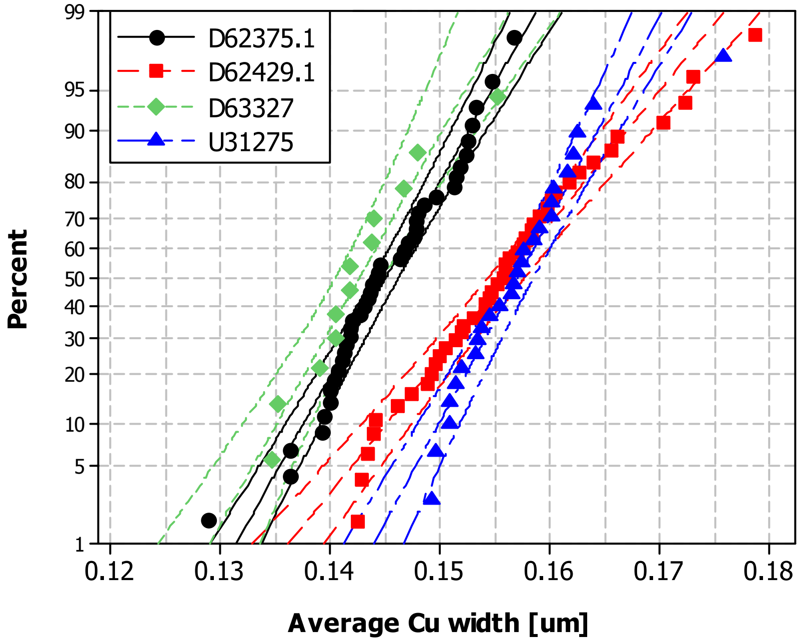

Figure 3.28 Distributions of average Cu width as a function of lot. The average value has been obtained by measuring the line width on the bottom, in the middle and on top of the trench.

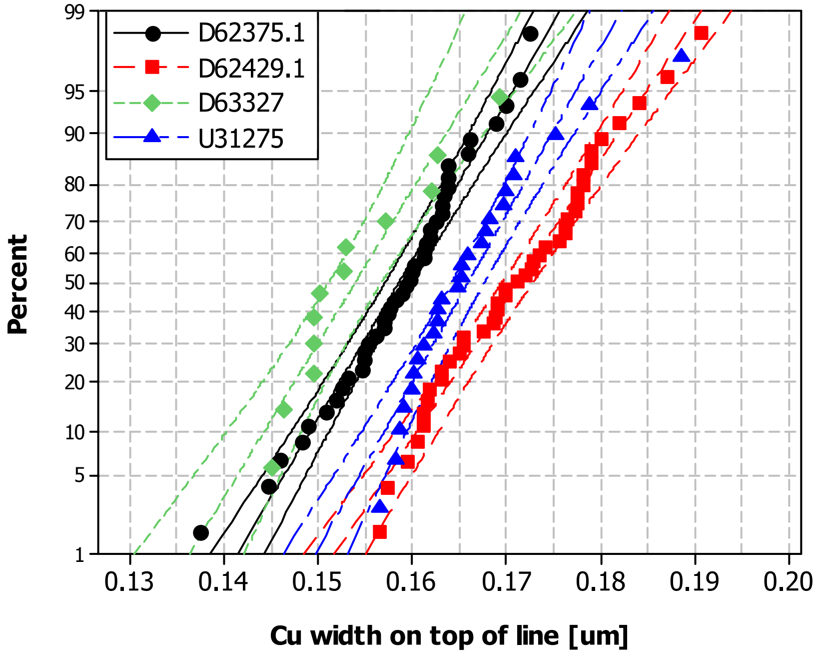

Figure 3.29 Distributions of Cu line width on top of the line as function of lot.

Table 3.1 Statistics of Cu cross-sectional area as a function of lot. All mean and sigma values are measured in μm^2

Cu x-sectional area	Mean	Lower Mean	Upper Mean	Sigma	Lower Sigma	Upper Sigma	Data Points
D62375.1	0.0429	0.0423	0.0434	0.00272	0.00234	0.00316	41
D62429.1	0.0451	0.0446	0.0455	0.00222	0.00192	0.00257	43
D63327	0.0394	0.0385	0.0403	0.00244	0.00184	0.00324	12
U31275	0.0420	0.0414	0.0427	0.00271	0.00224	0.00328	26

Table 3.2 Statistics of Ta cross-sectional area as a function of lot. All mean and sigma values are measured in μm^2. The last column contains the number of measurements obtained per lot.

Ta x-sectional area	Mean	Lower Mean	Upper Mean	Sigma	Lower Sigma	Upper Sigma	#
D62375.1	0.00880	0.00865	0.00895	0.000735	0.000634	0.000851	41
D62429.1	0.00874	0.00861	0.00887	0.000641	0.000554	0.000741	43
D63327	0.00797	0.00775	0.00819	0.000598	0.000441	0.000811	12
U31275	0.00817	0.00799	0.00836	0.000727	0.000602	0.000878	26

Table 3.3 Statistics of Cu line height as a function of lot. All mean and sigma values are measured in µm.

Cu line height	Mean	Lower Mean	Upper Mean	Sigma	Lower Sigma	Upper Sigma	Data Points
D62375.1	0.290	0.288	0.293	0.0121	0.0105	0.0140	41
D62429.1	0.285	0.284	0.287	0.0086	0.0075	0.0100	43
D63327	0.271	0.266	0.276	0.0135	0.0099	0.0184	12
U31275	0.262	0.259	0.266	0.0134	0.0111	0.0161	26

Table 3.4 Statistics of average Cu line width as a function of lot. The average value has been obtained by measuring the line width on the bottom, in the middle and on top of the trench. All mean and sigma values are measured in μm.

Cu line width (average)	Mean	Lower Mean	Upper Mean	Sigma	Lower Sigma	Upper Sigma	Data Points
D62375.1	0.145	0.144	0.146	0.00585	0.00504	0.00678	41
D62429.1	0.156	0.154	0.158	0.00849	0.00735	0.00981	43
D63327	0.143	0.140	0.145	0.00585	0.00433	0.00790	12
U31275	0.157	0.156	0.158	0.00563	0.00470	0.00675	26

Table 3.5 Statistics of Cu line width on top of the trench as a function of lot. All mean and sigma values are measured in μm.

Cu line width (top)	Mean	Lower Mean	Upper Mean	Sigma	Lower Sigma	Upper Sigma	Data Points
D62375.1	0.159	0.157	0.160	0.00736	0.00636	0.00851	41
D62429.1	0.171	0.170	0.173	0.00835	0.00722	0.00966	43
D63327	0.154	0.151	0.157	0.00757	0.00565	0.01014	12
U31275	0.166	0.164	0.168	0.00698	0.00584	0.00834	26

Chapter 4: Experimental Results

While the analysis of the microstructure in Cu interconnects was already included in the previous chapter, the experimental results of the EM tests will be discussed in this chapter. First, the electrical results will be examined, followed by a detailed analysis of the void evolution process. Furthermore, the void size statistics will be analyzed as a function of resistance increase and time. Subsequently, details on the average void growth as a function of time will be provided.

4.1 ANALYSIS OF RESISTANCE TRACES DURING EM

The resistance change as a function of time as typically observed during an EM experiment is shown in Figure 4.1. All samples displayed in the plot have been tested to a 100% resistance increase failure criterion. Initially, the resistance decreases slightly due to annealing effects within the Cu microstructure. After a period of small increase, the resistance generally jumps by 5 to 10%. Subsequently, the resistance increases approximately linearly with time. Deviations from linearity can be attributed to changes in void shape during void growth as well as to a dependence of Cu diffusion on grain orientation.

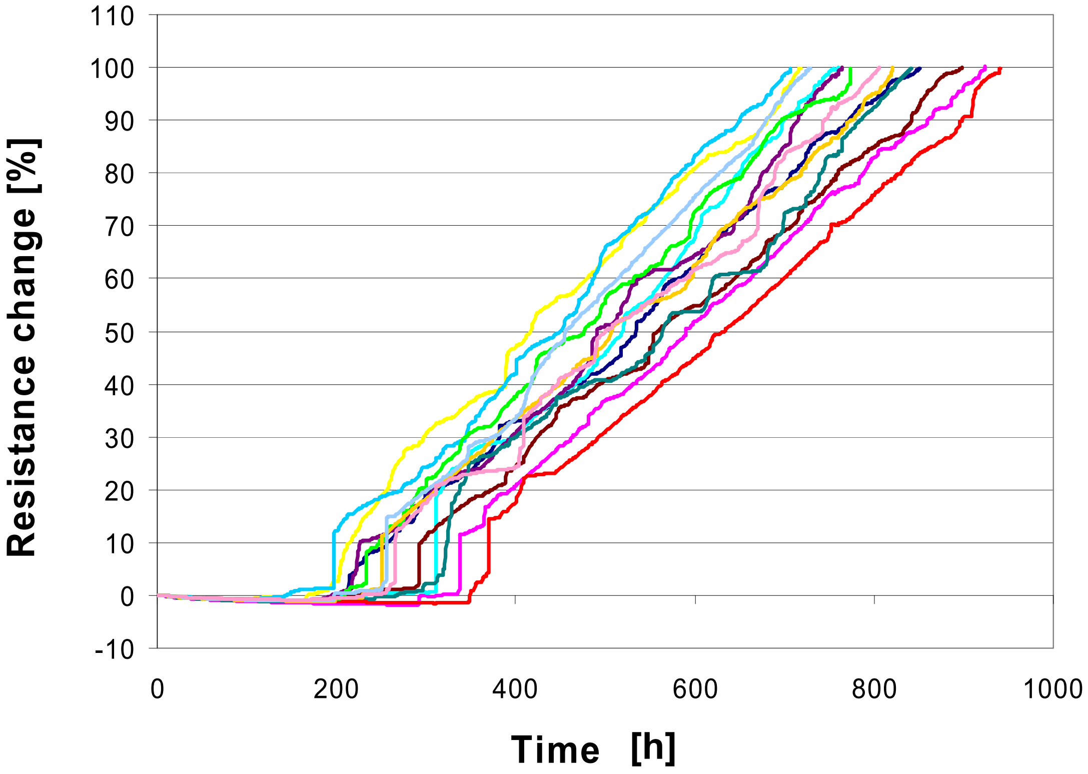

Figure 4.1 The resistance change as a function of time as measured during an EM test.

4.1.1 Analysis of statistical characteristics of EM lifetimes

For each DUT, the time needed to obtain a 10% resistance increase has been acquired. The time distribution is shown as cumulative percentage plots in Figures 4.2-4.5 with different distribution functions used to fit the data. In Figure 4.2 a lognormal distribution function has been applied, in 4.3 a normal distribution function, in 4.4 a Weibull distribution, and in Figure 4.5 a Smallest Extreme Value distribution function was used. The confidence bounds shown in all plots are 80% two-sided limits. A lognormal distribution with a median of 297h and a sigma of 0.24 clearly provides the best fit to the data. All other distribution functions show systematic deviations of the experimental data for smaller and larger percentage values. Following the analysis in

Chapter 3, a certain number of data points are required to distinguish between different distribution functions. Assuming lognormal statistics, Equation (3.3) with a sigma value of 0.24 yields a number of approximately 600 data points, which are needed to statistically examine the EM lifetimes with 2% accuracy. The plot in Figure 4.2 contains 264 data points. Hence, for very sound statistical analysis additional data points would be needed. However, the total number of data points acquired here is deemed sufficient since the qualitative deviation of certain distribution functions already can give a good indication on which function provides the best description.

Traditionally, EM data has been described using a lognormal distribution function. Whether this choice is the most appropriate has been addressed previously [Towner 1990, Lloyd 1991, Gall 1999, Gall 2001]. The issue has mostly been discussed in terms of scaling. In the case of EM, the statistics depend on which test structure is used, i.e. is only one failure link tested or several links in series. If a one-link distribution can be described by a certain distribution function, such as a lognormal distribution, a multi-link test result cannot follow the same function, since distribution functions generally do not scale. In this case, a multi-link result would then follow a "multi"-lognormal distribution. Only single links were tested in this study. However, as Lloyd *et al.* [1991] pointed out, any one-link test structure can theoretically be cut in half and represent a test structure with two links of shorter line length each. If the statistics of the original distribution follows lognormal characteristics, the shorter lines cannot obey lognormal behavior. Hence, the question arises which line length is the correct choice to obtain lifetime distributions with truly lognormal behavior and not multi-lognormal characteristics, if such a length even exists.

Gall *et al.* [1999, 2001] ruled out the Weibull distribution as a possible function to fit EM data. Since this is the only major distribution that actually scales, experimental results from EM tests with various numbers of links were examined with regard to a Weibull distribution fit. The experimental data showed that the spread in the distribution decreased with increasing number of tested links. In a Weibull distribution function, the shape parameter represents the variation of a distribution. However, since a Weibull distribution scales, that parameter does not change as a function of tested lines, and should remain identical for all multi-link tests. Due to this discrepancy between experiment and theory, a Weibull distribution cannot be the underlying distribution function for EM lifetime data.

A strong argument for a lognormal or most likely multi-lognormal distribution function can be made when considering the diffusion process of Cu ions under EM. As mentioned above, the major diffusion path is along the top interface of the line. When traveling along that interface, Cu encounters a variety of different interfacial structures depending on the grain orientation. These influence the diffusivity of Cu, i.e. the diffusivity of Cu varies with grain structure. It has been seen in Chapter 3 that lognormal statistics provide a good description for grain size distributions. Hence, due to the influence of microstructure on the EM process, it could be concluded that a lognormal distribution provides the underlying statistics for EM lifetimes. Whether a more appropriate terminology would involve multi-lognormal statistics remains unanswered. However, due to the excellent fit of a simple lognormal distribution function to the experimental data, this function was used to describe all EM data reported in this study. In general, the difference between simple lognormal and multi-lognormal statistics only shows up at the tails of the distributions. Again, a very large sample size is needed to properly distinguish between the two assumptions.

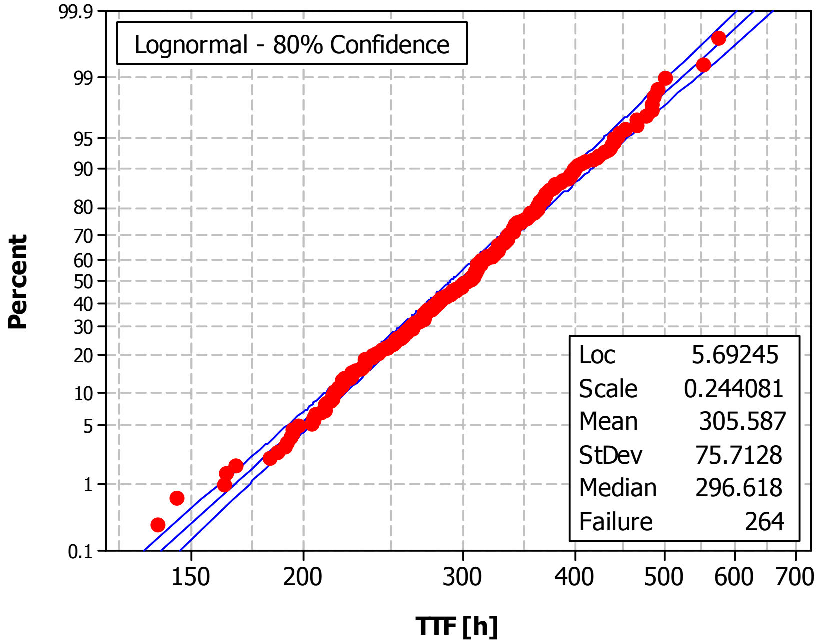

Figure 4.2 Cumulative percentage plot of the time distribution needed to obtain a 10% resistance increase with a lognormal distribution function used to fit the data.

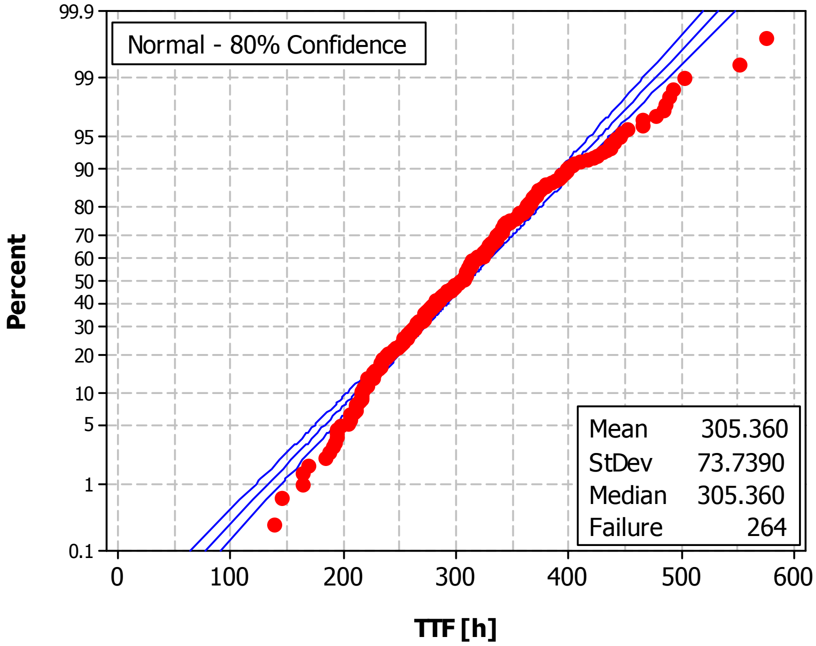

Figure 4.3 Cumulative percentage plot of the time distribution needed to obtain a 10% resistance increase with a normal distribution function used to fit the data.

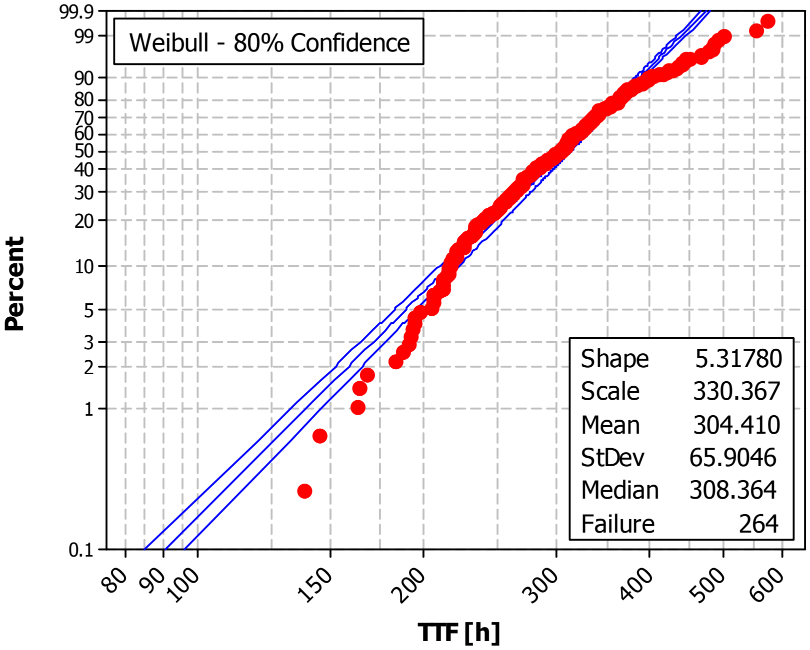

Figure 4.4 Cumulative percentage plot of the time distribution needed to obtain a 10% resistance increase with a Weibull distribution function used to fit the data.

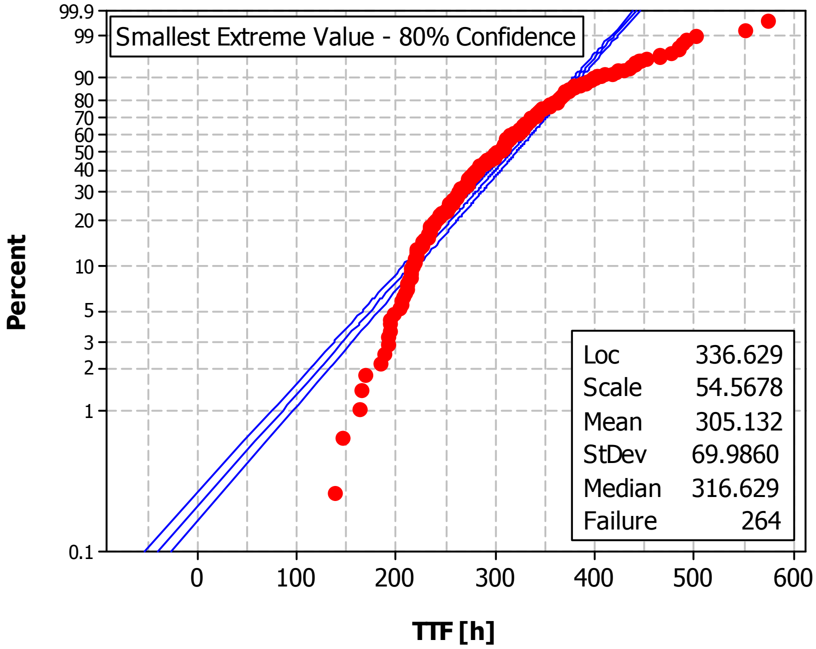

Figure 4.5 Cumulative percentage plot of the time distribution needed to obtain a 10% resistance increase with a Smallest Extreme Value distribution function used to fit the data.

4.1.2 Analysis of EM Lifetimes as a Function of Die Location

Immature process control or out-of-spec process steps could induce slight differences in processing conditions across the wafer. For instance, a larger amount of etchants at the periphery of the wafer would induce larger etch rates towards the edge of a wafer. Thus the height of the interconnect structures would show variations depending on the location on the wafer. Likewise, the CMP process as well as the electroplating process could be affected by variations of chemical concentrations across the wafer. PVD processes, such as the barrier and seed deposition, could be affected by shadowing from the trench side walls leading to thickness variations. Furthermore, temperature variations during annealing could influence the interface qualities as a function of location on the wafer. All of these process variations could potentially induce differences in EM lifetime across the wafer, affecting the statistical analysis of EM data.

It is most probable that any processing issues are circular symmetric. Thus, the analysis performed here is limited to a comparison between samples form edge and center dies of the wafers. A sample is defined to be from the wafer edge when it was taken from within 4.5cm of the wafer's border. A maximum of 84 identical V1M2 structures can be obtained per wafer resulting in 38 center and 46 edge dies, respectively. The EM lifetime distributions of center and edge samples for a 10% resistance increase failure criterion are shown in Figure 4.6. In this case, all 78 samples were taken from one wafer. The number is smaller than 84, since some parts broke during packaging or did not yield acceptable resistance values at the start of the experiment. No difference can be observed between samples from wafer center and wafer edge. Figure 4.7 displays all 10% data separated according to die location. Again, no significant difference in EM behavior of center and edge dies can be discerned. Thus, the influence of die location on EM lifetime statistics appears to be negligible in this study.

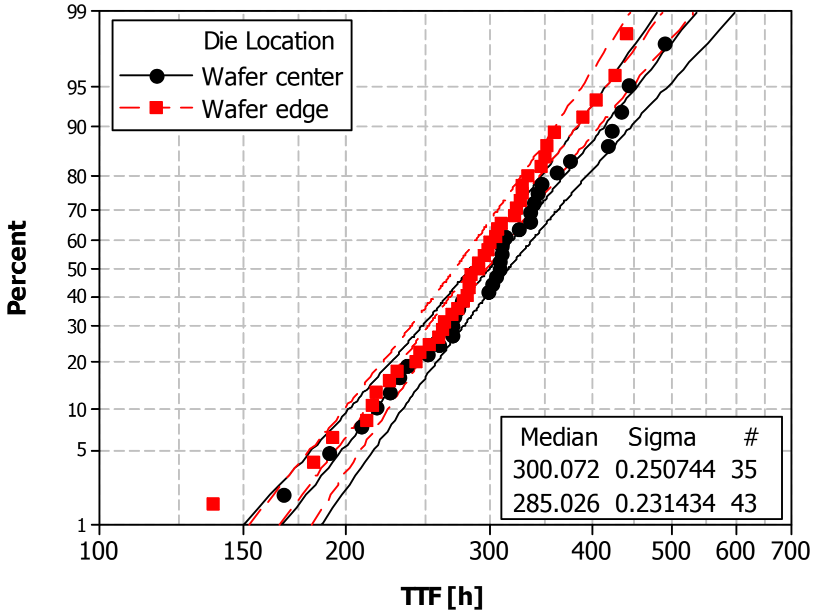

Figure 4.6 EM lifetime distributions corresponding to a 10% resistance increase failure criterion as a function of die location. All samples were taken from one wafer.

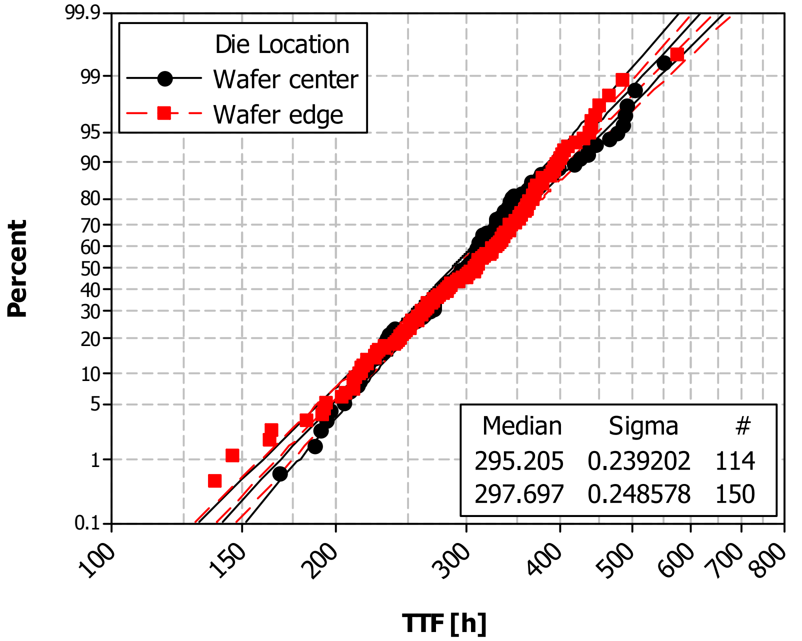

Figure 4.7 EM lifetime distributions corresponding to a 10% resistance increase failure criterion as a function of die location. All tested samples across multiple wafers and lots are included.

4.2 EM LIFETIME DISTRIBUTIONS AS A FUNCTION OF RESISTANCE CRITERION

The time distributions needed to obtain a first resistance increase, 1%, 5%, 10%, 20%, 30%, 50%, 70% and 100% resistance increase are plotted in Figure 4.8. The time to first resistance increase has been obtained manually for each resistance trace. It can be seen that the median time to failure increases with increasing resistance criterion, since it takes more time to reach a larger resistance change. Interestingly, the slope of the distributions changes as a function of resistance criterion, i.e. sigma decreases with increasing resistance criterion. Figure 4.9 contains a plot of sigma as a function of median lifetime. The fit through the data is purely empirical and for illustrative purpose only . The equation used is of an exponential form:

$$f(t) = a + b(1 - \exp(-(\frac{t}{\tau})^{c})) \tag{4.1}$$

In this case, the parameters a and c have been set to 0.135 and 1. The choice of these parameters will be discussed further below. It needs to be mentioned that the line fit is not valid before the first resistance increase data point, since no additional data points could possibly exist before a first resistance increase due to the nature of this measurement. The continuation of the fit is only shown for illustrative purpose. The plot clearly shows the decrease of sigma from approximately 0.32 to 0.14. Thus, the variation in lifetimes is becoming smaller with larger median times to failure. The sigma value appears to have asymptotic behavior at long times with the minimum sigma being approximately 0.14 for the test structure used in this study.

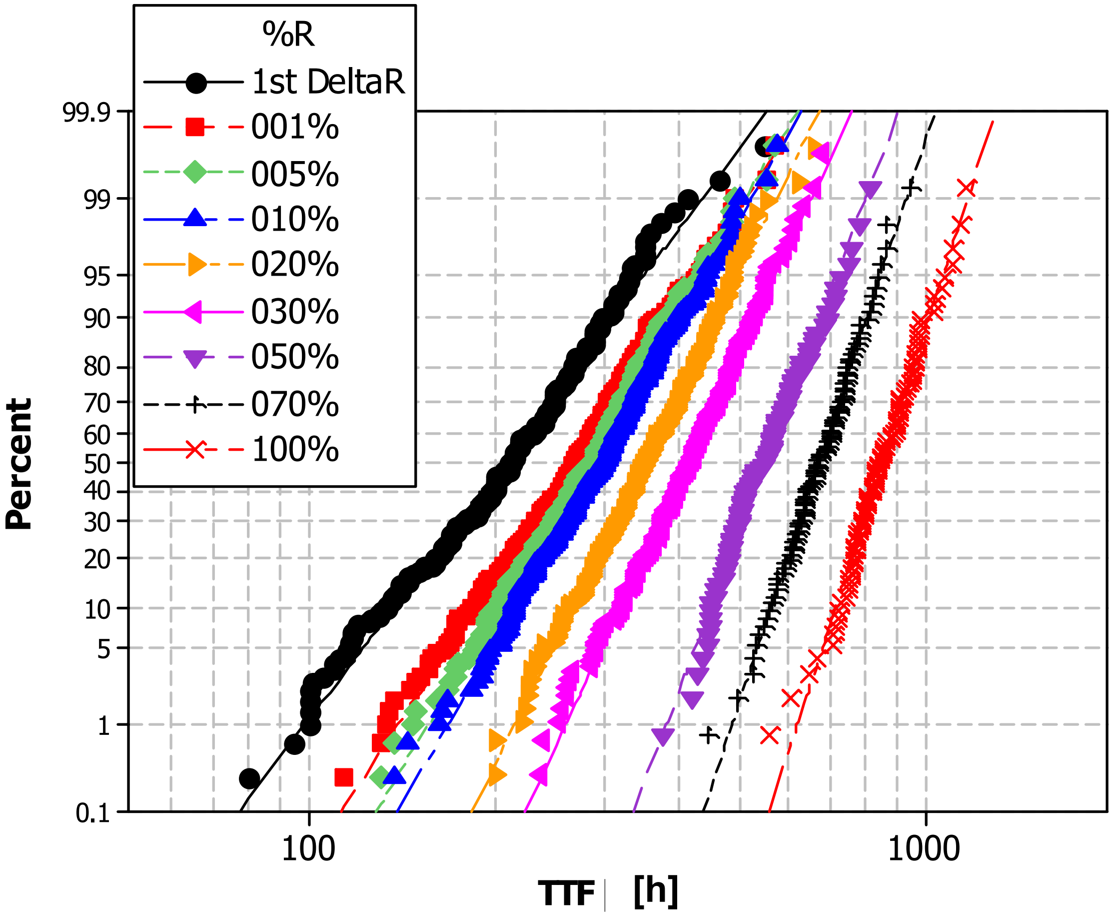

Figure 4.8 EM lifetime distributions as a function of resistance increase.

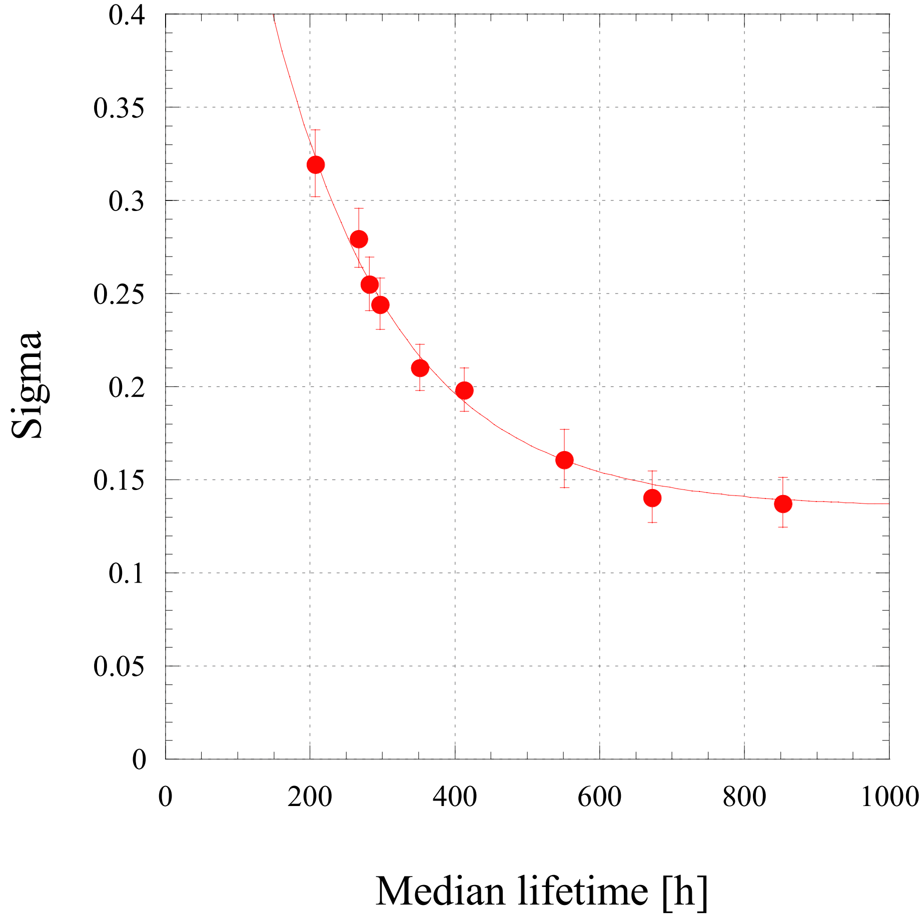

Figure 4.9 Sigma of EM lifetime distributions as a function of median time to failure.

4.3 DESCRIPTION OF VOID EVOLUTION DURING EM

In order to understand the statistical behavior of EM lifetimes, the void evolution during EM was analyzed. Four stages were identified, namely void formation, void evolution at the interface, first resistance increase and continuous void growth. SEM images typical of each stage are shown in Figures 4.10(a)-(d).

Results from the image analysis show that void formation occurs at the interface between Cu and SiN_x, usually away from the cathode end. The initial void formation site appears to be at junctions of grain boundaries with the interface. Different Cu grain orientations can influence Cu diffusivities at the interface and thus induce a flux divergence leading to void formation. Likewise, in addition to mass transport along the interface, diffusion along the grain boundaries can influence the amount of Cu ions flowing in and out of the interface/grain boundary junction. Thus, depending on the grain boundary, a flux divergence can be induced. The possibility of mass transport along grain boundaries and the dependence of interfacial mass transport on Cu orientation can explain the statistical distribution of the initial voids with respect to the distance from the cathode end.

In the second stage, the void grows at the interface towards the cathode end of the line. Due to a continuous flux of Cu ions along the interface, the initial voids refill, leading to void evolution towards the cathode end. When the void arrives at the cathode end, the final flux divergence site is reached, where the barrier layer between via and line prevents additional Cu to leave the via and fill the void. Subsequently, the void grows at the cathode end.

The first resistance increase occurs when the void reduces the Cu cross-section of the line to a large extent forcing the current to pass through a small area. In the case shown in Figure 4.10(c) the void already spans the whole line and covers most of the via. The connection between the via and the Cu portion of the line is very small, forcing the current through a small area. The jump in the resistance traces appears to occur when the void completely covers the via, i.e. there is no remaining Cu connection between the via and the line.

The last stage of void evolution is depicted in Figure 4.10(d). The void grows past the via and continuously along the line. Since the barrier layer is left intact, the current continues to flow through the structure and an entirely open circuit is prevented.

In this stage, the resistance of the line increases about linearly, proportional to the rate of Cu depletion at the cathode end.

It needs to be mentioned that all samples analyzed in this study showed the final failure void at the end of the line. While it has been observed that voids occasionally lead to failure of the line by growing down to the bottom of the line prior to reaching the end, this has not been the case for the voids observed here. Void evolution behavior similar to the one described above was observed by several researchers [for instance: Meyer 2002, Liniger 2002, Zschech 2004]. It has to be pointed out that some of these studies investigated dual damascene structures, whereas the results presented in this chapter were obtained with single damascene samples. In Chapter 6, the effects of dual damascene processing on EM lifetime statistics will be discussed.

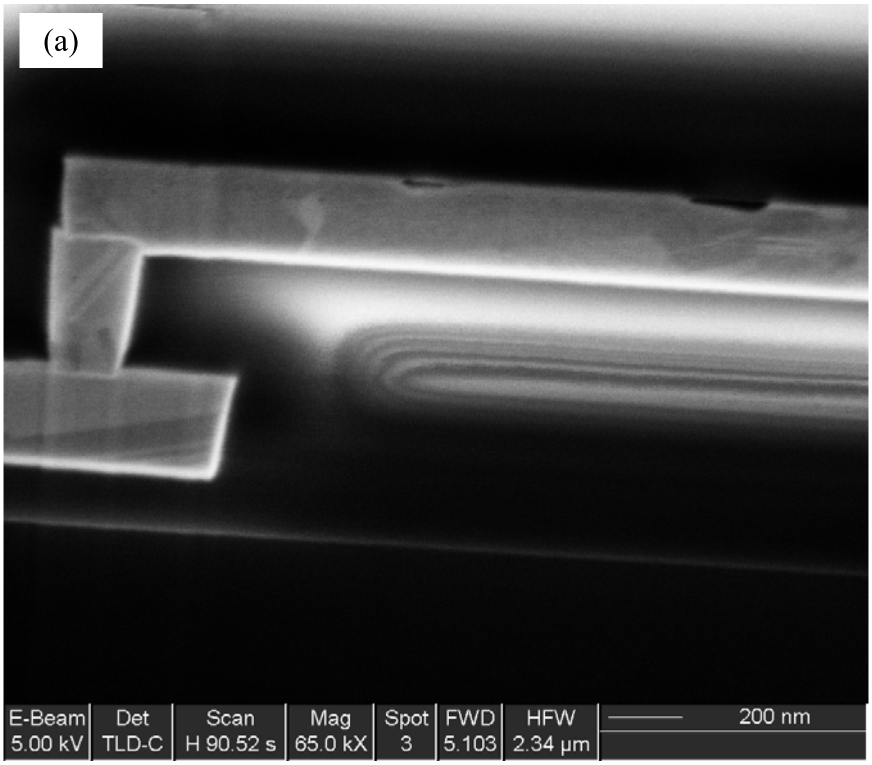
(a)
E-Beam 5.00 kV
Det TLD-C
Scan H 90.52 s
Mag 65.0 kX
Spot 3
FWD 5.103
HFW 2.34 µm
200 nm

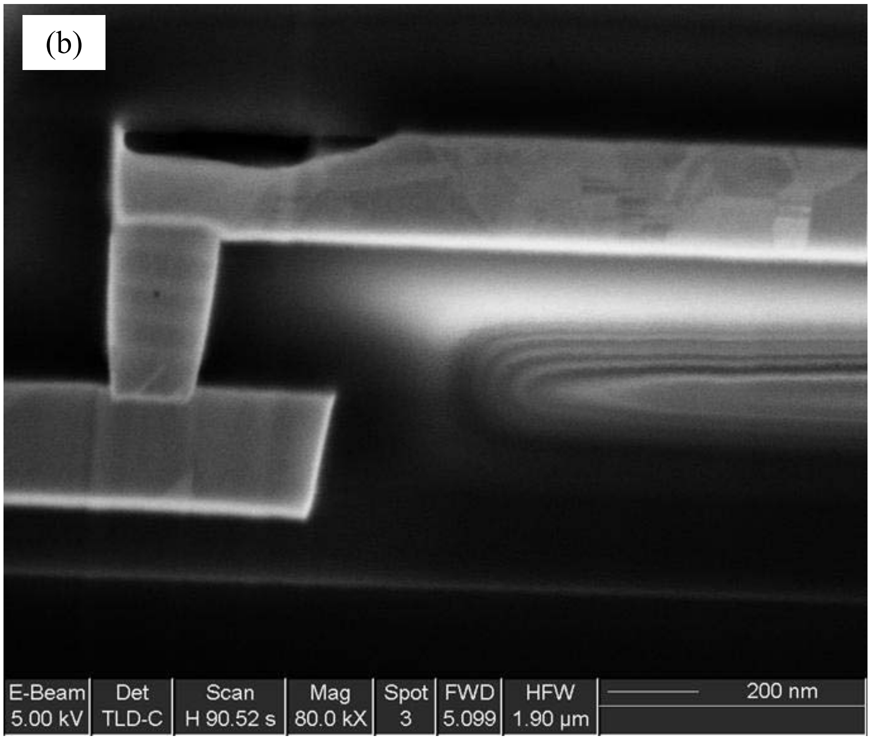
(b)
E-Beam 5.00 kV
Det TLD-C
Scan H 90.52 s
Mag 80.0 kX
Spot 3
FWD 5.099
HFW 1.90 µm
200 nm

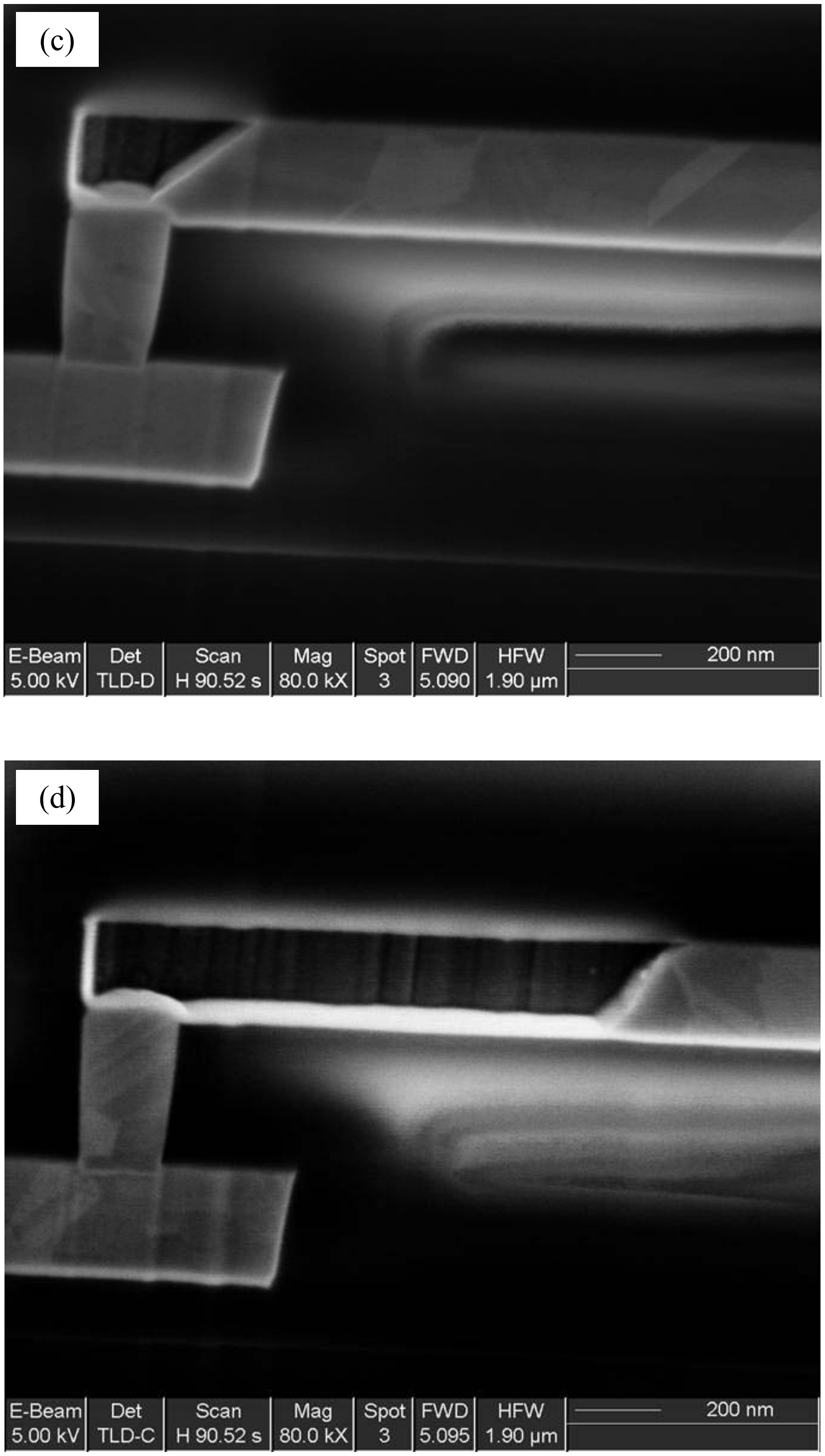

Figure 4.10 FIB images illustrating four stages of void evolution: (a) Void formation, (b) Void evolution at interface, (c) 1st resistance increase, (d) Continuous void growth.

4.4 VOID SIZE ANALYSIS AS A FUNCTION OF RESISTANCE CRITERION

For a more quantitative analysis, the void area distributions were obtained as a function of resistance increase with at least 10 data points per condition. For the 30% resistance increase criterion, 24 data points were acquired. Representative SEM images of voided metal lines together with corresponding resistance traces are shown in Figures 4.11 to 4.18 for various resistance increases. Figures 4.11 to 4.13 display 12 images of voids, which have just passed the first resistance increase. 8 images of 10% voids are included in Figures 4.14 and 4.15. Figures 4.16 to 4.18 show 4 images each for a 30%, 50% and 100% resistance increase criterion. A larger number of images have been included for the first two conditions, since the void shapes show a larger diversity at smaller resistance increases.

It needs to be mentioned that the void size analysis was performed on samples from different lots. The 30% void data was obtained using lot U32175, the 100% data originated from lot D63327, and the 10% and 50% tests were conducted with samples from D62375.1. The data corresponding to the first resistance increase was obtained using lot D76814. Again, the EM behavior of all lots was observed to be similar enabling a direct comparison of void data obtained from different lots. However, slight variations in line dimensions as a function of lot have been observed as discussed in the previous chapter. For accuracy, these have been taken into account during the simulation part of this study as will be discussed in Chapter 5.

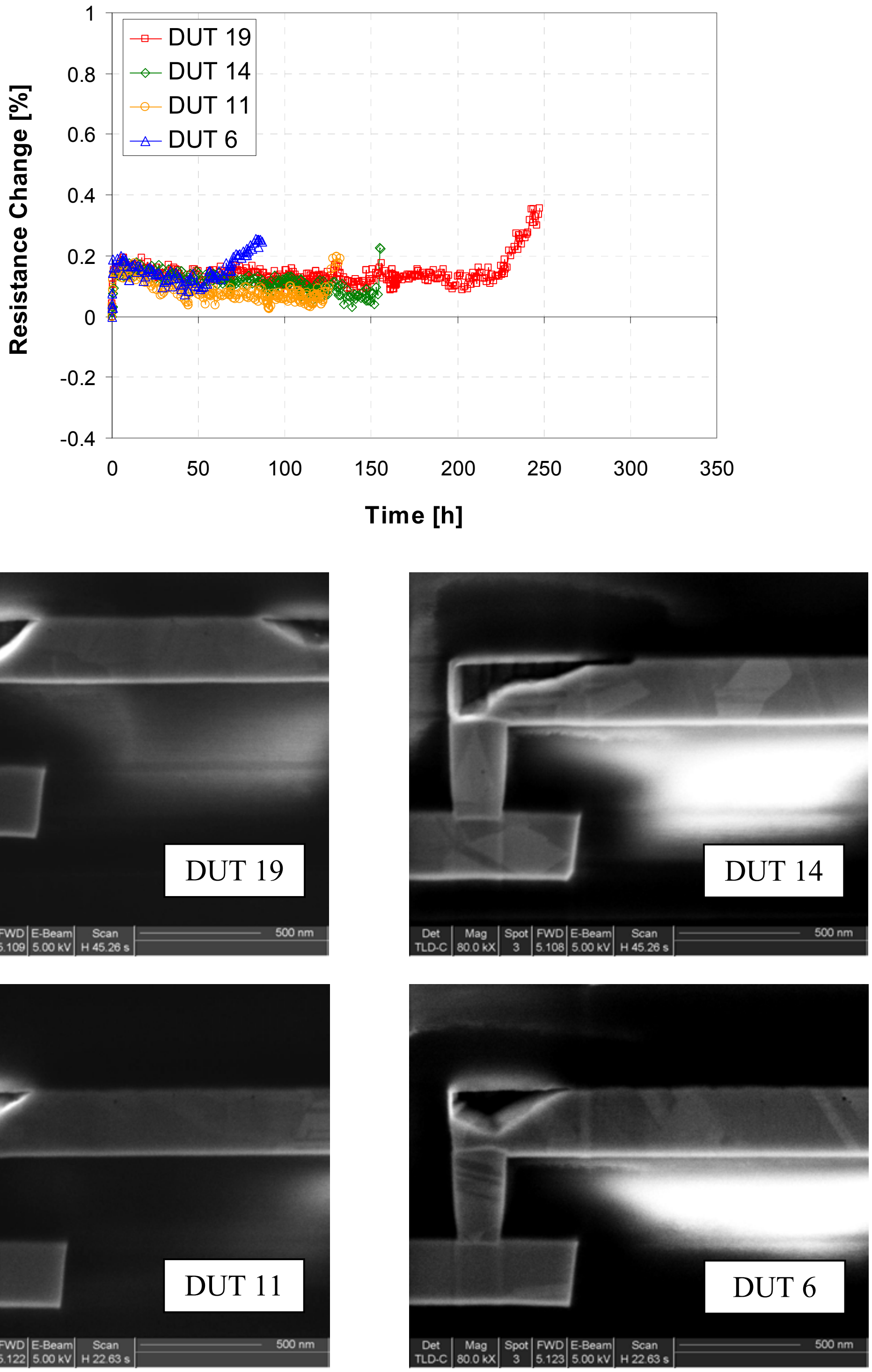

Figure 4.11 The resistance change as a function of time for selected DUTs tested to the first resistance increase, and corresponding SEM images showing the voids at the cathode end of the interconnects.

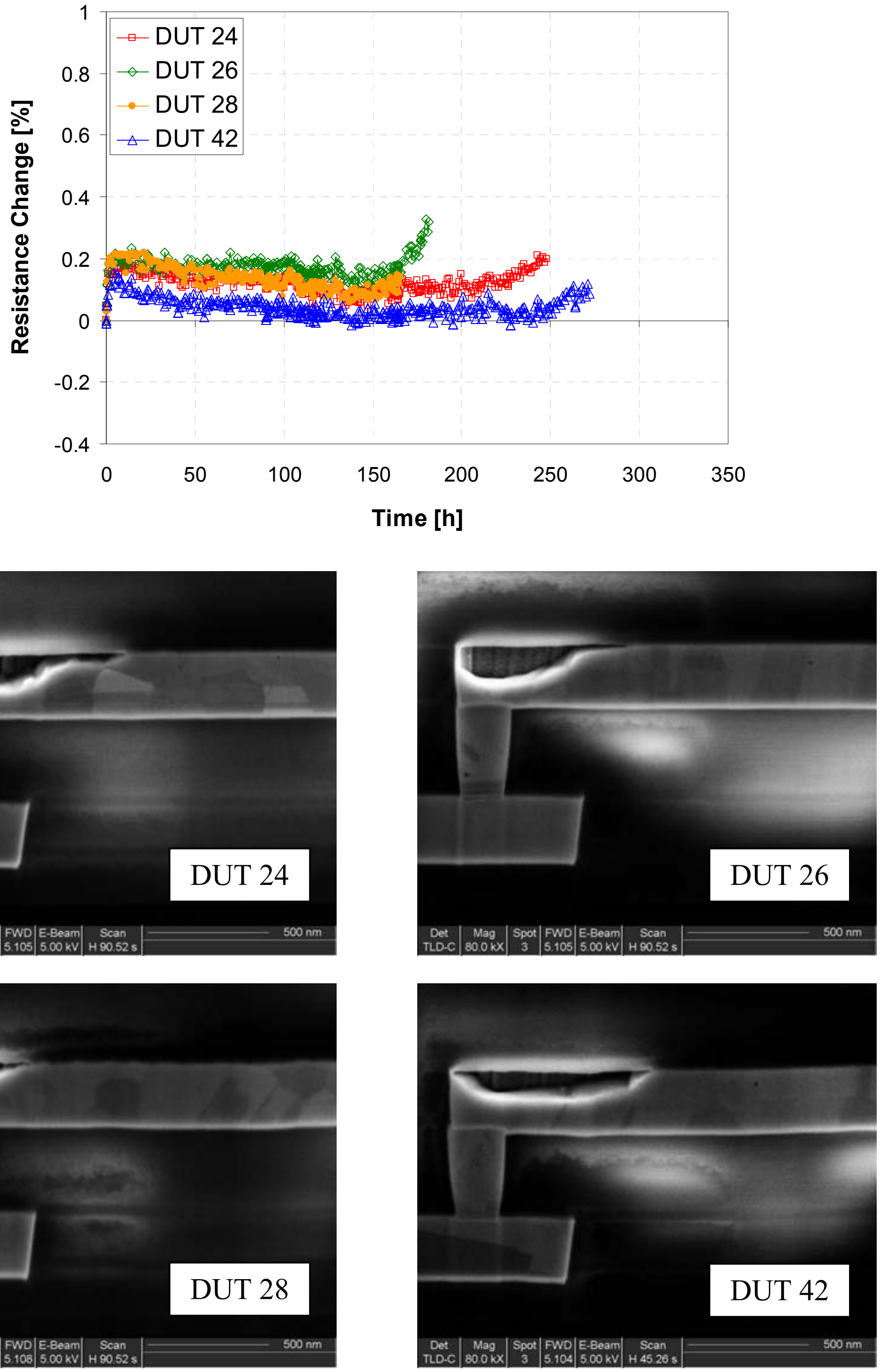

Figure 4.12 Additional results for samples tested to the first resistance increase. A larger number of resistance traces and corresponding SEM images are shown due to larger variations in void shape at shorter times.

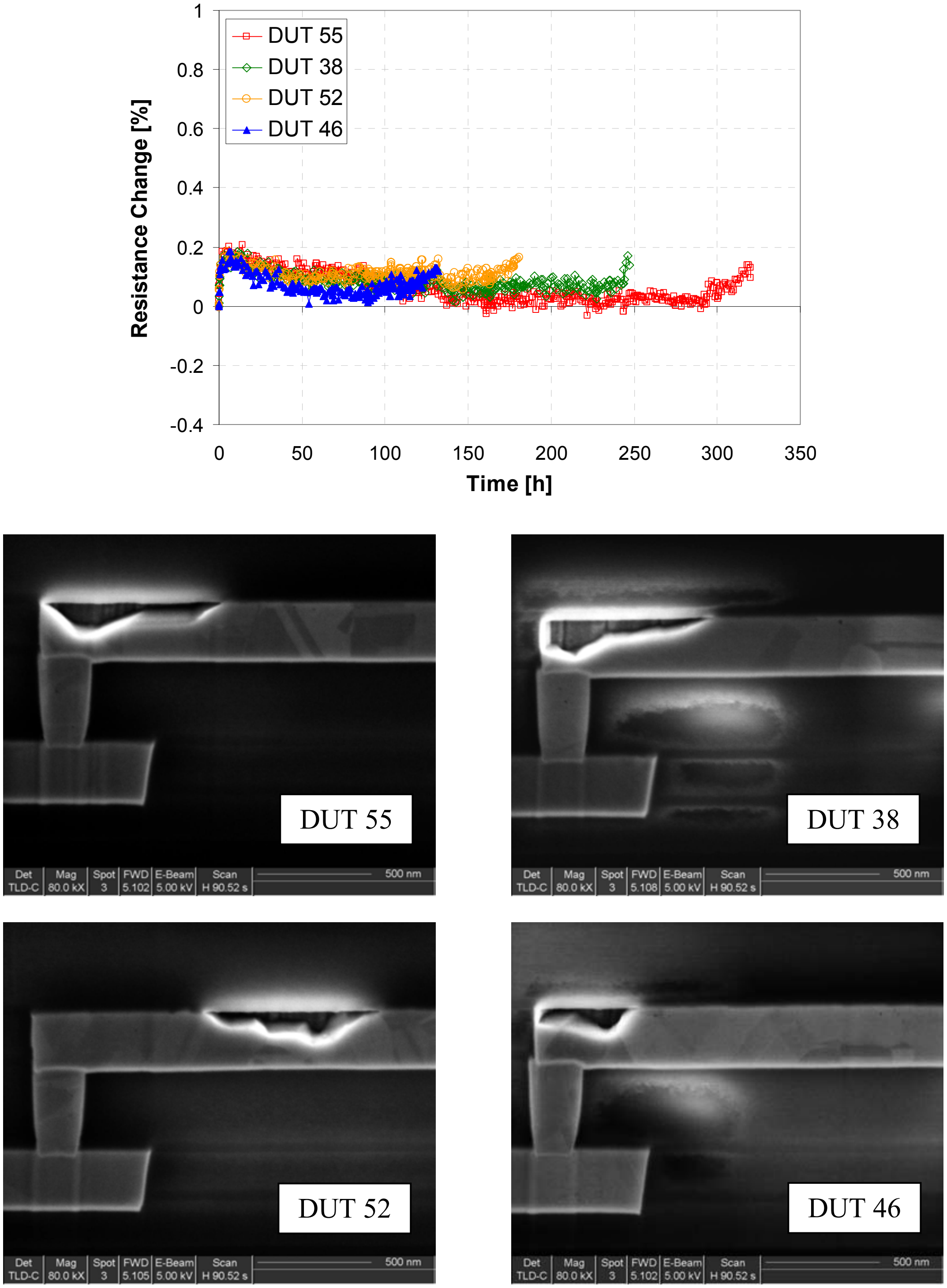

Figure 4.13 Additional results for samples tested to the first resistance increase. Resistance traces and corresponding SEM images are shown for selected DUTs.

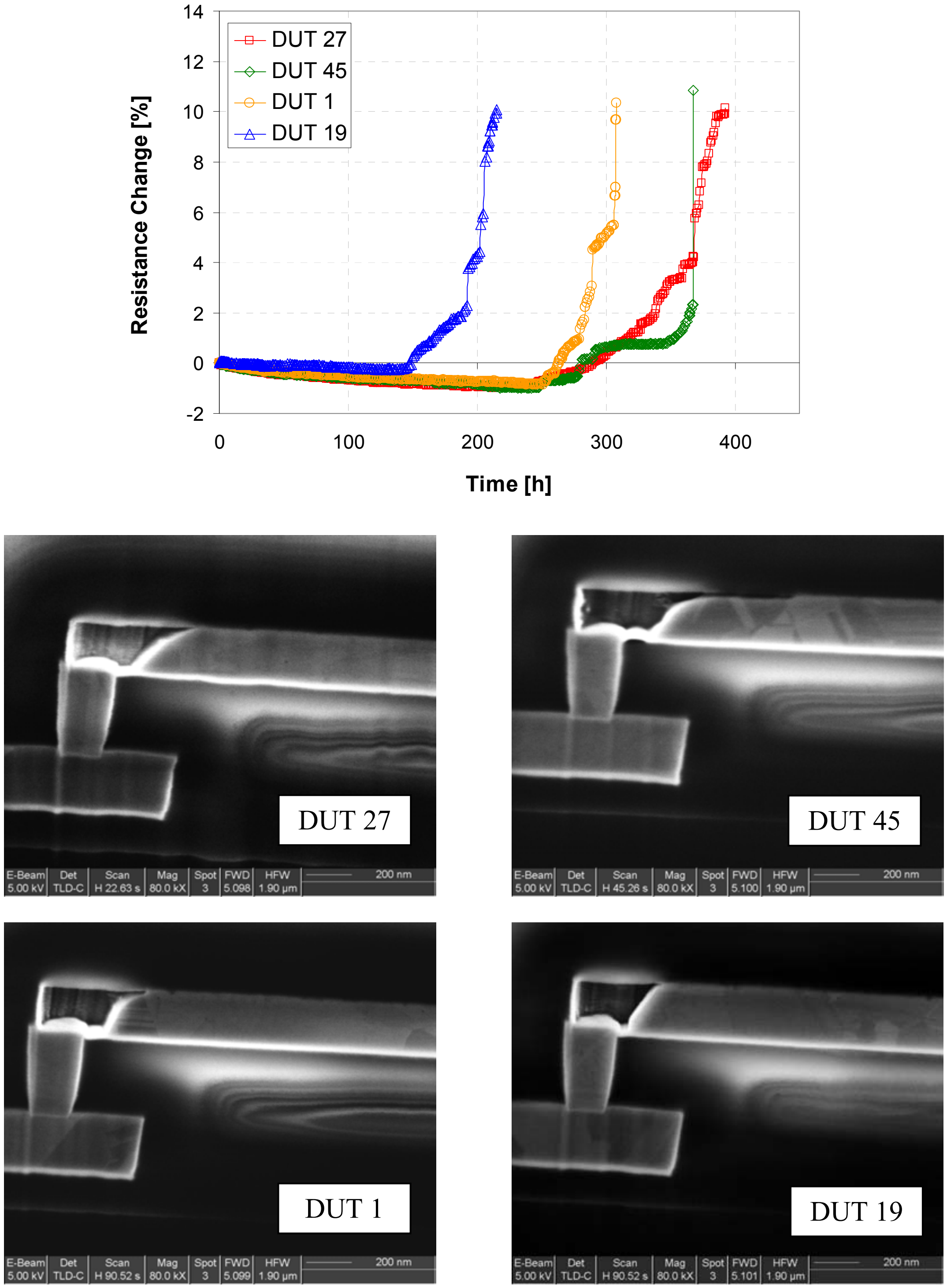

Figure 4.14 The resistance change as a function of time for selected DUTs tested to a 10% resistance increase, and corresponding SEM images showing the voids at the cathode end of the interconnects.

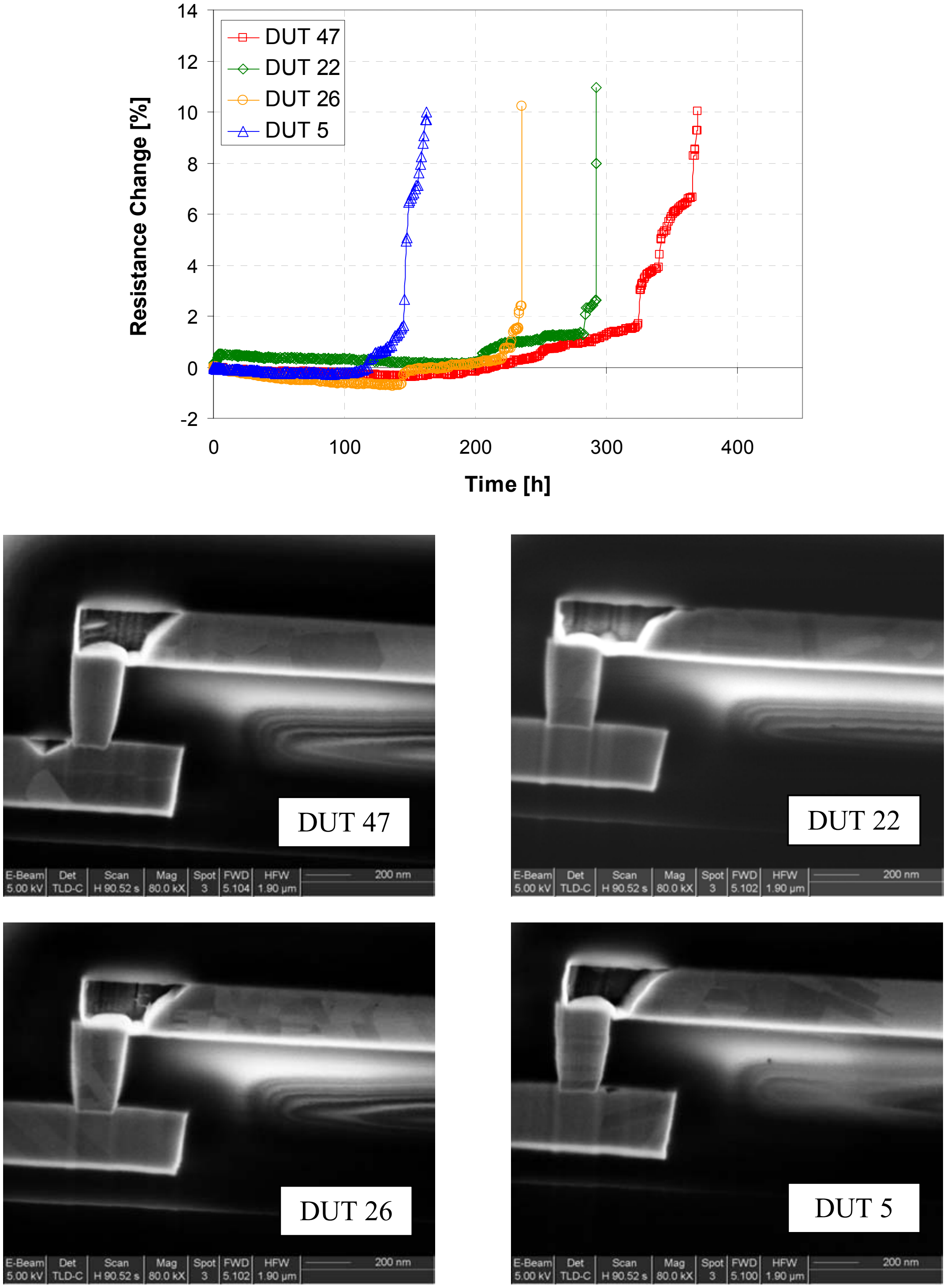

Figure 4.15 Additional results for samples tested to a 10% resistance increase. A larger number of resistance traces and corresponding SEM images are shown due to larger variations in void shape at shorter times.

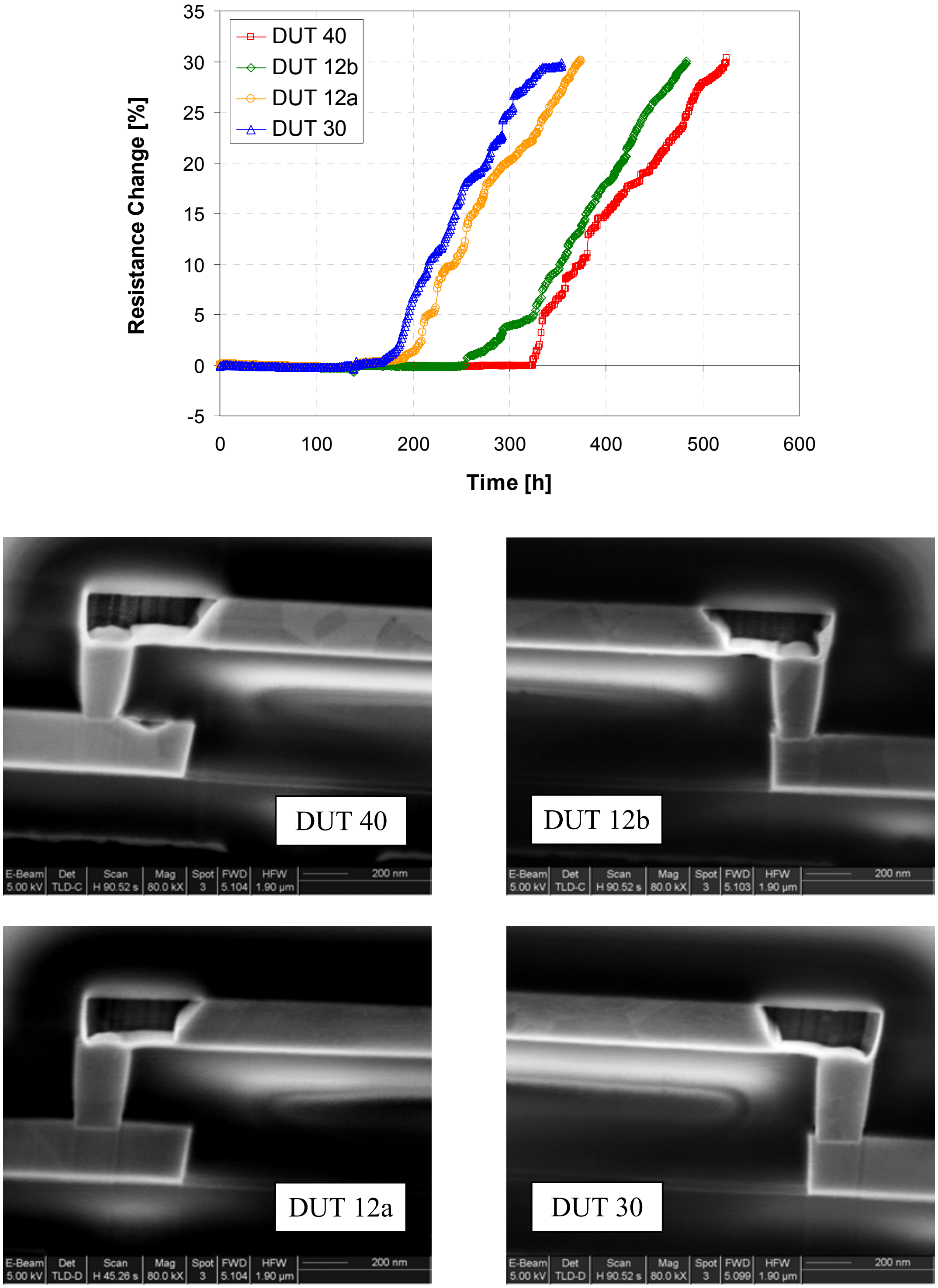

Figure 4.16 Resistance traces and corresponding SEM images for selected DUTs tested to a 30% resistance increase.

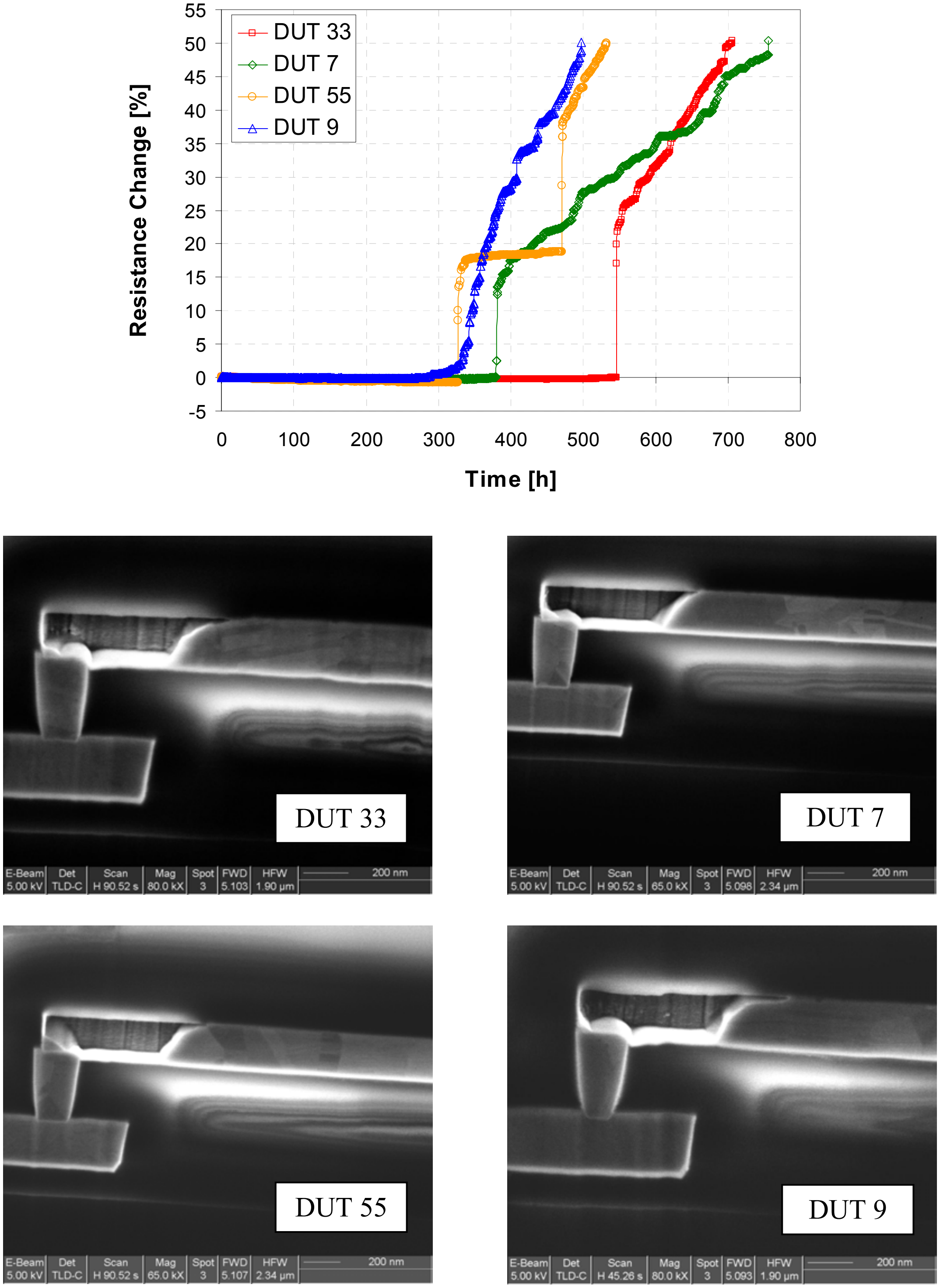

Figure 4.17 Resistance traces and corresponding SEM images for selected DUTs tested to a 50% resistance increase.

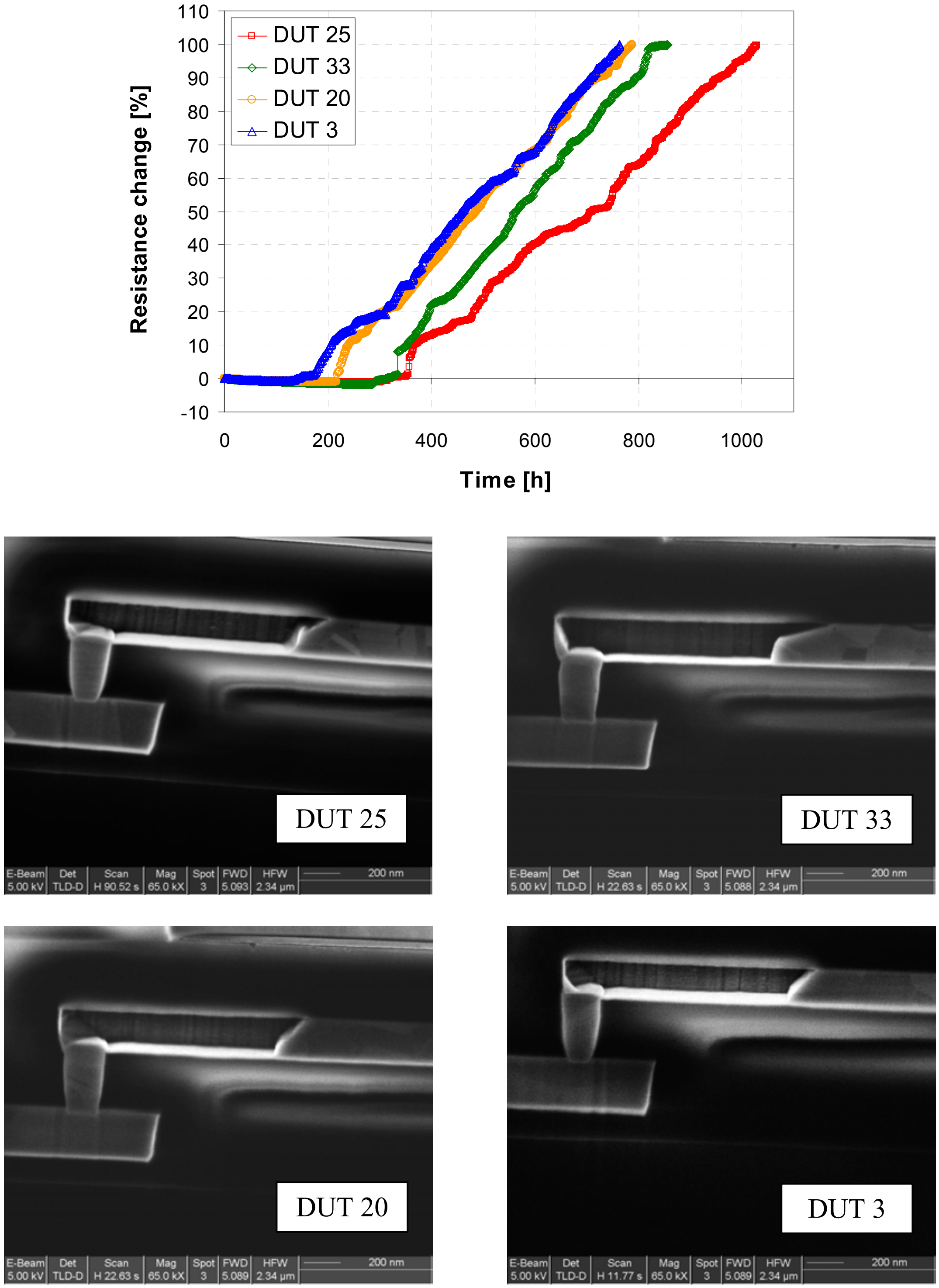

Figure 4.18 Resistance traces and corresponding SEM images for selected DUTs tested to a 100% resistance increase.

As seen in the figures, the void sizes increase with increasing failure criterion. Furthermore, at the same failure criterion, the void sizes are not identical. Void size distributions for all resistance-based EM experiments are included in Figure 4.19. All distributions can be well fit by a lognormal distribution function, even though the number of data points is too small to allow a definite statement about the most appropriate distribution function. The increase in median void area with failure criterion is obvious. However, in order to better examine the sigma values, sigmas of void size distributions as well as of EM lifetimes are plotted as a function of time in Figure 4.20. Again, the time is defined as the median lifetime of the experiment for the EM data as well as the resistance-based void sizes. The line fit used for the resistance-based void size statistics is based on Equation (4.1). In this case, parameters a and c have been set to 0.085 and 1. Again, the choice of these parameters will be examined further below. As mentioned previously, the sigma values of EM lifetime distributions decrease as a function of median lifetime. Likewise, the sigma values of the resistance-based void size distributions appear to decrease with increasing test time. However, the sigma values of resistance-based void size distributions are significantly smaller compared to the corresponding lifetime values at the same failure criterion. This observation indicates that even though the trend of sigma values over time is identical, the variation in void sizes cannot be the only factor inducing the sigma values in EM lifetime distributions. Additional parameters need to be considered when analyzing the higher sigma values of EM lifetimes.

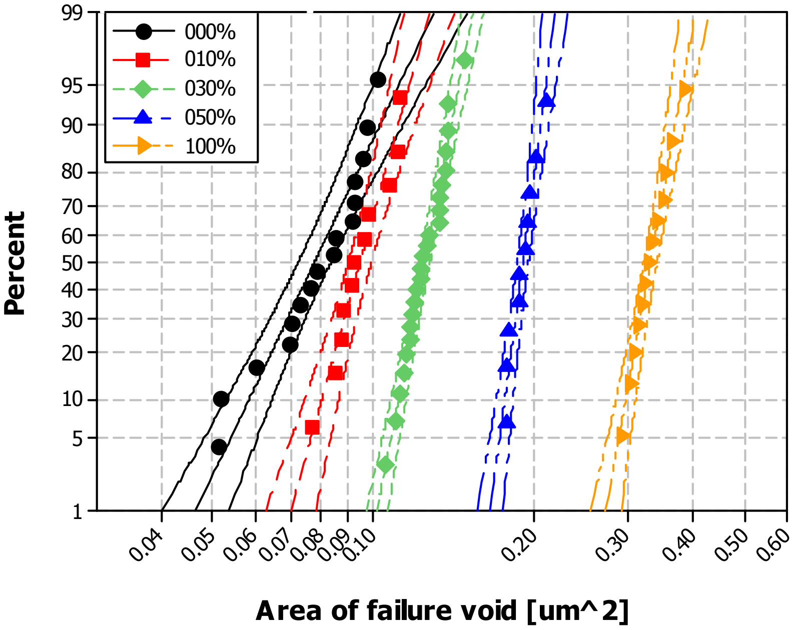

Figure 4.19 Void area distributions of resistance-based EM experiments. The void area distribution labeled ‘000%’ corresponds to a first resistance increase.

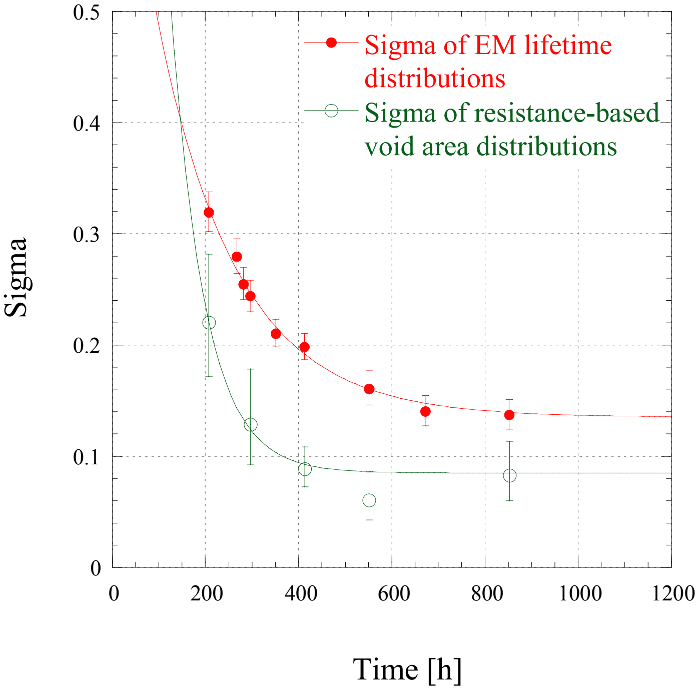

Figure 4.20 Sigma as a function of time for EM lifetimes and resistance-based void size distributions.

4.5 VOID SIZE ANALYSIS AS A FUNCTION OF TIME

Similar to the resistance-based EM tests, the size of at least 10 void areas has been obtained for each time-based EM experiment. Representative SEM images of voided interconnects together with corresponding resistance traces are shown in Figures 4.21-4.28 for various test times. 8 voids each are shown for 18.75h, 37.5 and 150h test times in Figures 4.21 to 4.26. Figures 4.27 and 4.28 display 4 voids each for 300h and 1000h experiments. Akin to the resistance-based EM tests, a larger number of voids are included for the shorter test times to illustrate the larger variety of possible void shapes and locations.

Again, similar to the resistance-based data, it needs to be mentioned that the void size analysis was performed on samples from different lots. The void data from 18.75h, 150h and 1000h EM tests was obtained using lot D62429.1, while the data corresponding to 37.5h and 300h experiments originated from lot D62375.1. As mentioned previously, a direct comparison of void data obtained from different lots is possible, since the EM behavior of all lots was found to be similar. Slight variations in line dimensions as a function of lot have been considered in the simulation part of this study as will be discussed in Chapter 5.

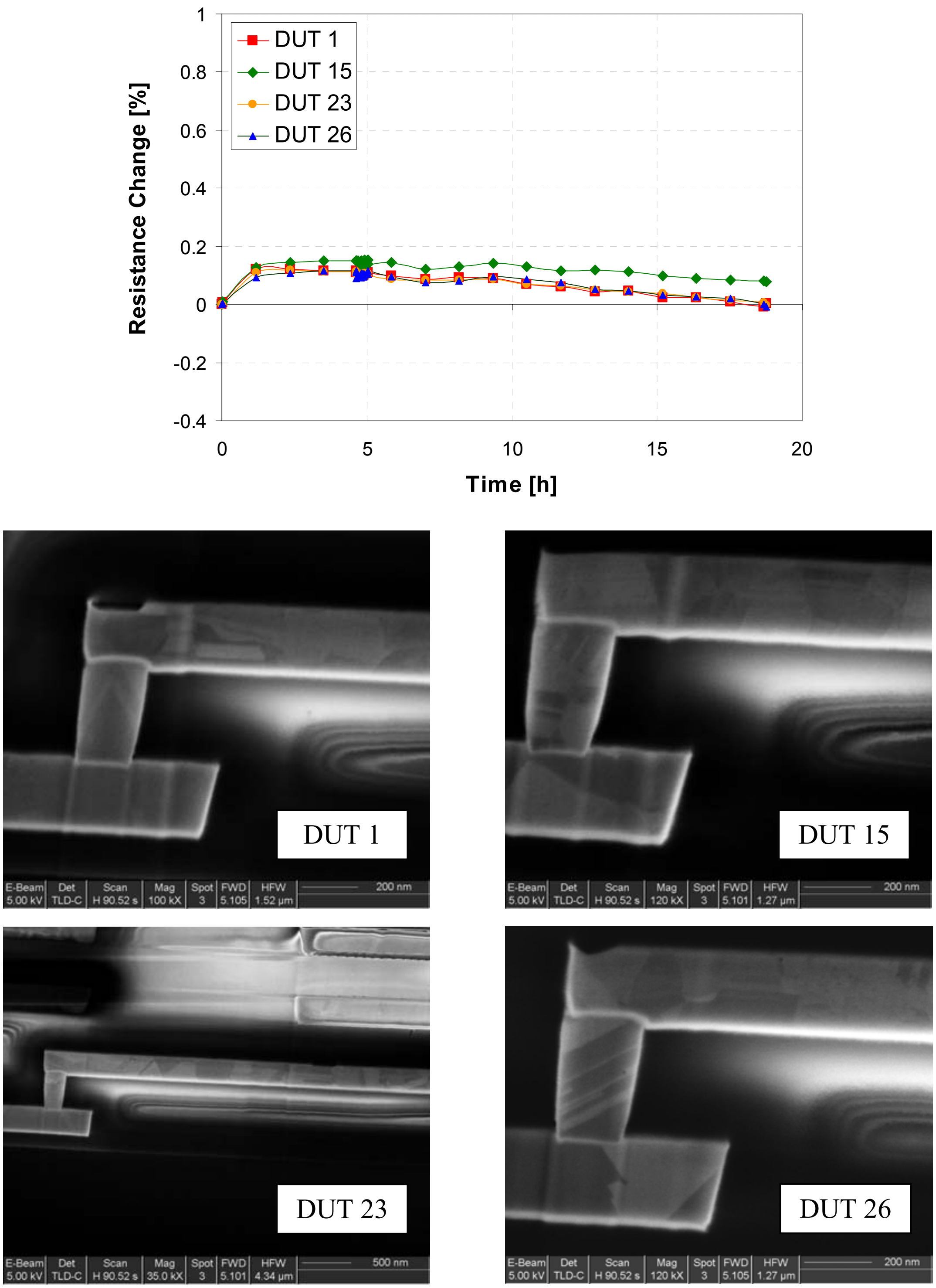

Figure 4.21 The resistance change as a function of time for selected DUTs tested for 18.75h, and corresponding SEM images showing the voids at the top interface of the interconnects.

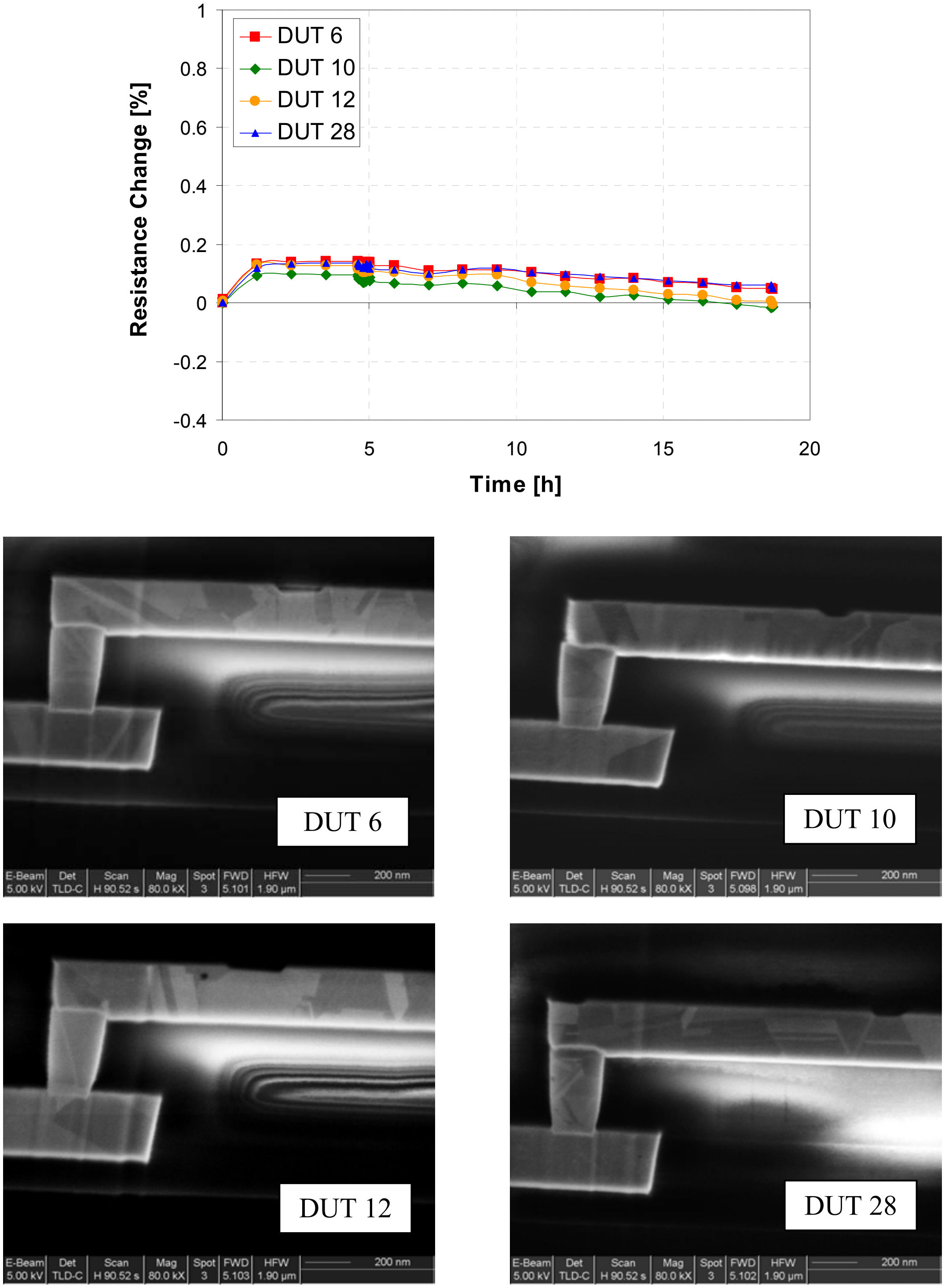

Figure 4.22 Additional results for samples tested for 18.75h. A larger number of resistance traces and corresponding SEM images are shown due to larger variations in void shape and location at short test times.

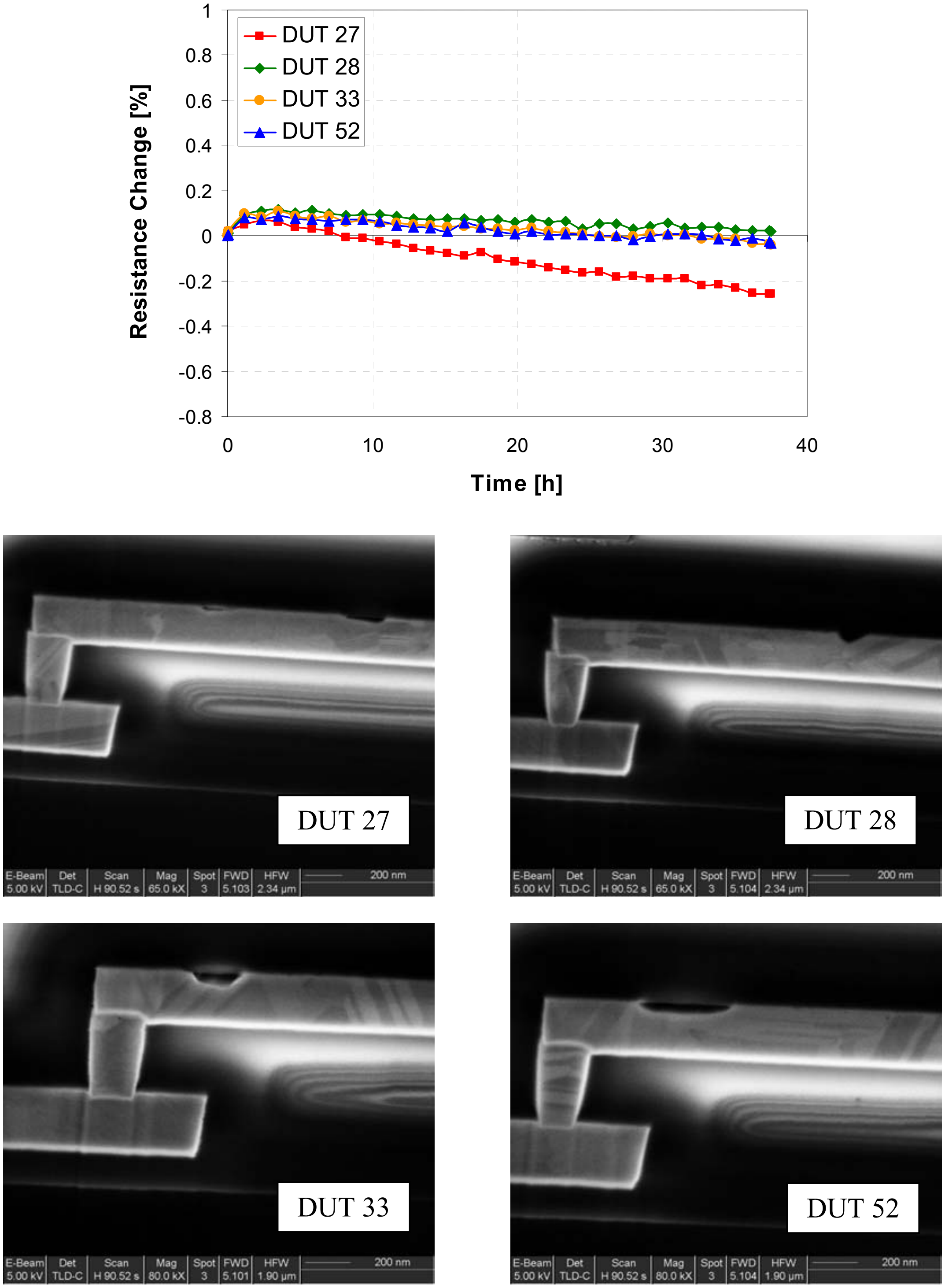

Figure 4.23 The resistance change as a function of time for selected DUTs tested for 37.5h, and corresponding SEM images showing the voids at the top interface of the interconnects.

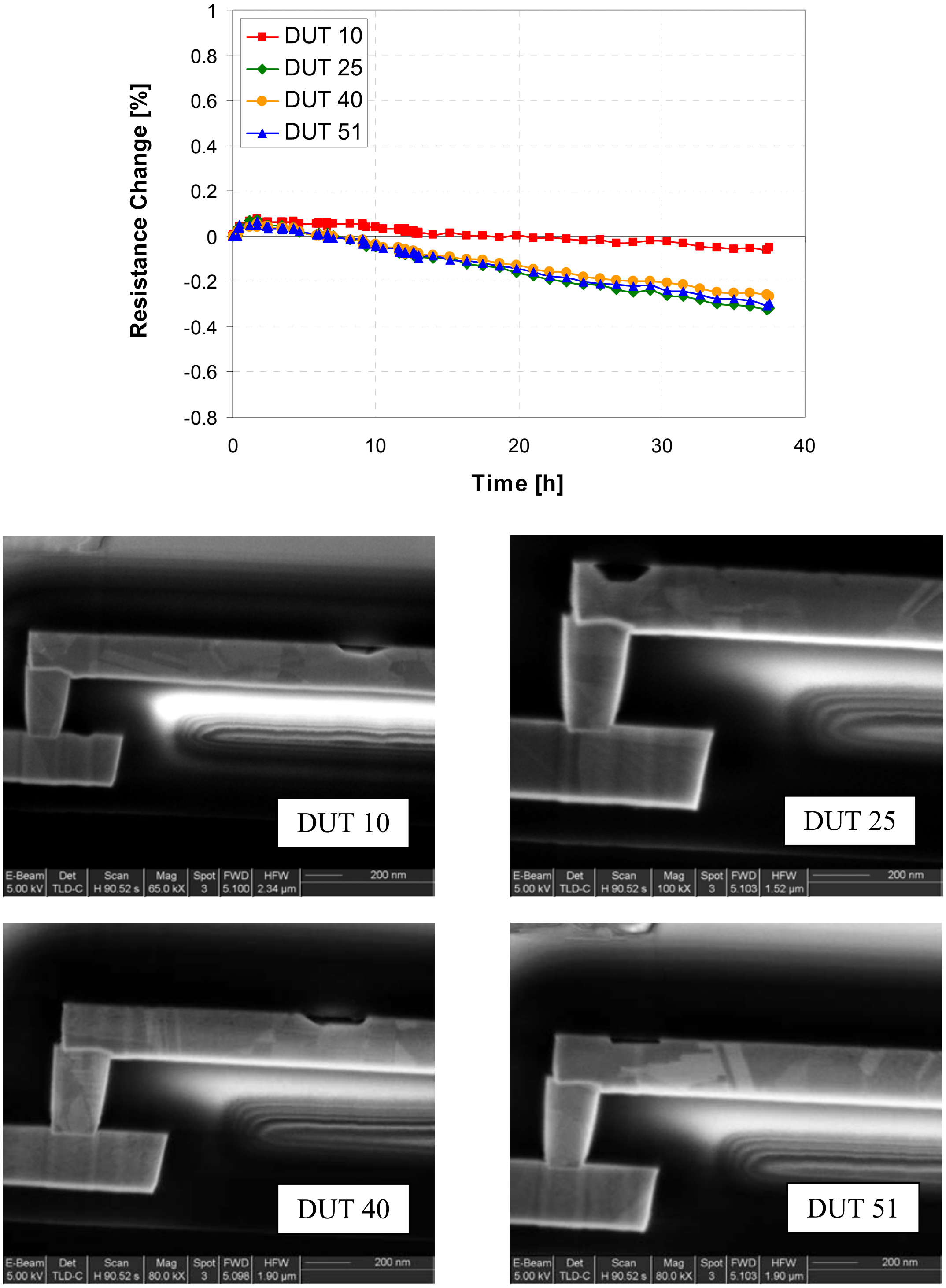

Figure 4.24 Additional results for samples tested for 37.5h. A larger number of resistance traces and corresponding SEM images are shown due to larger variations in void shape and location at short test times.

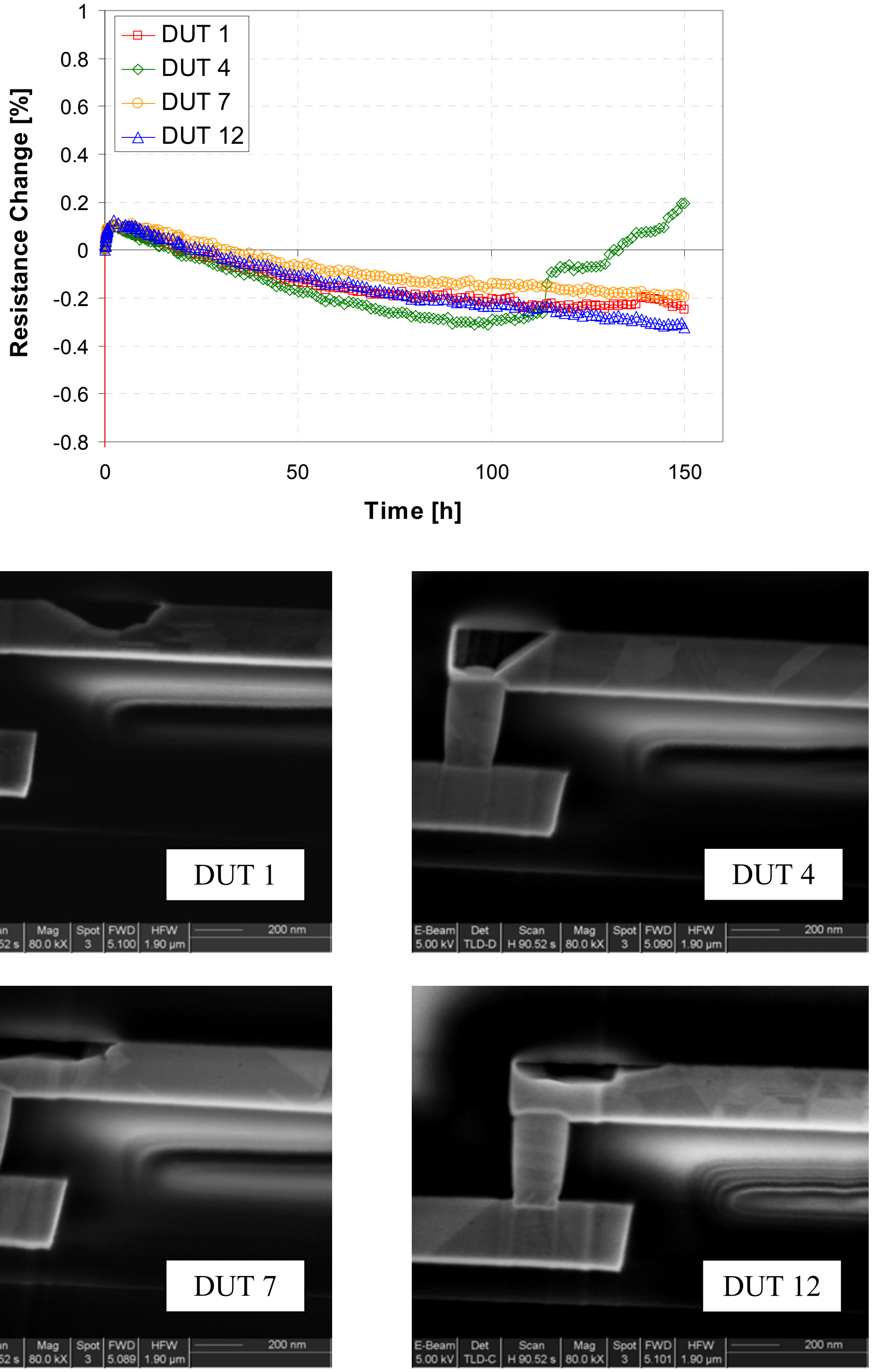

Figure 4.25 Resistance traces and corresponding SEM images for selected DUTs tested for 150h.

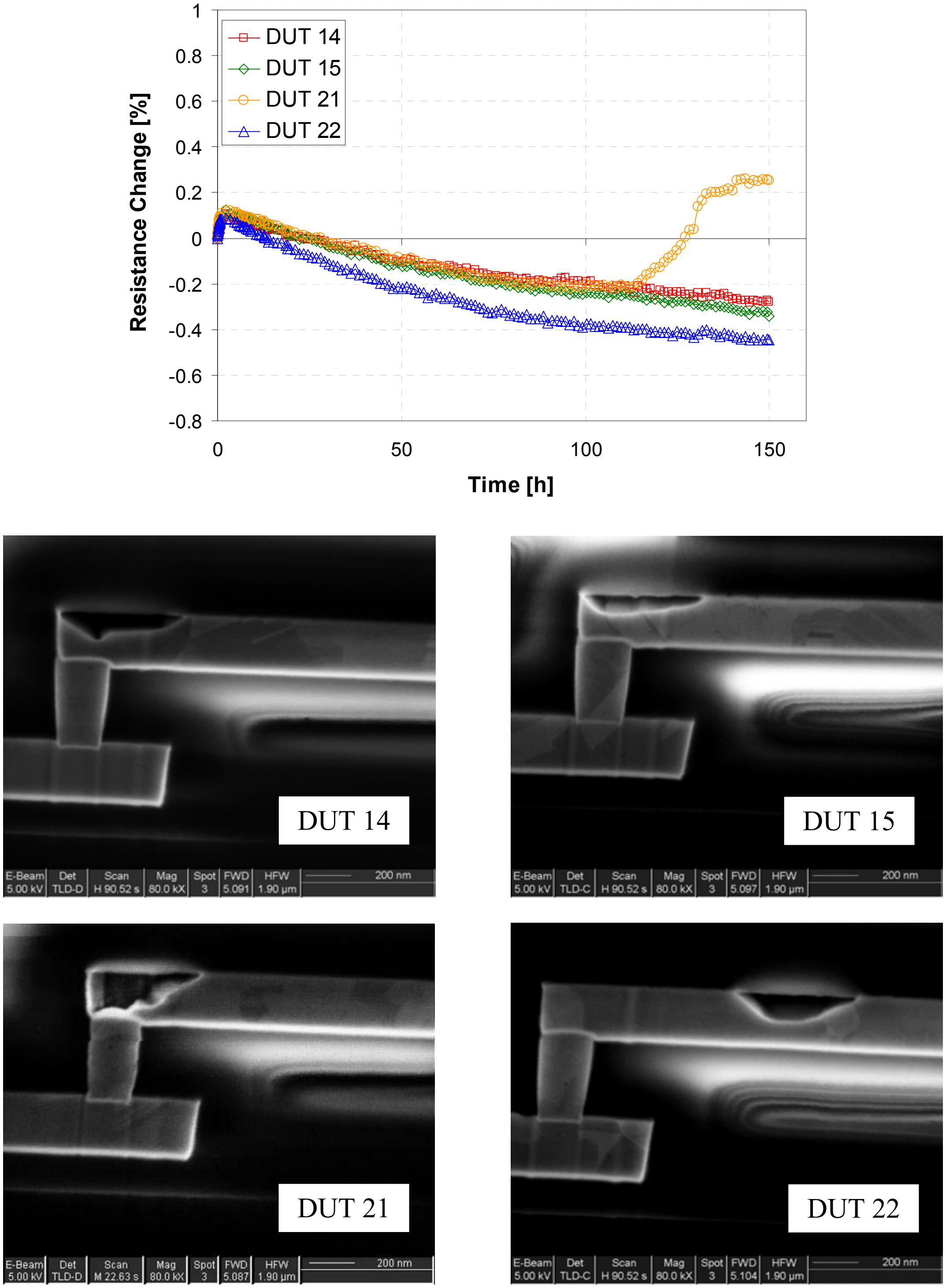

Figure 4.26 Additional results for samples tested for 150h. A larger number of resistance traces and corresponding SEM images are shown due to larger variations in void shape and location at short test times.

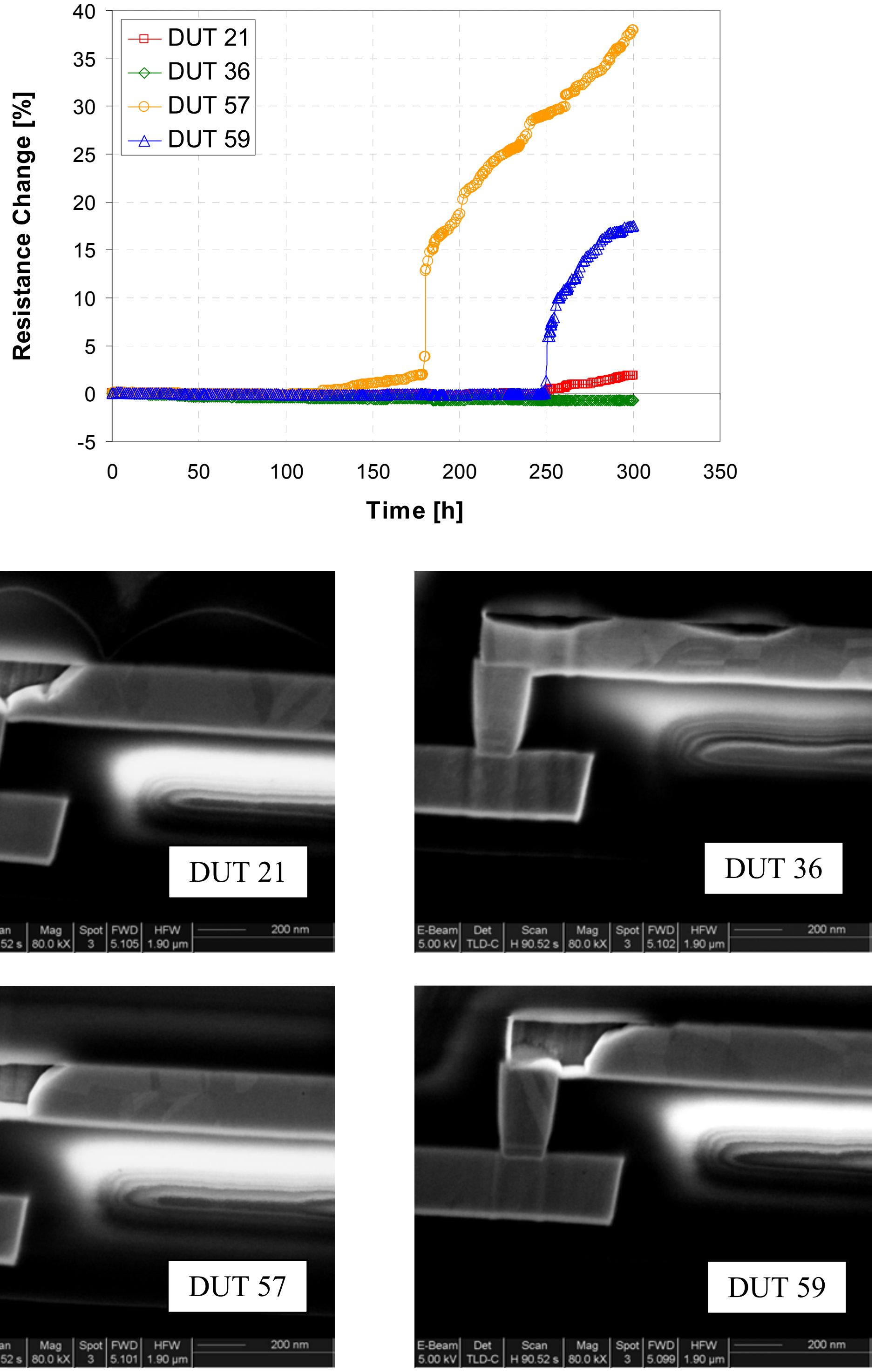

Figure 4.27 Resistance traces and corresponding SEM images for selected DUTs tested for 300h.

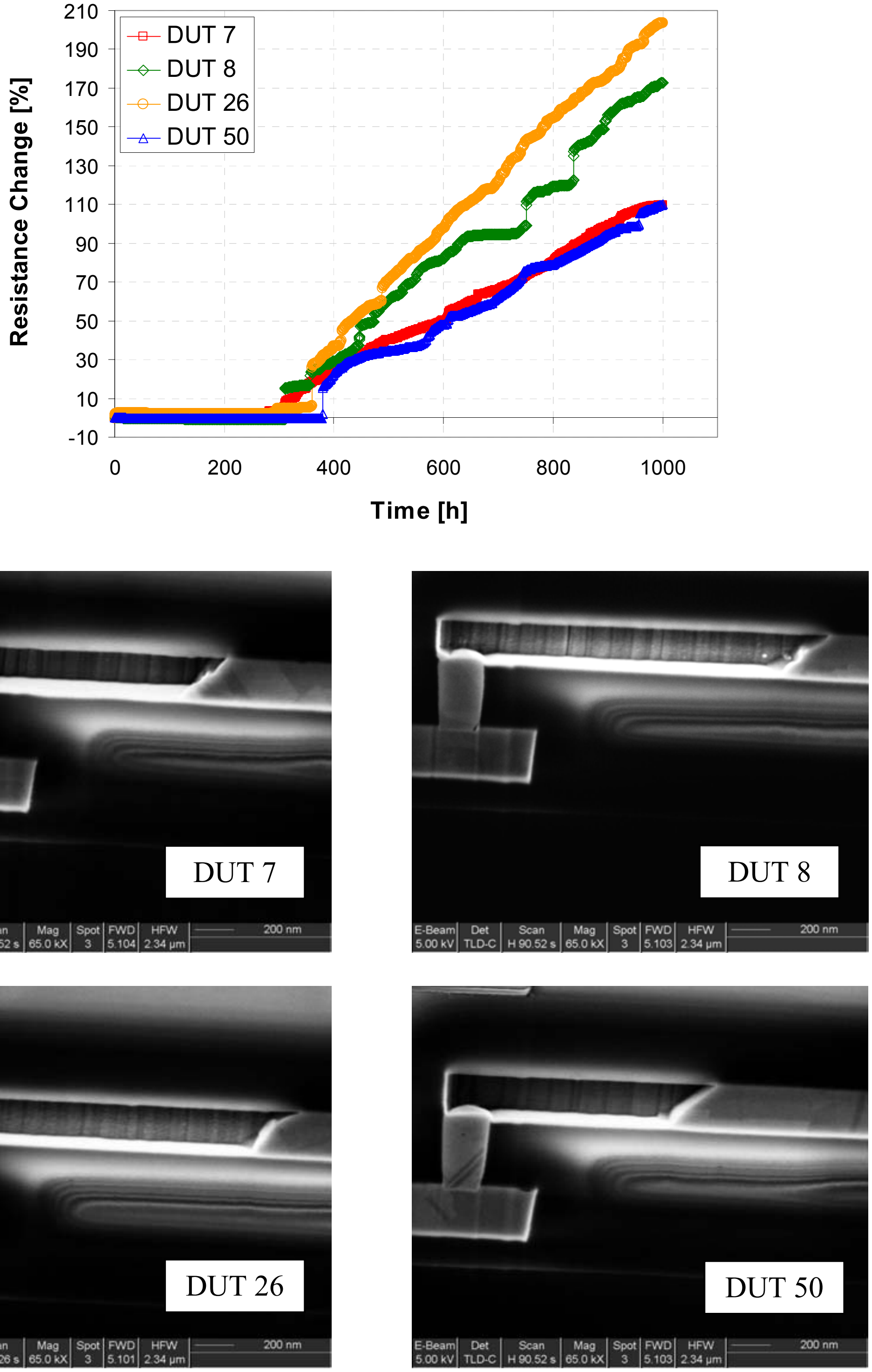

Figure 4.28 Resistance traces and corresponding SEM images for selected DUTs tested for 1000h.

Again, the pictures indicate that the void sizes increase with increasing test time. Additionally, after the same test time, the void sizes are not identical. For small times, they are not even at the same location, but randomly distributed at the interface. For longer times, all voids reach stage 4 of void evolution, i.e. they are at the cathode end growing along the line.

A difference in the definition of void area for the time-based and the resistance-based experiments needs to be mentioned. During all stages of void evolution, there can be more than one void per line depending on the amount of significant flux divergence sites. Even in stages 3 and 4, in addition to the main void at the cathode end, there can be other voids at the top interface similar in appearance to the voids in stage 1. The number, size and location of these voids is defined by the local microstructure as in stage 1. In resistance-based tests, only the void at the cathode end contributes to the observed resistance increase, whereas additional voids do not have a significant influence. Thus, for these tests the void area is considered to be only the area of the final failure void. In contrast, in time-based tests, the total amount of Cu being displaced in a fixed test time is being measured. Hence, the sum of the areas of all voids within 20-30μm from the cathode end is taken as the void area. This distinction is not significant when considering resistance increases above 10% or large test times, since the area of the major void at the cathode end dominates the total void size. However, when analyzing short test times, the difference between counting all observed voids or just the one at the cathode end becomes significant. Especially during void evolution stages 1 and 2, it is impossible to identify a major void in the first place.

Another detail about the void size acquisition needs to be mentioned. As seen in the images, the voids in the first two stages of void evolution are quite small. Hence, it is questionable whether they span the entire line width. In order to account for any variation in void area across the line, SEM images were taken at least twice at different positions within the line. Usually, the lines were cut approximately in the middle of the line and another time further to the end of the trench. For some lines, another imaging step was performed at the beginning of the line. Figure 4.29 shows SEM images of the same line approximately at the beginning, in the middle and towards the end of the trench. This line had been EM tested for only 37.5h. Changes in void shape can be seen. The void appears to be longer, but shallower towards the end of the interconnect. However, it seems to be spanning the entire line even after the very short test time. It is clear that small voids can exist which do not cover the complete line width, however, the biggest voids, which dominate the void area measurement, appear to be spanning the line width already after short test times. The void area used in the following represents the average of all measured void sizes per void for each line. This method has been used for samples tested for 18.75h and 37.5h as well as selected additional samples.

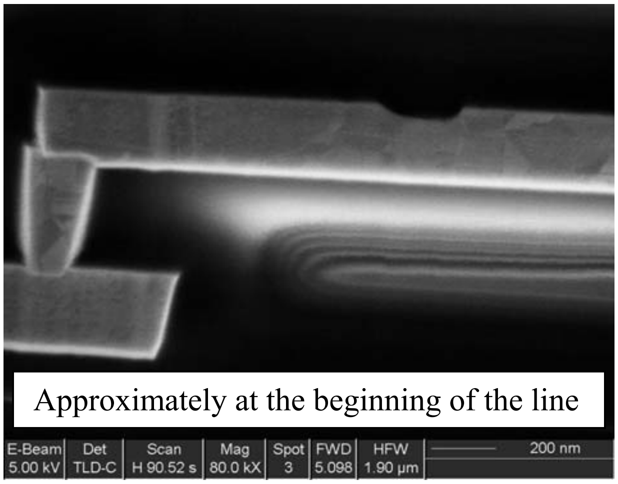

Approximately at the beginning of the line

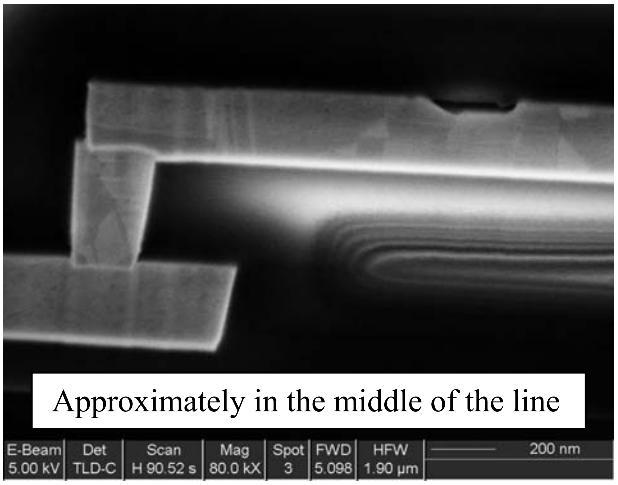

Approximately in the middle of the line

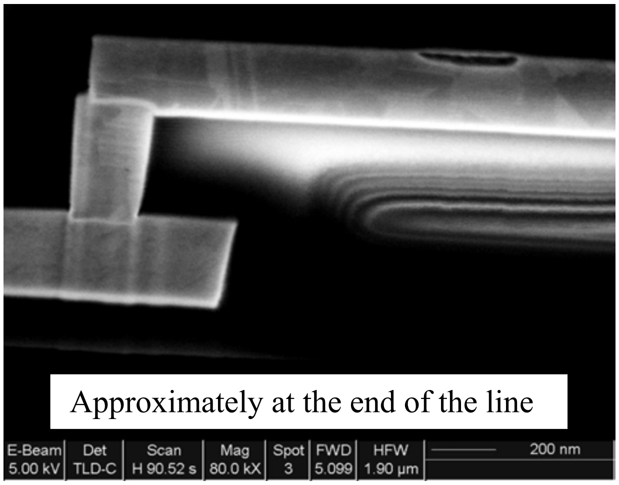

Approximately at the end of the line

Figure 4.29 SEM images of an interconnect tested for 37.5h showing the line approximately at the beginning, in the middle and towards the end.

Void size distributions for time-based EM experiments are included in Figure 4.30. Akin to the resistance-based void size distribution, a lognormal distribution function has been used to fit the data. Again, the increase in median void area with time is obvious. Figure 4.31 shows the evolution of sigma for both types of void size distributions as well as for EM lifetimes as a function of time. For the line fit of the time-based void size statistics, parameters *a* and *c* in Equation (4.1) have been set to 0.105 and 0.44. The sigma values of the time-based void size distributions decrease with increasing test time. Hence, the trend in the evolution of sigma over time is similar for both types of void sizes as well as EM lifetime distributions. Mostly, the sigma values of time-based void size distributions are significantly larger compared to the corresponding values of resistance-based voids. Only at the first resistance increase, the values are comparable. The observed differences between sigma values of both types of void size distributions and the correlation to the EM lifetime statistics will be discussed in detail in Chapter 5.

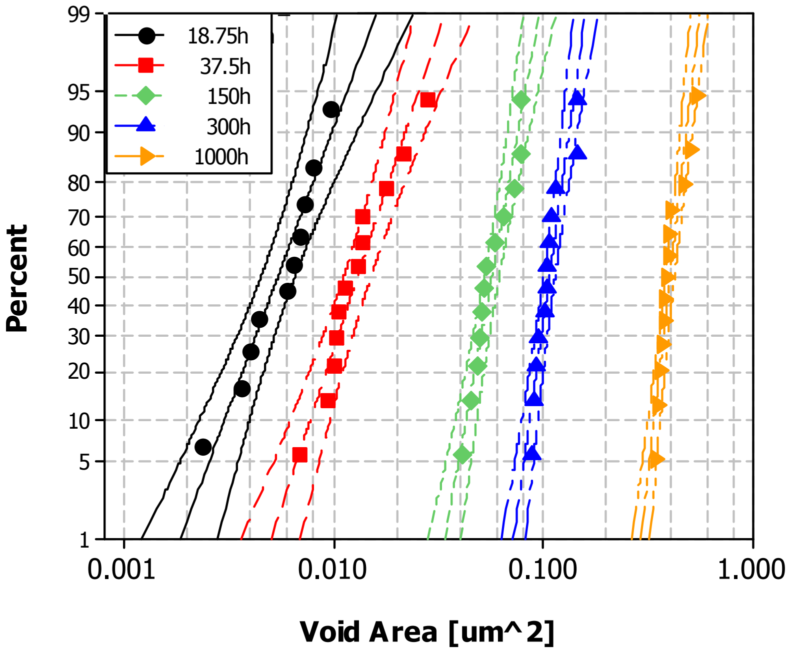

Figure 4.30 Void area distributions of time-based EM experiments.

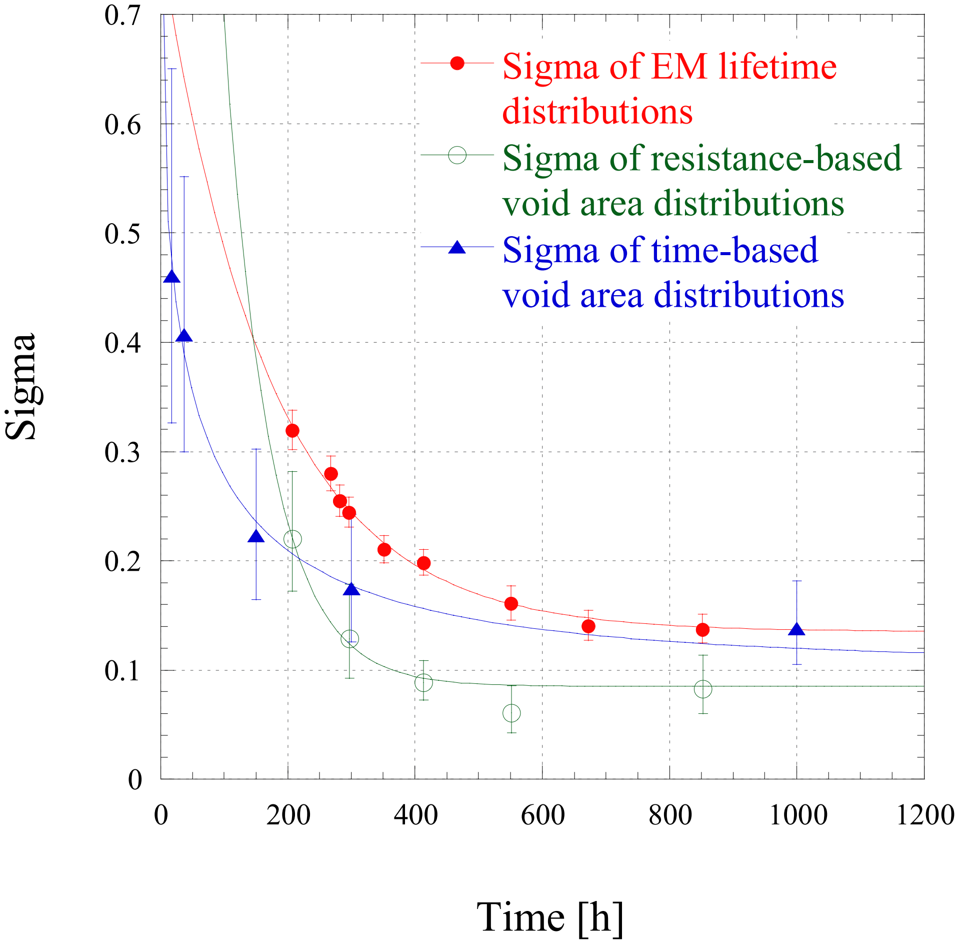

Figure 4.31 Sigma as a function of time for EM lifetimes and resistance-based and time-based void size distributions.

4.6 AVERAGE VOID GROWTH AS A FUNCTION OF TIME

Void areas as a function of void formation time are plotted in Figure 4.32 separated by experimental condition. In this case, akin to the data from time-based experiments, the data points from resistance-based EM tests are the sum of all observed void areas for each line. This is in contrast to the void size distributions shown above, since in this case each individual void formation time has been used and not the median lifetime based on a particular resistance increase. Data points for the median void areas for each experiment are shown in Figure 4.33. It can be seen that the average void area increases linearly with time. A linear fit through these data points passes through zero indicating that void formation begins directly after the current flow has started. Hence, an incubation time similar to the one observed for Al(Cu) EM is not seen in Cu interconnects. This is expected, since Cu diffusion begins immediately with the onset of current flow. In contrast, in Al(Cu) technology, initially Cu diffuses to clear a critical distance. Only subsequently, Al movement and thus void formation begins. Hence, an incubation time is usually observed [Rosenberg 1972, Hu 1993c, Hu 1994]. Besides the linear behavior of the average void areas with time, it can be seen that variations in void sizes exist within each experiment as already discussed above. For time-based experiments, only variations in void size exist, since the time is fixed, while for resistance-based tests, variations occur in both time and void areas with the latter being significantly smaller. This observation indicates that one of the assumptions made by He *et al.* [2004] is not supported by this study. They assume a deterministic correlation between void sizes and lifetimes. However, as seen in the experimental data above, that correlation appears to be more complicated, requiring a more detailed analysis of the statistics of the void evolution process.

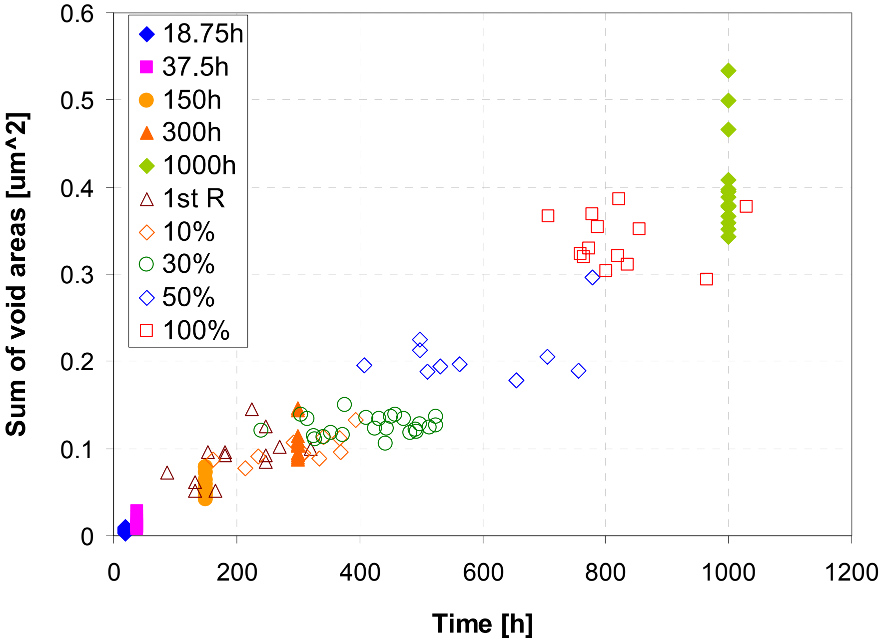

Figure 4.32 Void areas as a function of time. The void area is taken as the sum of all void areas observed per line.

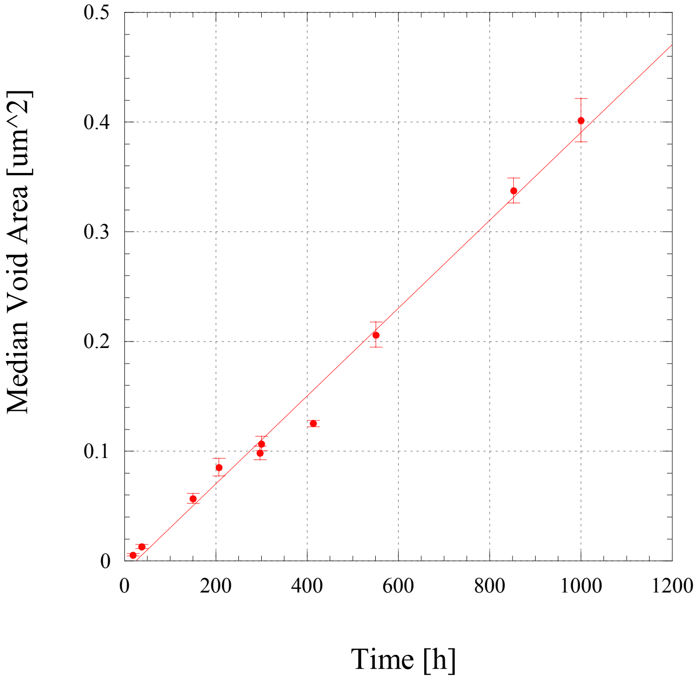

Figure 4.33 Median void areas for each experiment as a function of median test time together with a linear fit.

Figure 4.34 displays the individual void areas as a function of resistance change. Since only the major voids contribute to the resistance change, only their areas are included in this chart. The median void areas as a function of median resistance increase are included in Figure 4.35. Again, variations within each experiment can be observed, while the average void areas increase approximately linearly as a function of the resistance increase. Deviations from linearity can be observed at low percentage values with median void areas slightly larger than expected. This phenomenon can be explained when considering the SEM images corresponding to EM tests conducted to the first resistance increase (Figures 4.11-4.13). It is obvious that these voids can have different sizes due to their larger variety in shape and location. Only in a few cases the Cu has been removed entirely from the cathode end. Most voids appear as extended interface voids just approaching the line end. Once they reach the interconnect edge, the more controlled void growth of stage 4 leads to better defined void sizes. The linear fit through the average values in Figure 4.35 results in an average void area of $0.061\mu m^2$ needed to obtain the first resistance increase. This is smaller than the measured value of $0.078\mu m^2$ as explained above.

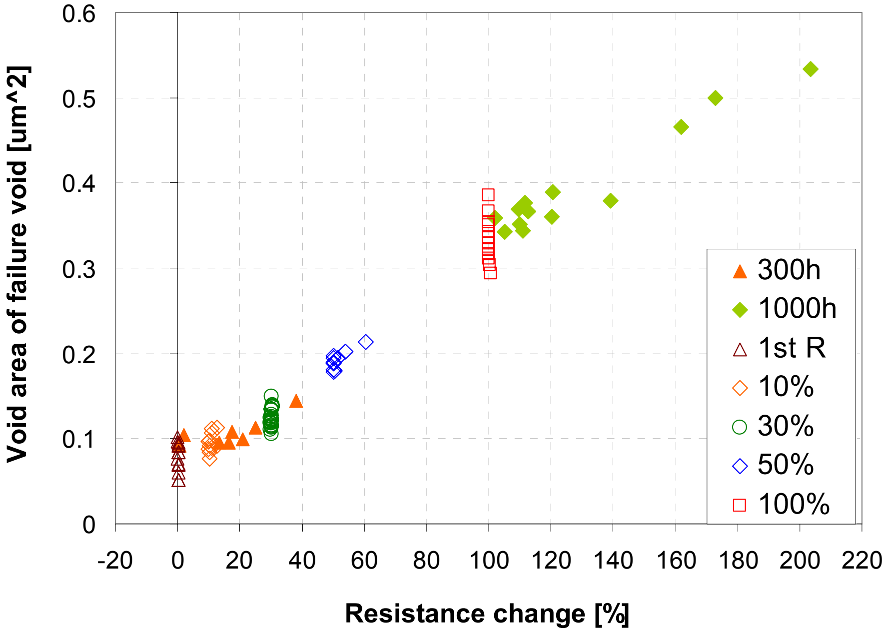

Figure 4.34 The void area of each failure void as a function of the corresponding resistance increase.

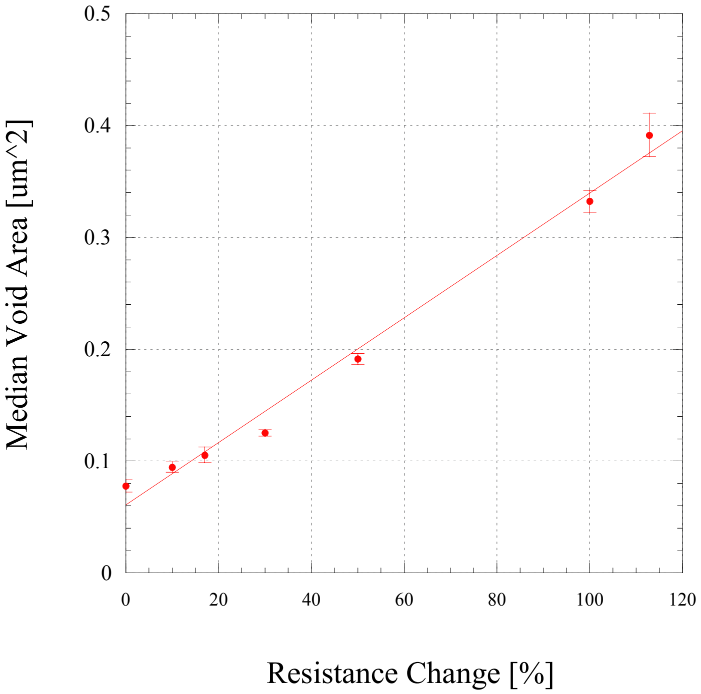

Figure 4.35 Median void areas for each experiment as a function of median resistance increase together with a linear fit.

The void length on top of each failure void is displayed as a function of corresponding resistance change in Figure 4.36. Here again, only voids are included which already span the whole line and create a significant resistance increase. It can be seen that for small resistance increases, the void length on top of the void shows considerable statistical scatter. While the voids are evolving towards the via in stages 1 and 2, they sometimes are very long, but shallow as can be seen in the SEM images corresponding to the first resistance increase and before. Once they span the whole line and develop according to stage 4, the growth is more controlled reducing the variation in void extension. In that stage, similar to the void area, the average void length on top of the void increases linearly in time.

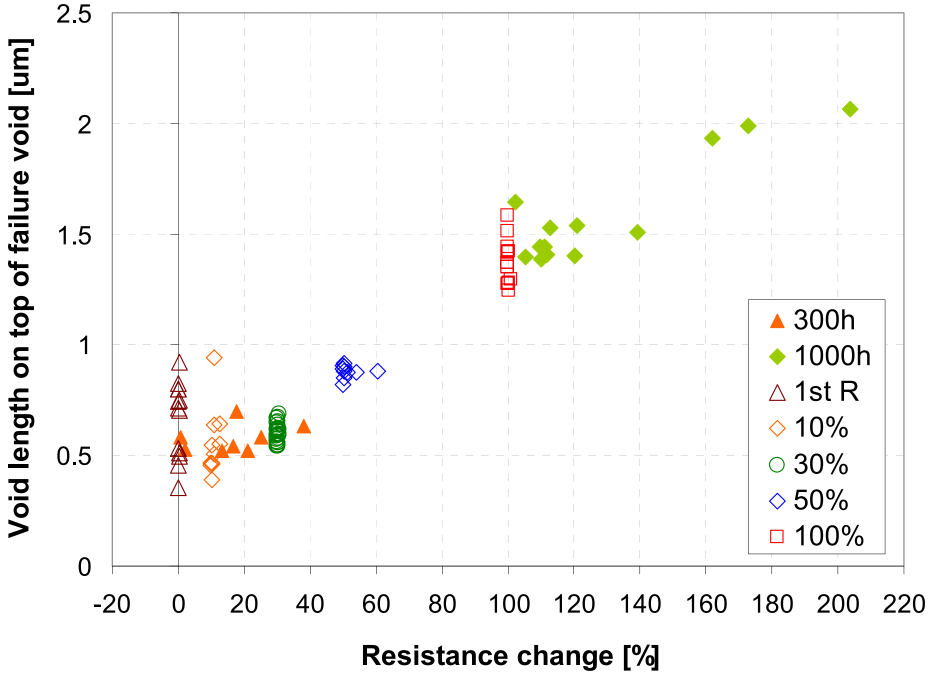

Figure 4.36 The void length on top of each failure void as a function of the corresponding resistance increase.

The void length adjacent to the via on the bottom of the trench as a function of time is plotted in Figure 4.37. Obviously, for this plot, only voids have been considered which have passed the via. This excludes the first resistance increase data, which as seen in the images above, does not fulfill this criterion. The average values as a function of average void formation time are included in Figure 4.38. Similar to the other void measurements, the average void length adjacent to the via increases linearly with test time, while each experiment in itself shows variations. A linear fit through the data passes the time axis at approximately 235h. This is slightly larger than the median time for the first resistance increase (207h), since a first resistance increase can be observed already before the void reaches the end of the via, but significantly reduces the Cu cross-sectional area. Extrapolation of the linear fit to the start of the experiment shows a negative length value of 0.35µm. This value is representative of the void length which would have formed in 235h if the void were in stage 4 of void evolution. It includes the length of the via, which is approximately 0.21µm. However, the fact that it is significantly larger than the via length indicates that the void needs some time to develop at the top interface and to grow down to the bottom of the line.

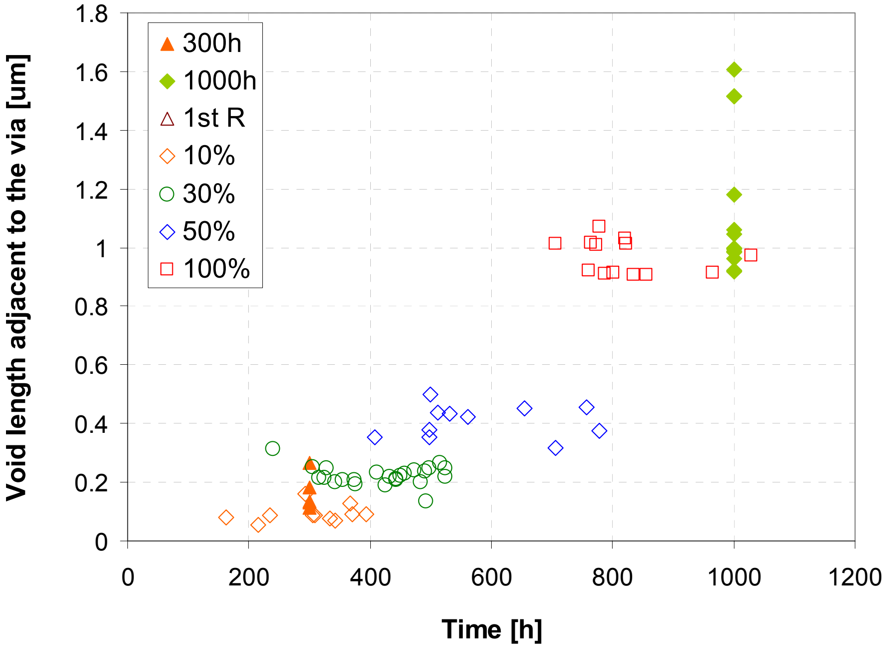

Figure 4.37 Void length adjacent to the via as a function of time.

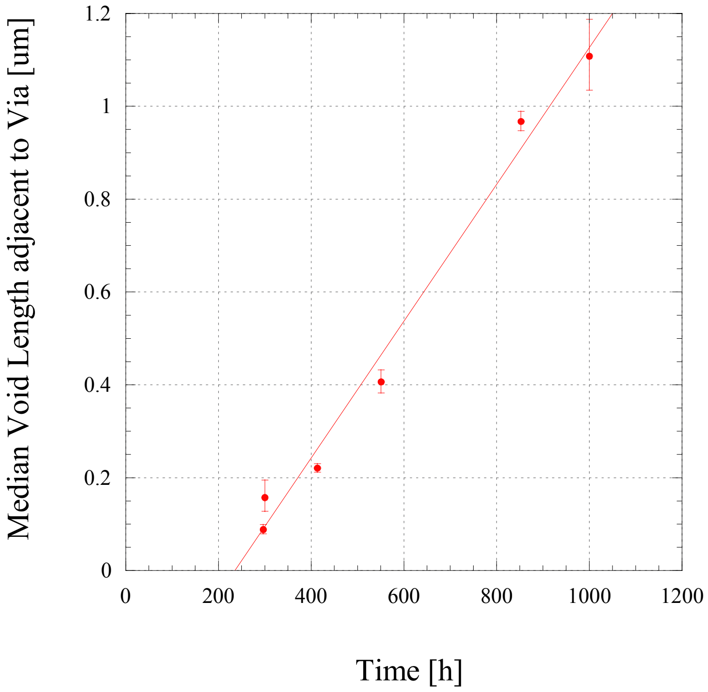

Figure 4.38 Median void length adjacent to the via for each experiment as a function of median test time together with a linear fit.

Figure 4.39 shows the void length adjacent to the via as a function of the corresponding resistance change. Comparing all shown scatter charts, the deviations from linearity are smallest in this plot. The reason for this observation is the fact that a given resistance increase defines the void length adjacent to the via to a high degree. This will be explained in detail in Section 5.3. Furthermore, this plot indicates that in order to observe a significant resistance increase the void has to cover the entire via and needs to start extending past it. Already small resistance increase values of about 1%-5% appear to require the current to pass through the Ta barrier layer, i.e. the void needs to extend past the via. As seen in the resistance traces of the first resistance increase voids, none of them have reached even 1% of change yet. Correspondingly, the voids are not necessarily covering the via, but create a resistance increase by significantly reducing the Cu cross-sectional area. For further analysis, void area distributions of samples tested to a 1% or 2% resistance change are needed.

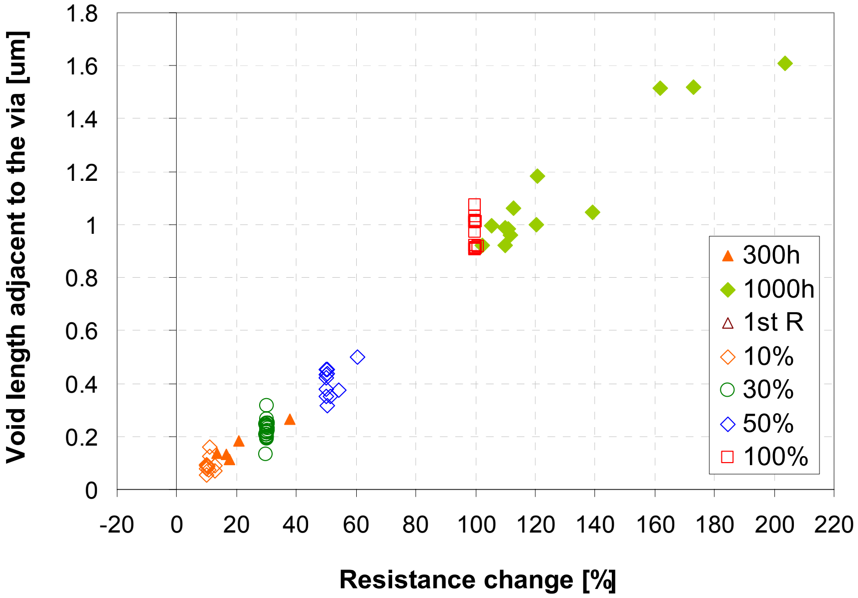

Figure 4.39 The void length adjacent to the via of each failure void as a function of the corresponding resistance increase.

Chapter 5: Discussion and Analysis of EM Statistics

The experimental results in Chapter 4 showed that the variation in EM lifetimes decreases with increasing failure criterion. While the sigma values of resistance-based void size distributions display a similar trend, their values are significantly smaller indicating that they can be the underlying distribution of EM lifetime sigmas defining the trend, but additional parameters need to be considered when examining the absolute values. Void size distributions from time-based EM experiments again showed the decrease in sigma with increasing test time, however their values are larger compared to the resistance-based void sizes. This chapter contains the discussion of the experimental results including simulation results used to explain the observed statistics of void sizes and EM lifetimes. A geometrical and a kinetic model have been formulated to explain the void size characteristics. Furthermore, a correlation between the EM experiments and both types of void size measurements will be shown.

5.1 MASS TRANSPORT EQUATIONS

As already introduced in Chapter 2, the EM induced mass flux through an interconnect can be described as a product of drift velocity v_d and atomic density N. For long Cu interconnects capped with a layer which allows significant interface diffusion, such as SiN_x, the drift velocity of the moving Cu ions under the EM driving force is given by Equation (2.10). Thus, the EM mass flux can be written as

$$J = Nv_d = N \frac{\delta_i}{h} \frac{D_i}{kT} Z_i^* e\rho j \tag{5.1}$$

Additionally, the mass flux through an interconnect line can be described by

$$J = \frac{N_{Cu}}{A_{Cu}\Delta t} \tag{5.2}$$

where N_{Cu} is the number of Cu ions moving through the Cu cross-sectional area A_{Cu} in time Δt. The Cu ions move in the direction away from the cathode end towards the anode end of the line leaving behind a void. Hence, the number of participating Cu ions can be described by

$$N_{Cu} = \frac{\Delta V_{Void}}{\Omega} \tag{5.3}$$

where ΔV_{Void} is the change in void volume created by the EM mass flux and Ω the atomic volume. Hence,

$$J = \frac{\Delta V_{Void}}{\Omega A_{Cu}\Delta t} \tag{5.4}$$

Combining Equations (5.1) and (5.4) yields

$$N\frac{\delta_i}{h}\frac{D_i}{kT}Z_i^* e\rho j = \frac{\Delta V_{Void}}{\Omega A_{Cu}\Delta t} \tag{5.5}$$

Since N is equal to the inverse of Ω, this equation simplifies to

$$\frac{\delta_i}{h}\frac{D_i}{kT}Z_i^* e\rho j = \frac{\Delta V_{Void}}{A_{Cu}\Delta t} \tag{5.6}$$

Most of the voids span the whole line already after a few hours of EM testing as discussed in Chapter 4. Thus, the change in void volume over time Δt can be approximated to:

$$\Delta V_{Void} = \Delta A_{Void} w \tag{5.7}$$

where ΔA_{Void} is the change in the void area as measured in cross-sectional analysis. It needs to be remembered that the void area is measured parallel to the electron flow, whereas the cross-sectional area A_{Cu} is defined perpendicular to the electron flow. Substituting Equation (5.7) into Equation (5.6) and rearranging yields an equation for time Δt:

$$\Delta t = \frac{hkT}{D_i Z_i^* e\rho j \delta_i} \frac{\Delta A_{Void} w}{A_{Cu}} \tag{5.8}$$

Replacement of current density j with the quotient of current I and cross-sectional area A_{Cu} and further rearrangement lead to:

$$\Delta t = \frac{kTA_{Cu}}{D_i Z_i^* e\rho I \delta_i} \frac{\Delta A_{Void} hw}{A_{Cu}} = \frac{kTA_{Cu}}{D_i Z_i^* e\rho I \delta_i} \Delta A_{Void} \tag{5.9}$$

This equation allows the calculation of the time required to increase the void size by a certain amount. Hence, it can be used to estimate the EM lifetime needed to create a void and enlarge it to its final size. More importantly for this study, this equation indicates all parameters needed to analyze the statistics of the EM lifetime distribution. It is obvious that some of the variables in Equation (5.9) have statistical variations, i.e. they are not constant. The combination of all these variations is responsible for the variation in EM lifetimes. Obvious constants in Equation (5.9) are Boltzmann's constant and the electric charge. Furthermore, certain interface properties, such as the interface width and the effective charge number, can be assumed to be constant. Slight variations in Cu resistivity between lines could be induced by variations in the electroplating process possibly leading to slightly different amounts of additives in the Cu. However, these are expected to be rather small and have been neglected here. Likewise, the variation in applied current between lines has been ignored, since the current control is very stable as mentioned in Chapter 3. All constants can be combined into one term, simplifying Equation (5.9) to

$$\Delta t = C \frac{\Delta A_{Void} T A_{Cu}}{D_i} \tag{5.10}$$

where

$$C = \frac{k}{Z_i^* e \rho I \delta_i} \tag{5.11}$$

When analyzing the total time *t* during which the interconnect was subjected to current flow, the change in void area can be replaced by the total void area A_{Void}. Therefore Equation (5.10) can be adjusted to:

$$t = C \frac{A_{Void} T A_{Cu}}{D_i} \tag{5.12}$$

It can be seen from Equation (5.12) that the lifetime distribution is a function of the void area distribution, the temperature variation in the EM oven, the Cu cross-sectional area distribution and the variation in diffusivity from line to line. The variation in diffusivity could arise from a variety of reasons including the influence of Cu grain orientation, processing issues and EM test temperature. Most of these will be analyzed in more detail later, while the influence of temperature can be included here. As shown in Chapter 3, the temperature varies somewhat across the EM oven, thus exposing certain lines to slightly higher or lower temperatures compared to other interconnects. The influence on the diffusivity can be expressed as:

$$D_i = D_i^0 \exp(-\frac{Q_i}{kT}) \tag{5.13}$$

where D_i^0 is the prefactor of the diffusivity term and Q_i the activation energy. Substituting Equation (5.13) into (5.12) results in

$$t = C\frac{A_{Void} T A_{Cu}}{D_i^0 \exp(-\frac{Q_i}{kT})} \tag{5.14}$$

Equation (5.14) provides the basic mathematical formula used in this study to examine the statistics of both time-based void sizes and electromigration lifetime distributions.

5.2 CORRELATION BETWEEN TIME-BASED AND RESISTANCE-BASED TESTS

From Equation (5.14) it can be seen that the variation in void sizes contributes to the variations in EM lifetimes. However, since at least three additional parameters have an influence on the EM lifetime statistics, the experimental observation that the sigma values from EM lifetime distributions are larger than the sigma values of resistance-based void size distributions is intuitively understandable. The question arises whether it is possible to explain EM lifetime statistics from measured void sizes and these additional experimental parameters using Equation (5.14). The statistics of the void area, the temperature and the Cu cross-sectional area distributions were measured as discussed in previous chapters. However, the variation in interface diffusivity from line to line is not easily measurable. Variation in interface diffusivity can have several causes, including the influence of Cu grain orientation, processing issues and temperature. The effect of the latter has been included already. The other parameters will be discussed in detail in Chapter 5.4, where an attempt will be made to simulate the diffusivity variation. Here, the measured results from time-based experiments will be used to estimate the experimental and mass transport variations at certain times.

When performing time-based experiments, the left-hand side of Equation (5.14) is a constant value. Thus, Equation (5.14) can be rearranged to

$$A_{Void}^{t-based} = C^{*} \frac{D_i^0 \exp(-\frac{Q_i}{kT})}{TA_{Cu}} t_{test} \tag{5.15}$$

where C^* is equal to $1/C$ and $A_{Void}^{t-based}$ denotes the void area after a fixed test time. The parameter t_{test} represents the fixed time of each time-based EM experiment. This equation indicates that with the time being a constant, the statistics of the void areas equal the combined variations of the experiment, such as temperature variation, Cu cross-sectional area variation, and variation in mass transport, i.e. diffusivity differences between lines. Hence, with the measurement of the void area statistics at certain times, an experimental measurement of the diffusivity variation has been indirectly achieved, which otherwise is hard to obtain.

Now, when performing the time-based experiments with test times equal to the median times of the resistance-based EM experiments, the measurements of the time-based void area statistics provide a reasonable estimate of the experimental and mass transport variation influencing the lifetime distribution characteristics. Equating the test time with the median lifetime of the resistance-based EM experiments in Equation (5.15) and rearranging leads to

$$C \frac{TA_{Cu}}{D_i^0 \exp(-\frac{Q_i}{kT})} = \frac{t_{median}}{A_{Void}^{t-based}} \tag{5.16}$$

Now combining Equations (5.15) and (5.16) yields

$$t = \frac{A_{Void}}{A_{Void}^{t-based}} t_{median} \tag{5.17}$$

It needs to be mentioned that this equation is only an approximation, since the diffusivity variation depends on time as will be discussed in Chapter 5.4. Hence, equating the diffusivity variation observed during a time-based experiment conducted to the median time of a resistance-based experiment with the diffusivity variation of that resistance-based test is not entirely correct. However, the difference is expected to be rather small. In general, Equation (5.17) indicates that the variation in EM lifetimes can be calculated by combining the statistics of resistance-based and time-based void areas, both of which have been obtained experimentally. Although the chosen test times of the time-based experiments in this study are not identical with the median lifetimes of the resistance-based tests, the empirical fit to the time-based void data as shown in Figure 4.31 allows the extraction of the sigma value at any required time. Hence, for each resistance increase failure criterion, two random distributions with 500 data points each have been generated. For one of them, the measured sigma value of the resistance-based void areas has been used, and for the other the extrapolated sigma of the time-based void areas. Following Equation (5.17), the data points of each distribution have been randomly divided and subsequently multiplied with the median lifetime of the respective resistance increase criterion. The resulting distributions as a function of resistance increase criterion are plotted in Figure 5.1. Additionally, the corresponding experimentally obtained lifetime distributions are included. The sigma values of the calculated distributions are shown in Figure 5.2 together with experimental values for EM lifetimes as well as both types of void sizes. It can be seen that the agreement between calculated sigma values and experimental ones for the EM lifetime distributions is quite good. Hence, the statistics of the EM lifetime distributions can indeed be simulated by combining the experimentally obtained time-based and resistance-based void area statistics.

Using this observation, instead of trying to directly simulate the EM lifetime characteristics, a separate analysis of the variations of both types of void size measurements can be performed to explain the origins of EM lifetime sigmas. The following section, 5.3, deals with resistance-based void size distributions, while time-based void area characteristics are the topic of Section 5.4.

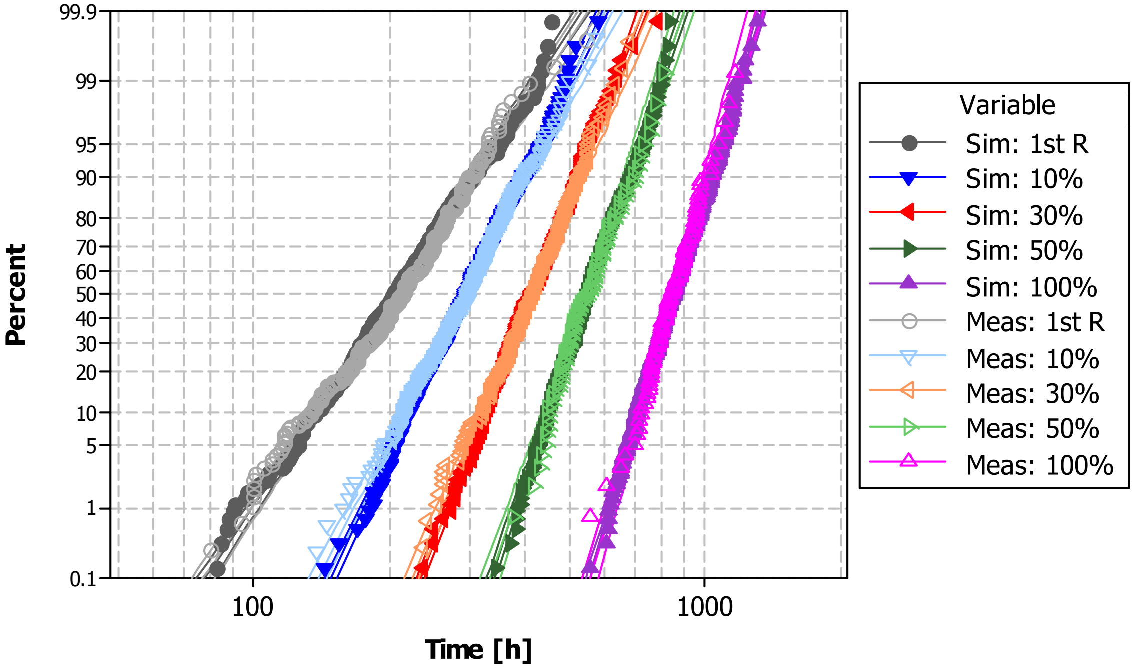

Figure 5.1 Calculated and measured EM lifetime distributions as a function of resistance increase. The measured void size statistics were used for the calculation of the EM lifetime statistics.

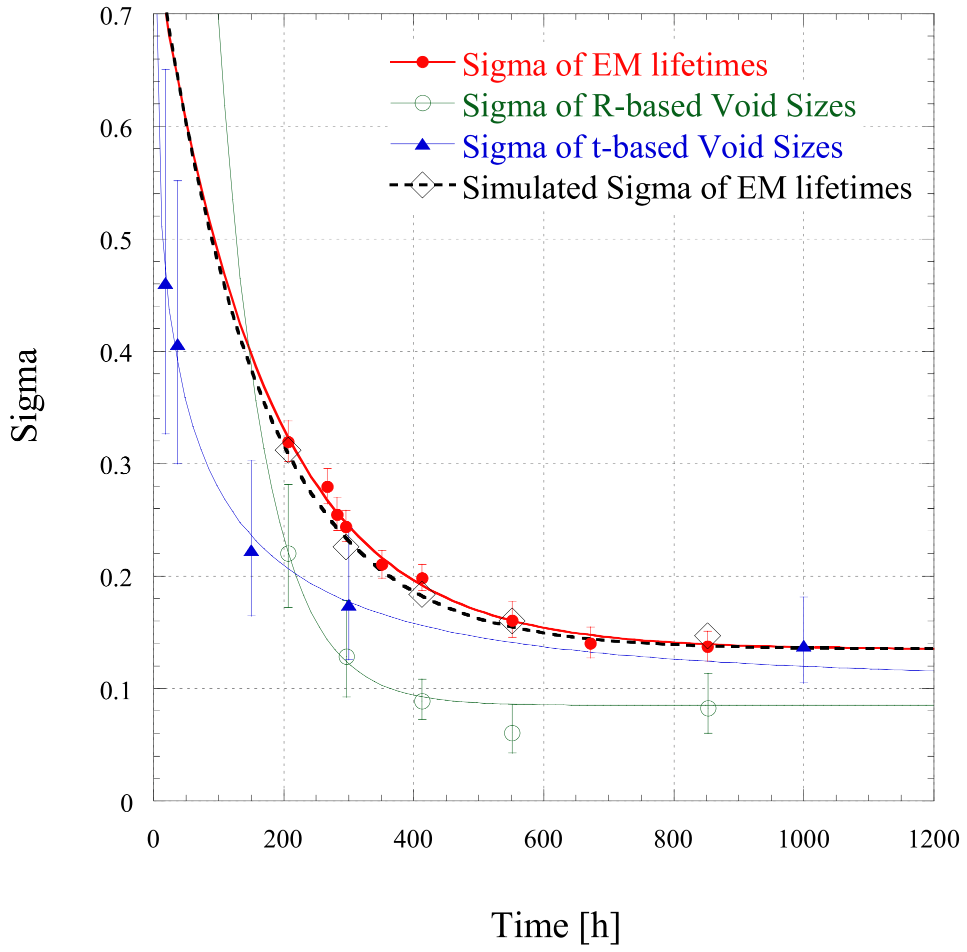

Figure 5.2 The evolution of sigma in time for void sizes corresponding to time-based and resistance-based EM tests as well as for EM lifetimes. For the latter, simulated and measured values are included, showing good agreement.

5.3 SIMULATION OF RESISTANCE-BASED VOID SIZES

In Chapter 4 it was mentioned that the sigma values of resistance-based void area distributions decrease with increasing test time. Furthermore, the sigma values were observed to be significantly smaller compared to values from time-based void sizes as well as EM lifetime distributions. In this chapter, the origins of the statistics of resistance-based void area distributions will be examined in more detail.

To get a specified resistance increase, a certain amount of Cu adjacent to the via needs to be removed, forcing the current through the highly resistive barrier layer. In the following, geometrical arguments will be used to simulate the void areas as a function of resistance increase. In this model, the total void area is divided into three parts as illustrated in Figure 5.3. The first part can be estimated as a rectangle above the via. It is defined as a product of the line length and height above the via. The second component is approximated as another rectangle defined by the void length adjacent to the via which is needed to obtain a certain resistance increase. The third part of the void area is induced by the inclination angle of the void towards the line.

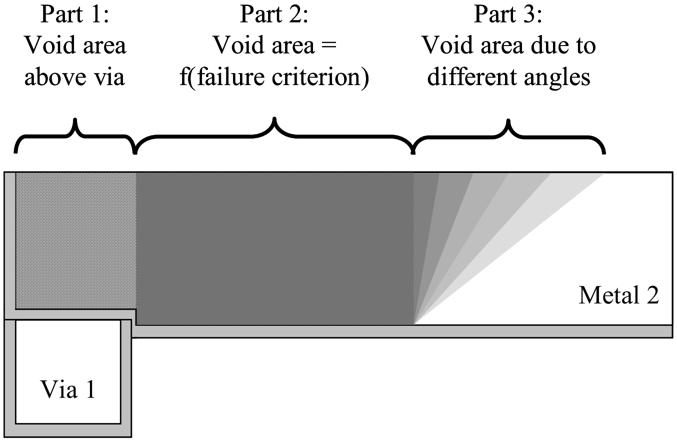

Figure 5.3 Schematic drawing of a voided metal line. For the simulation, the void area is divided into three parts.

For the first part, the line length and height above the via need closer analysis. Both these parameters depend significantly on processing. For some lots, the lines are etched deeper compared to others, leaving the line height above the via smaller than in the rest of the line. Likewise, slight misalignments can occur during processing locating the via slightly to the left or right of the line end. Hence, the line length which corresponds to the line height above the via can be different than the via size. The amount of over-etch and the line length above the via have been measured as a function of lot, and the results are included in Tables 5.1 and 5.2. Even though both parameters are not constant, but vary from sample to sample, the variation is very small, and has thus been neglected. For both variables, the mean values were used for further calculations. In order to calculate the line height above the via for each lot, the mean value of the over-etch distribution has been subtracted from the mean value of the line height, which is listed in Table 3.3. Multiplying the values for line height and length above the via yield the first part of the total void area.

Table 5.1 Statistics of the trench over-etch as a function of lot. All mean and sigma values are measured in μm.

Over-etch of trench	Mean	Lower Mean	Upper Mean	Sigma	Lower Sigma	Upper Sigma	Data Points
D62375.1	0.0289	0.0278	0.0300	0.00335	0.00259	0.00434	15
D62429.1	0.0191	0.0180	0.0201	0.00300	0.00226	0.00397	13
D63327	0.0312	0.0301	0.0324	0.00323	0.00243	0.00430	13
U31275	-0.0037	-0.0049	-0.0025	0.00467	0.00385	0.00566	24

Table 5.2 Statistics of the line length above the via as a function of lot. All mean and sigma values are measured in μm.

Line length above via	Mean	Lower Mean	Upper Mean	Sigma	Lower Sigma	Upper Sigma	Data Points
D62375.1	0.192	0.190	0.195	0.00731	0.00557	0.00958	15
D62429.1	0.218	0.215	0.220	0.00586	0.00441	0.00777	13
D63327	0.230	0.224	0.237	0.01869	0.01430	0.02443	13
U31275	0.215	0.212	0.217	0.00821	0.00675	0.00998	24

The second part of the void area can be calculated following an analysis of the resistance of the interconnect line. The initial resistance of the interconnect prior to the EM test can be estimated to be

$$R_0 = \frac{l}{A_{Cu}} \rho_{Cu} \tag{5.18}$$

where R_0 is the initial resistance, l the line length and ρ_{Cu} and A_{Cu} the resistivity and cross-sectional area of Cu, respectively. Here, it is assumed that the whole current travels through the Cu portion of the line even though the Ta barrier layer provides a parallel conducting path. Since the resistivity of Ta is approximately 70 times larger compared to Cu, this assumption is reasonable. The resistance of the line after the EM test results from the addition of two resistors in series. The first resistor is in the voided region of the line, where the current has to pass through the barrier layer. The second component is the remaining line, where the current passes through Cu. Thus, the total resistance can be calculated according to

$$R = \frac{\Delta l}{A_{Ba}} \rho_{Ba} + \frac{(l - \Delta l)}{A_{Cu}} \rho_{Cu} \tag{5.19}$$

where R is the measured resistance, Δl the length of the void adjacent to the via and ρ_{Ba} and A_{Ba} the resistivity and cross-sectional area of the barrier layer, respectively. In this equation, the void shape has been simplified to be rectangular. The contribution towards the line resistance of the inclined region of the void has been neglected. It can be assumed that the current transfers from the barrier layer to the Cu once some of the line cross-section contains the lower resistivity Cu. However, since the Cu cross-sectional area is smaller during this stage, the contribution to the resistance is larger compared to parts of the line with a completely filled Cu cross-section. Considering the large resistivity of Ta and the fact that this transition region is rather small compared to the void as well as the rest of the line, neglecting the inclination region is a reasonable simplification. Combining Equations (5.18) and (5.19), the resistance change due to void growth can be estimated using:

$$\frac{R-R_0}{R_0}=(\frac{\rho_{Ba}}{\rho_{Cu}}\frac{A_{Cu}}{A_{Ba}}-1)\frac{\Delta l}{l} \tag{5.20}$$

This equation can be rearranged to isolate the void length:

$$\Delta l=\frac{(R-R_0)}{R_0}\frac{l}{(\frac{\rho_{Ba}}{\rho_{Cu}}\frac{A_{Cu}}{A_{Ba}}-1)} \tag{5.21}$$

Thus, in order to calculate the void length adjacent to the via, which induces a certain resistance increase, the resistivities and cross-sectional areas of barrier layer and Cu need to be examined. As mentioned above, the cross-sectional areas have a variation due to process variations. This variation cannot be neglected, since it induces a variation in void length as can be seen from the above equation. Using the experimentally obtained mean and normal standard deviation values as listed in Table 3.1 and 3.2, random distributions for A_{Ba} and A_{Cu} were generated as a function of lot. Depending on the particular experiment, the distribution corresponding to the tested lot was used.

The resistivities of Cu and barrier layer are more difficult to assess. The known values for bulk materials cannot simply be taken, since the material properties of thin films often differ from those of the bulk materials. Furthermore, the resistivity could be a function of lot as well, due to slight process variations. The Cu resistivity can be calculated by inserting the measured values of initial resistance, line length and mean Cu cross-sectional area into Equation (5.18). Mean Cu resistivity values at 300°C of 0.043Ωμm, 0.044Ωμm and 0.042Ωμm were obtained for lots U31275, D63327 and

D62375.1, respectively. These mean values were used in later calculations. In contrast, the resistivity of Ta is not easily measurable. Furthermore, Ta can exist in two different crystal structures, which have vastly different resistivity values. While the body-centered cubic α-Ta has a room temperature resistivity of approximately 0.15Ωμm to 0.3Ωμm, the tetragonal β-Ta has a value of 1.5Ωμm to 2.2Ωμm. Which crystal structure forms depends significantly on processing conditions. While most PVD processes lead to β-Ta films, especially when the film is deposited onto a dielectric material, careful adjustments of processing parameters as well as the use of a TaN underlayer or a CVD process were observed to produce the low resistivity α-Ta [Edelstein 2001, Donohue 2002, Hecker 2002, Demuynck 2003]. Different crystal structures within one film were found as well [Lee 1999, Kwon 2000]. Thus, a variety of resistivities between the commonly known low and high resistivity values were measured on differently manufactured thin films. Since the barrier layer in this case was PVD-Ta on F-TEOS, it is expected that its resistivity is rather high. However, the influence of line geometry on the barrier resistivity has not been considered, which adds another unknown factor. Due to the difficulty of estimating its value, the Ta resistivity has been used as a fitting parameter in the calculation of the void length.

The distribution created for the cross-sectional areas for each lot as well as the appropriate resistivity values were inserted into Equation (5.21) to calculate the void length distribution adjacent to the via for different resistance increases. Good agreement between measured and calculated values could be obtained when using Ta resistivity values of 2.90Ωμm, 2.30Ωμm and 2.65Ωμm for lots U31275, D63327 and D62375.1. The measured and calculated void length distributions are shown in Figure 5.4. The Ta resistivity values correspond to a temperature of 300°C. For a comparison to the above mentioned room temperature values, the temperature coefficient of resistivity (TCR) value of Ta needs to be known. For bulk material, the TCR is approximately 0.0035/K. However, it is known that this value decreases with decreasing feature size. Using a TCR value of 0.003/K, the above Ta resistivities at 300°C transfer to values between 1.21Ωµm and 1.53Ωµm at room temperature, while using a TCR of 0.002/K leads to resistivities in the range of 1.44Ωµm to 1.81Ωµm. These values seem to indicate that predominantly β-Ta exists in these samples, which is in agreement with expectations. In general, all values are in reasonable accord with the literature.

Now, the calculated void length distribution can be used to obtain the second part of the total void area by multiplying each value with the line height. It needs to be remembered that the use of a distribution of void lengths produces a distribution of void areas for the second part of the total void area. This is in contrast to the first part of the void area, which has been approximated as a constant value only varying as a function of lot.

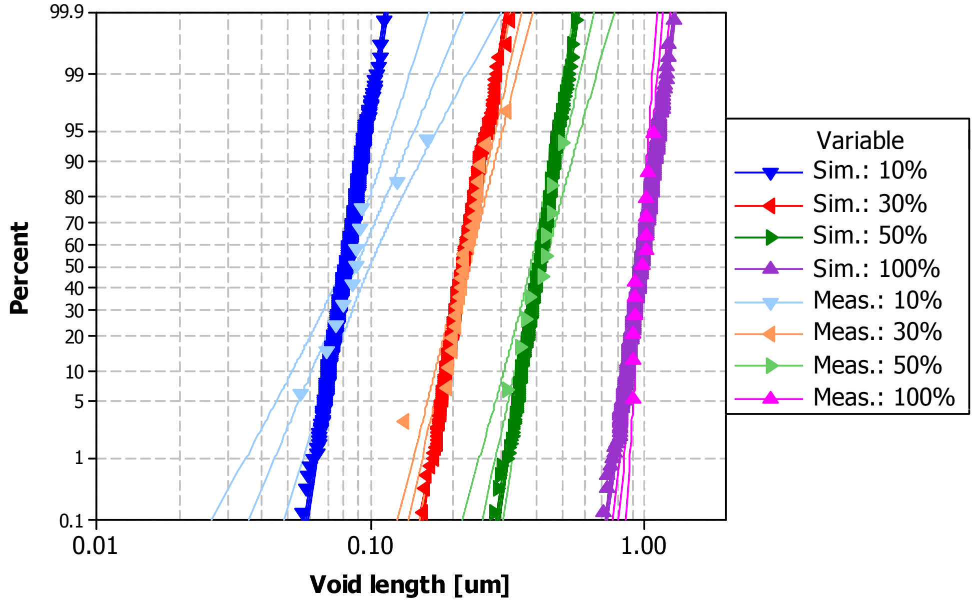

Figure 5.4 Measured and simulated distributions of the void length adjacent to the via for different resistance increase criterions.

The third part of the total void area is defined by the inclination angle of the void towards the line. The inclination can be considered to represent the difference in mass transport between the interface and the average of the line. The statistics of the inclination probably arise because the interfacial mass transport depends on the local grain orientation. The statistical details of the void inclination angle distribution were acquired from measurement. Figure 5.5 shows the cumulative percentage plot using a lognormal distribution fit. The median and sigma values are 56.2° and 0.156. A random distribution of 500 void inclination angles has been generated following the measured statistics. The third part of the void area can be calculated assuming a triangular shape.

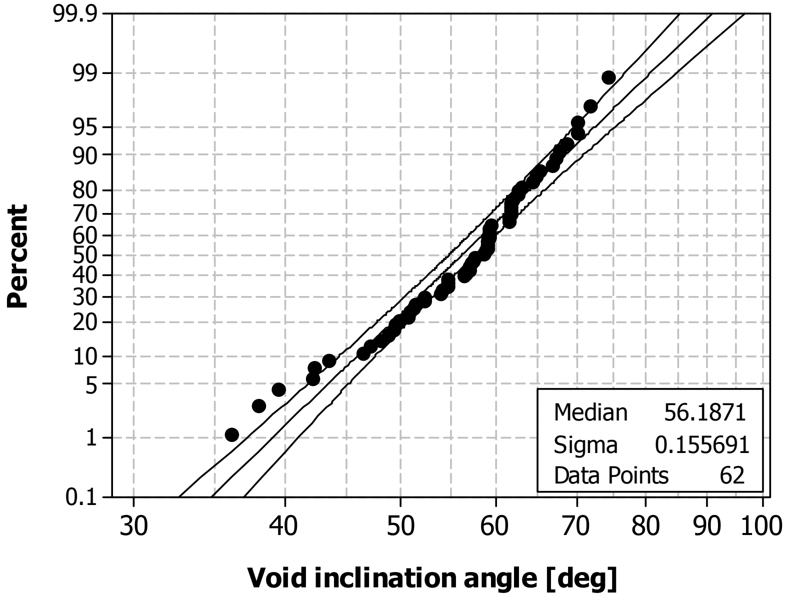

Figure 5.5 Distribution of void inclination angles. A lognormal distribution function was used to fit the data.

The total void area was computed by randomly adding parts two and three to the constant value of part one. In case of the first resistance increase, part two was simply considered to be zero, since the voids corresponding to a first resistance change do not yet extend past the via as shown in Chapter 4. Cumulative distribution plots resulting from this simulation are shown in Figure 5.6 together with experimental data. The evolution of sigma over time for simulation and measurement is included in Figure 5.7. Again, the line fit is simply for illustrative purpose using Equation (4.1)

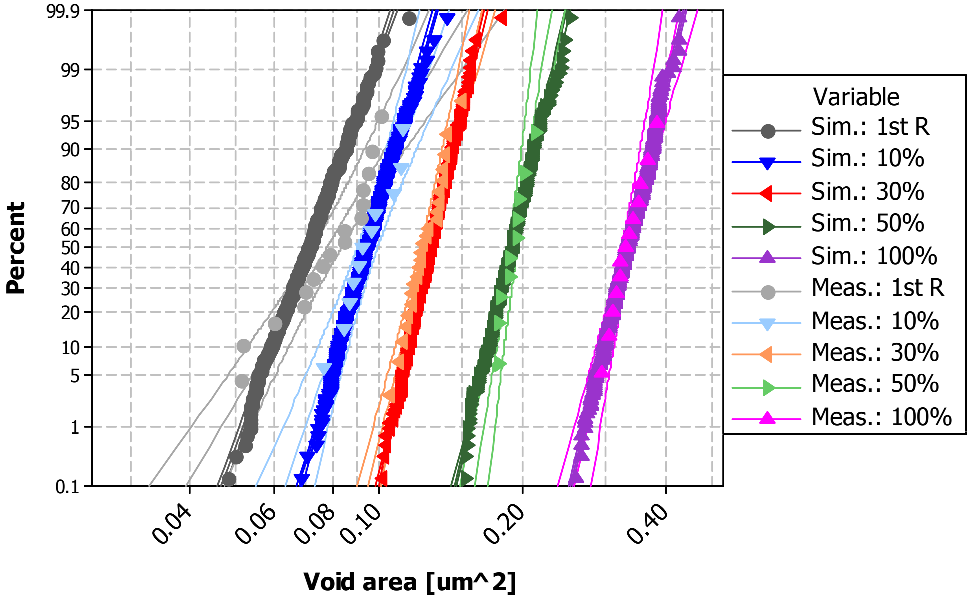

Figure 5.6 Measured and simulated distributions of the void area for different resistance increase criterions.

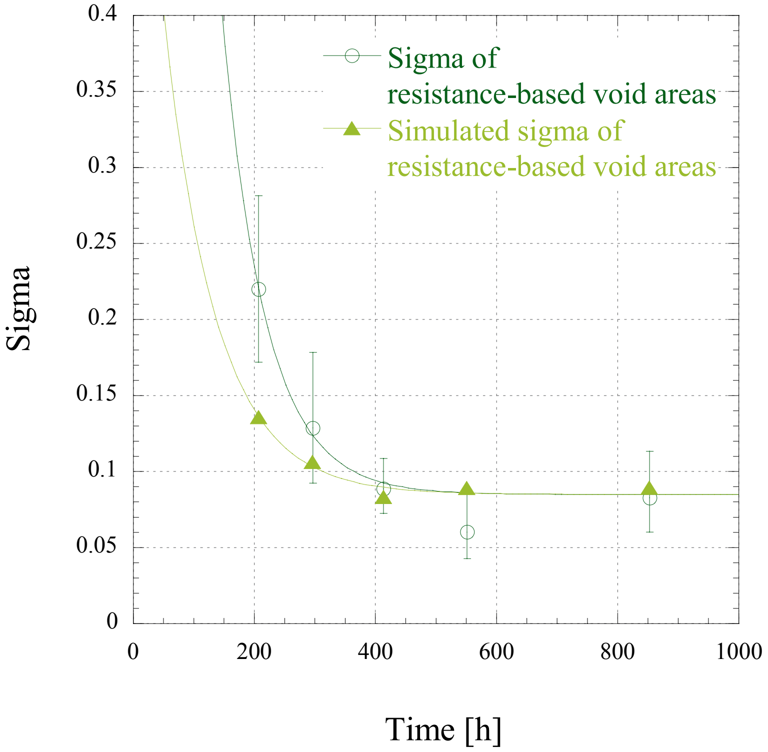

Figure 5.7 Simulated and measured evolution of sigma as a function of time for resistance-based void size distributions.

From both figures, it can be seen that the simulation agrees well with experimental measurements for large void sizes, which result from a 30%, 50% and a 100% resistance increase. However, for small void sizes corresponding to the first resistance increase and the 10% resistance increase, the agreement is not as good. A variety of reasons exist for this disagreement. The major problem for the first resistance increase data is the fact that a first resistance increase can be caused by a variety of differently shaped and located voids as seen in Figures 4.11 to 4.13. A resistance increase can be observed whenever the void reduces the Cu cross-section to a certain value forcing the current through a small area even though it is still Cu. This can be achieved as well when the void has not even reached the cathode end as shown in the

SEM image of DUT 52 in Figure 4.13. This problem is not significant once a larger resistance increase is reached. When analyzing the average void growth behavior, it seemed that already a resistance increase as small as 1% to 5% needs the current to pass through the highly resistive barrier layer. Hence, the void has already reached the cathode end and some length of the line adjacent to the via is free of Cu. However, a disagreement between the simulated and measured void statistics still exists at 10%. Possible reasons are extended interface voids or "left-over" Cu above the via at the cathode end as schematically indicated in Figure 5.8. Examples of both these effects can be seen in the SEM images in Chapter 4. Even though these effects can be seen at all void sizes, the effect of these "artifacts" is much more influential when considering smaller void sizes, such as 10% voids compared to 30% voids for instance.

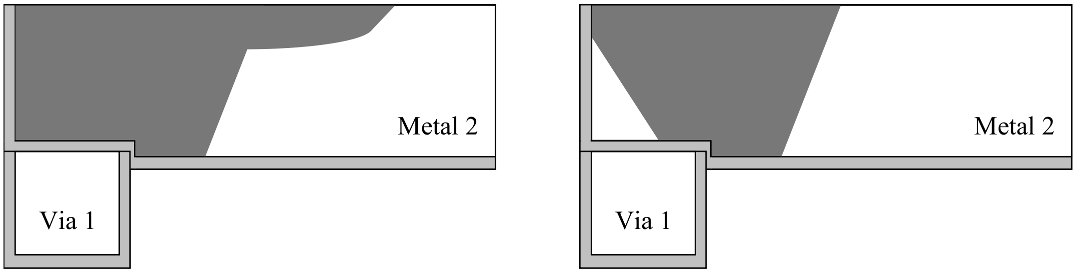

Figure 5.8 Schematics showing possible "artifacts" of the void shape, such as extended interface voids and "left-over" Cu above the via at the cathode end.

In general, however, it can be said that the void size distribution for resistance-based EM tests can mainly be explained by geometrical factors. In contrast, the statistics of void size distributions from time-based experiments depend significantly on kinetic aspects, such as the location of void formation, the time needed for the void to move to the cathode end and diffusivity differences from line to line. The influence of kinetics in addition to geometrical factors leads to larger variations in void sizes qualitatively explaining the larger sigma values for time-based void size distributions. A more quantitative analysis is presented in the following chapter.

5.4 SIMULATION OF TIME-BASED VOID SIZES

As explained in Chapter 5.2, the statistics of the void area for fixed EM test times can be simulated using Equation (5.15). Again, the statistics of the temperature and the Cu cross-sectional area distributions were measured as discussed above. However, the variation in diffusivity from line to line is not easily measurable. Only a combined value together with temperature and Cu cross-sectional area variations can be obtained by measuring the statistics of time-based void areas as discussed in Chapter 5.2. In this chapter, an attempt will be made to understand and simulate the diffusivity variations. Subsequently, all parameters will be combined according to Equation (5.15) to simulate the time-based void size characteristics.

5.4.1 Causes for Diffusivity Variations

Diffusivity variations between lines could be induced by variations in EM testing temperature, wafer processing, and Cu grain orientation. The influence of the temperature has been discussed above. An influence of processing could arise as a result of variations in Cu surface treatment before the deposition of the passivation layer as well as during passivation layer processing. For instance, the pad used during CMP deteriorates over time, thus a wafer processed at the beginning of a pad's lifetime might have a slightly different Cu surface compared to a wafer made just before exchanging the pad. Likewise, slight variations in the CMP slurry, such as the concentration of its components, could lead to differences in the Cu surface from wafer to wafer. In addition, slight variations during passivation layer deposition, for instance in deposition temperature, could potentially influence the interface towards the Cu line. The properties of the interface between Cu and passivation layer depend on the interface quality. Thus, the diffusivity along that interface could show slight variations due to variations in processing. These variations are likely to be largest between different lots, and considerably smaller between different wafers from the same lot. Processing variations across one wafer influencing the interface are not expected to be significant. EM results showing no difference between center and edge dies have been shown in Chapter 4 to support this claim. For this study, samples have been selected from lots with comparable EM behavior to reduce the effect of processing. In the following, it will be seen that indeed the effect is rather small, even though, not completely eliminated.

In addition to effects originating from processing and EM test temperature, it is expected that the diffusion of Cu along the interface depends on the orientation of individual Cu grains. Sommer *et al.* [1996] analyzed silver (Ag) diffusion along a Ag/Cu interface with different interface orientations and diffusion directions. Their results show clear differences in diffusivity depending on interface orientation as well as diffusion direction. As mentioned previously, it has been observed in in-situ EM experiments on Cu interconnects by Meyer *et al.* [2002], Liniger *et al.* [2002], and Zschech *et al.* [2004] that the rate of void growth along the Cu line is not constant indicating as well that the interface structure, or in the case of Liniger *et al.* [2002] the surface structure, can vary depending on Cu grain orientation leading to differences in Cu diffusivity. During EM, Cu ions are moving at the interface for the entire length of the interconnect. Since the Cu grains in the line vary in size and orientation, the moving Cu ions experience a variety of diffusion conditions. Because the Cu lines are long, the average diffusivity of different interconnects is expected to be very similar. However, especially during the initial stages of void evolution, only the grain interfaces close to the cathode end have a significant influence. Even during the formation of the final failure void, only the interfaces within a certain distance from the cathode end are thought to control the removal of Cu from the final flux divergence site. For instance, if all these interfaces cause a slow Cu diffusivity, the void formation would take longer compared to fast diffusing interfaces. Considering only the cathode ends, the average diffusivity can vary from line to line depending on the grain orientations and sizes at each line end.

5.4.2 Statistics of Void Sizes and EM Lifetimes at Long Times

From the explanations in the previous section, it becomes clear that a component of the diffusivity variation is dependent on time, since the number of grain interfaces directly participating in the void evolution increases with time. Hence, the longer the EM experiment, the smaller the variation in diffusivity between lines due to an averaging over more grains. The influence of processing on diffusivity variations is a constant and is established initially depending on the choice of wafers used for the experiments. Likewise, the variations in temperature and Cu cross-sectional area are independent of time. However, their variations were measurable, whereas the variation of diffusivities is not easily obtainable. The constant part induced by processing can be estimated when analyzing the behavior of time-based void sizes at very long times, since in that case, the diffusivity variations are mostly induced by processing variations. Again, at long times, the influence of the averaging effect over different grain interfaces is negligible due to the large number of grains participating in the diffusion process. In the following paragraph, a logical argument will be made extracting an approximation of the influence of processing on diffusivity variations.

It has been discussed in previous chapters that the resistance-based void sizes appear to follow asymptotic behavior at long times with a minimum sigma value of approximately 0.085. Furthermore, the sigma values of EM lifetimes at long times appear to behave asymptotically with a minimum sigma value of 0.135-0.14. Both of these values can be obtained from fitting the experimental data as shown in Figure 4.20. In both cases, Equation (4.1) was used with the parameter *c* set to 1. This choice is advantageous since it reduces the needed variables in Equation (4.1) to three. The asymptotic behavior of both resistance-based void sizes as well as EM lifetimes arises from parameters which are time independent. For instance, in the case of the resistance-based voids, the variation in void length adjacent to the via due to cross-sectional area variations as well as the variation in void inclination angles will always induce a variation in the void area even for very large voids. Likewise, in addition to the ever present resistance-based void area variation, the variations in Cu cross-section and temperature as well as processing induced diffusivity variations induce a non-zero sigma value in EM lifetimes even at very long times. Similarly, the time-based void size statistics are expected to have asymptotic behavior. However, the asymptotic value is more difficult to determine from the experimental data due to the larger error bars. As described in Chapter 5.2, the statistics of both types of void sizes can be combined to estimate the EM lifetime statistics. Hence, the asymptotic values of approximately 0.085 and 0.14 for the resistance-based void sizes and the lifetimes, respectively, which are reached after long testing times, can be used to estimate the asymptotic value of the time-based void size statistics using Equation (5.17). This procedure leads to a sigma value of about 0.105 for the time-based void areas at long times, which results in a good empirical fit through the data as seen in Figure 4.31. Again, this asymptotic value is defined by variations in Cu cross-sectional area, temperature and processing induced diffusivity. The combined effect of the first two can be estimated to be approximately 0.082 using their measured statistics. Hence, considering this contribution in Equation (5.15), the sigma value of the diffusivity distribution at long times is approximately 0.07. This rather small value describes the effect of processing on the diffusivity variation and thus on the statistics of the EM lifetime distributions for the samples selected for this study. As a result of the analysis of the asymptotic behavior, it is obvious that for smaller times the influence of grain orientation as well as grain size distribution on the diffusivity variation needs closer examination.

5.4.3 Statistics of Initial Void Formation

To examine the influence of grain orientation on the diffusivity at the interface, the void evolution process as a function of time needs to be analyzed. As explained in Chapter 4, void formation occurs at the top interface between Cu and passivation layer. The initial void formation site appears to be away from the cathode end at junctions of grain boundaries with the interface. Different Cu grain orientations on either side of the grain boundary can influence Cu diffusivities at the interface such that a flux divergence is being induced, leading to void formation. Hence, the initial void formation sites are predetermined by the microstructure in each Cu line. The difference between the diffusivities of neighboring grains shows where a flux divergence might form during EM, as well as the extent of void formation in a certain time.

A model has been developed simulating this phenomenon. As mentioned in Chapter 3, mainly four grain orientations are generally observed in Cu interconnects, namely {111} orientations, orientations due to sidewall nucleation and due to twinning, and a random component. Corresponding to these orientations, it has been assumed that mainly four different diffusivities exist at the top interface of the interconnect. Even though the last three components individually can have different interface structures, they have been grouped together for simplicity. All four diffusivities are normalized with respect to the fastest diffusivity value. The two middle values are distributed evenly between the slowest and fastest values. The fraction of grains with a certain diffusivity are defined by the grain orientation distribution. In this case, it was assumed that 40% of the grain interfaces are {111} oriented, 15% have a twin orientation and the remaining texture components amount to 22.5% each. The {111} interfaces have been assigned the lowest diffusivity, since they have the lowest surface energy. However, this has not been proven and quantitative information is not available. Furthermore, the twin orientations have been assumed to be the second slowest interfaces.

The difference between these diffusivity ratios defines whether a flux divergence could form between two neighboring grains. Only neighboring grains with the downstream grain having a higher diffusivity can form a void. In order to simulate this behavior, two distributions with 500 values of diffusivity ratios have been randomly created with 40% corresponding to the slowest diffusivity, 15% to the second slowest and 22.5% each to the two remaining diffusivity values. In this case, the fastest diffusivity has been assumed to be 2.5 times faster, compared to the slowest. These distributions have been randomly subtracted from each other, representing the differences in diffusivities of 500 grain pairs. Only positive differences indicate that the downstream grain is faster compared to the upstream grain. Under this condition, the possibility of forming a void exists. Negative differences indicate a slower grain on the downstream site, which reduces the out-flux of Cu from the grain boundary/interface junction. Thus, no void formation can occur. The positive differences have been plotted and fit using a lognormal distribution. Figure 5.9 shows the two initial distributions as well as the final distribution of differences. The sigma value of the latter distribution represents the sigma value of the void volumes at short times when the voids are still at the initial flux divergence sites. For instance, a large difference between diffusivities between two grains produces a larger void in the same time compared to smaller diffusivity differences. The sigma value in this case is approximately 0.4, which coincides well with the sigma values of the time-based void size distributions at very short times (compare to Figure 4.31).

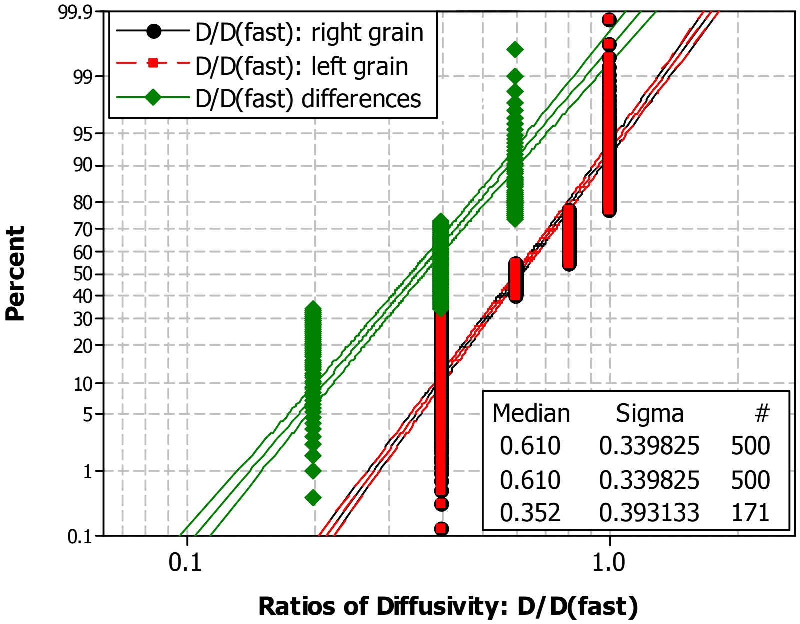

Figure 5.9 Simplified distributions of diffusivity ratios. The diffusivity ratio represents the diffusivity behavior at the top interface of each grain. It is assumed that only 4 different diffusivities exist at the top interface of the line. Two initial distributions are shown, as well as the difference between them. The difference indicates potential flux divergence sites between grains.

Obviously, this model is simplifying the phenomenon greatly. First, the fractions of each diffusivity need to be known, i.e. the orientation distribution and the relation between orientation and diffusivity. Detailed information whether a certain interface promotes slow or fast diffusion is still lacking, even though it seems likely that the {111} interface is the slowest interface due to its low surface energy. A second assumption has to be made regarding the difference between slowest and fastest diffusivity. Unfortunately, a quantitative relationship of diffusivity and orientation for this particular interface is unknown. Additionally, the physics of void formation is more complicated as it is most likely influenced by the type, location and orientation of grain boundaries. However, this model provides some insight on how the differences in orientation might promote variations in void sizes at very short times.

A variety of different cases have been examined. First of all, three different cases have been analyzed regarding the ratio of slowest to fastest diffusivity, namely the fastest diffusivity is twice, 2.5 times and 3 times faster compared to the slowest. All results show a sigma value of about 0.4 for the diffusivity differences distribution. Another simulation included 8 different diffusivity values instead of just 4. Even though 4 main components of grain orientation have been observed, assuming only 4 diffusivities is a simplification, since the interface structures of individual twins or random grains for instance cannot be expected to be exactly the same. This calculation resulted in a sigma value of approximately 0.6 for all three different ratios of slowest to fastest diffusivity. Furthermore, 16 different diffusivity values have been examined. Figure 5.10 shows the original distributions, which are based on the fastest diffusivity being 2.5 times the slowest, as well as the distribution of differences. The latter has a sigma value of about 0.8. Even though the error bar corresponding to the sigma values of time-based void sizes at very small times is quite large (Figure 4.31), this value is outside of the error margin. However, this could be related to the SEM resolution limit. As seen in Figure 5.10, some of the diffusivity differences are very small, approaching zero. Thus, the flux divergence is not very large and the initial void, or vacancy accumulation, may be below the resolution limit of the SEM. This effect could be included in this analysis as a cut-off point for diffusivity differences below a certain value. However, the general idea of flux divergence formation as a result of different grain orientations and its correlation to the initial void sizes and their distribution is illustrated quite well with this simple model.

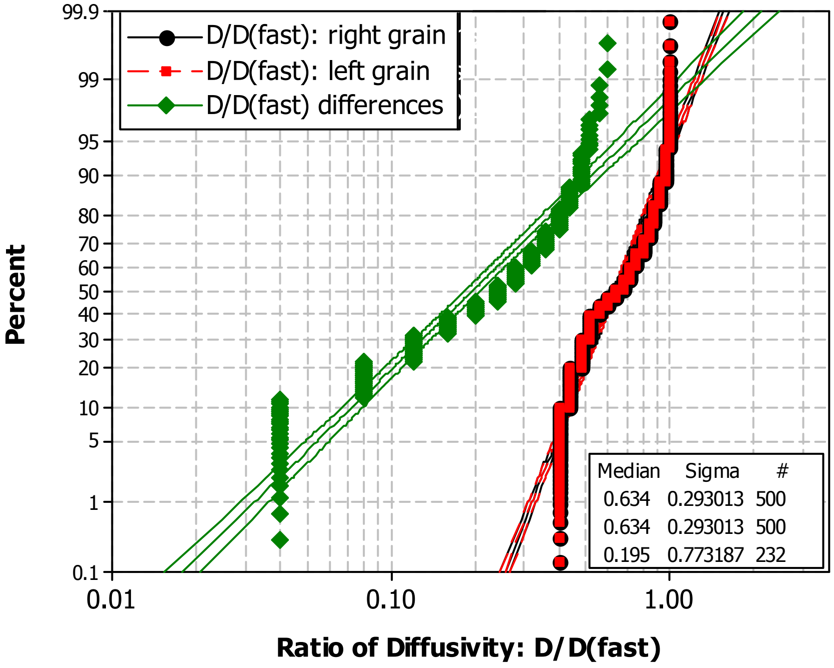

Figure 5.10 Simplified distributions of diffusivity ratios including two initial distributions and the distribution of their differences. It is assumed that 16 different diffusivities can exist at the top interface of the line.

5.4.4 Statistics of Diffusivity Variation during Void Evolution

In the second stage of void evolution, the voids appear to grow at the interface towards the cathode end of the line. Due to a continuous flux of Cu ions along the interface, the initial voids refill, leading to void evolution towards the cathode end. During this stage, the surface of the void acts as a fast diffusion path, removing Cu from the upstream side of the void. Due to this fast diffusion path, the slow diffusivity of the upstream grain, which led to the flux divergence, is not influencing the mass transport significantly at this stage. The void growth is controlled by the interface at the downstream side of the void, which needs to be passed by all incoming Cu ions, whereas the original, slow interface of the upstream grain can be circumvented by using fast surface diffusion. When the void arrives at the cathode end, the final flux divergence site is reached, where the barrier layer between via and line prevents additional Cu from leaving the via and filling the void. In Chapter 4, this period has been labeled the third stage of void evolution. After reaching the cathode end, the voids effectively "turn around" and grow along the line during the fourth stage.

It can be seen that the difference in location of the initial flux divergence site creates a variation in active interfaces, which participate in the void reaching the cathode end. Furthermore, if the initial void is close to the cathode end and/or if the interfaces close to the cathode end all promote fast diffusion, the void can grow larger during the fourth stage compared to samples in which the interfaces are slow or the flux divergences are further down the line. Hence, different numbers of grains participate actively during the fourth stage of void evolution. In short, the location of the initial flux divergence site and the diffusivity of the grain interfaces close to the cathode end define the number of grains actively influencing the void development in each line. Thus, the effective diffusivity is different from line to line depending on each individual diffusion path. It needs to be remembered that the testing time is fixed in the experiments discussed here, so the final void size in each line is directly proportional to the effective diffusivity in that line. In the following, the distribution of the effective diffusivity as a function of time has been modeled using a simplified quantitative model.

Since the diffusivity depends on grain size and orientation distributions, the results of the microstructure analysis as described in Chapter 3 need to be considered.

First, results from the grain size distribution analysis will be revisited. In Figure 3.16, the grain area distribution at the top of 0.18µm interconnects was shown together with a fit using Monte Carlo simulation. Again, twins were counted as separate grains because their interface structure is expected to be different compared to their "parent" grain leading to differences in Cu diffusivity. Using Monte Carlo simulation, a bimodal lognormal distribution was fit to the experimental data. The simulation consisted of 2800 data points. The Monte Carlo simulation was needed to generate a grain pool, which contains a larger number of grains as measured experimentally.

Randomly, each grain interface in the grain pool has been assigned a diffusivity. As in the preceding chapter, it has been assumed that only four different diffusivity values exist within each line. Again, the total grain area with a certain diffusivity is defined by the grain orientation distribution. In this case, it was assumed that 40% of the grain interfaces are {111} oriented, 15% have a twin orientation and the last two texture components amount to 22.5% each, as described previously.

As seen above, with increasing time, a larger final void size is being created. Thus, more grain interfaces directly participate in creating the final void. The area of the top interface, which participates in the void formation is important in estimating the effective diffusivity for each line. Using the grain pool, the diffusivity variation near the cathode end as a function of time can be statistically simulated. However, first the distribution of participating interface areas needs to be obtained as a function of time. The SEM images from time-based experiments form the basis for estimating these distributions.

When examining the voids after 1000h of testing (Figure 4.28), it is obvious that all have grown significantly down the line. The distribution of void lengths measured on top of the voids is shown in Figure 5.11. The use of a lognormal distribution function to fit the data results in a median void length of 1.58µm with a sigma of 0.14. Thus, on average, all interfaces within approximately 1.58µm of the cathode end have definitely participated in the void formation. However, as seen above, most voids started away from the cathode end. Hence, the grain interfaces covering the distance towards the cathode end need to be considered. In order to get an estimate of the distance distribution of the initial flux divergence site towards the cathode end, it has been assumed that the voids after 18.75h and 37.5h of testing are still at their initial location or at least reasonably close to that. Figure 5.12 shows a distribution plot of the distances of these voids towards the cathode end. The distance has been taken to include the void length. The distance distribution of the initial voids has been analyzed using a lognormal distribution function. Its median and sigma values are 0.62µm and 1.07, respectively. In order to get a distribution of the interface area active during 1000h of testing, two distributions with 500 data points each have been randomly created, one using the statistics of the top void length of the final void, the other the median and sigma values of the distance distribution of the initial void formation sites. By randomly adding one value of each distribution with one from the other, the distribution of the interface length active during the 1000h EM test can be estimated. Figure 5.13 shows all described distributions, namely the measured and simulated distributions of the distance of the initial flux divergences to the line end and of the void length after 1000h of EM testing as well as the sum of these, which describes the distribution of effective diffusion paths active during the 1000h EM experiment.

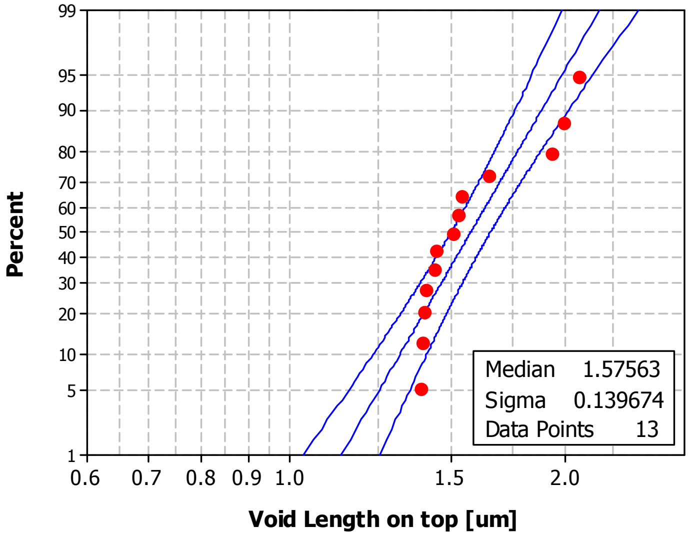

Figure 5.11 The distribution of void length on top of the void after 1000h of EM testing.

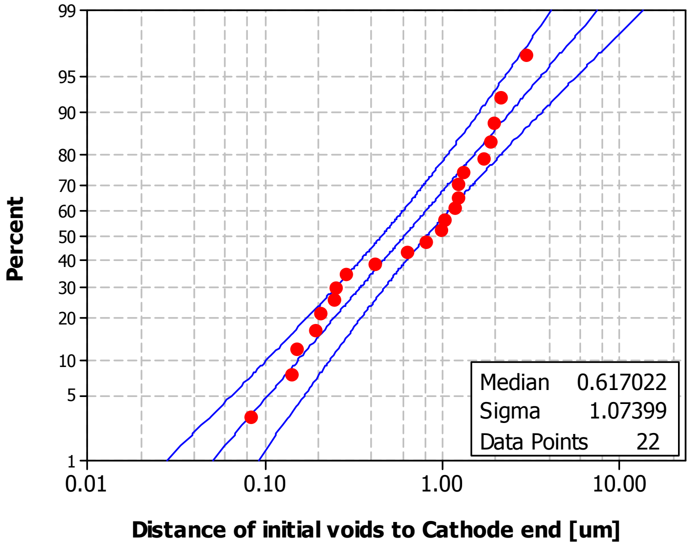

Figure 5.12 The distribution of distances of "initial" voids to the cathode end of the line. Voids after 18.75h and 37.5h have been considered as "initial" voids.

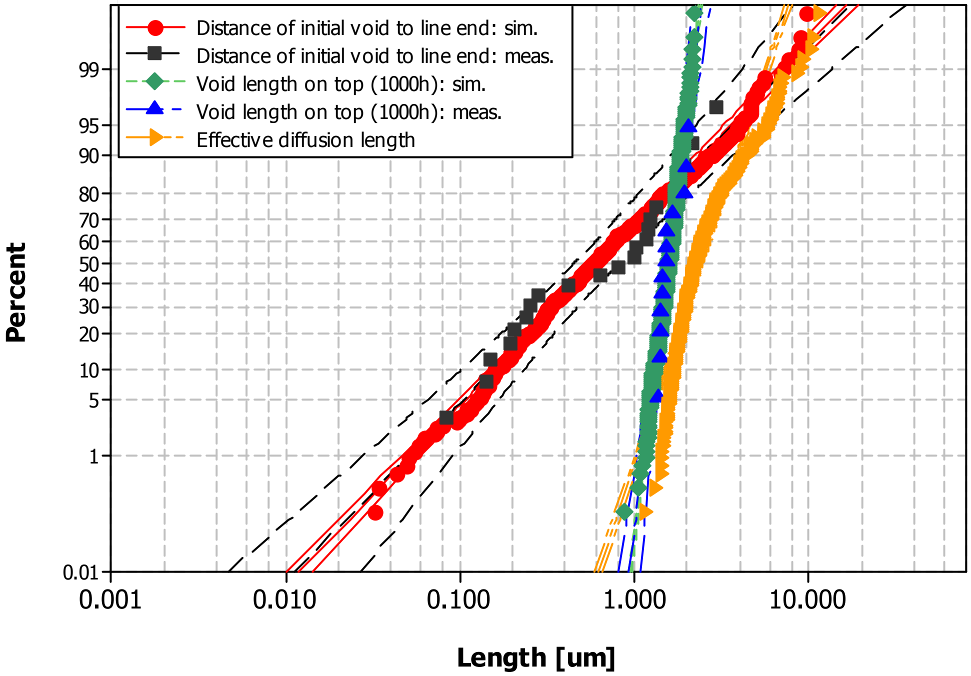

Figure 5.13 Simulated and measured distributions of the distance of "initial" voids to the cathode end of the line and of the void length on top after 1000h of EM testing. The sum of the simulated distributions of these two represents an estimate of the effective diffusion length active during a 1000h EM test.

The effective diffusion paths for the 150h and 300h EM tests are more complicated. In the case of the 300h test, all voids have reached the cathode end, however, only 66% have grown to cover the whole line. Examples of both void types can be seen in Figure 4.27 with the void in DUT 36 still at the top of the line and all other voids already grown down to the via or even past it. This observation has been taken into account for estimating the effective diffusion paths as described in the following. First, the top void length distribution of the voids covering the whole line has been measured. Figure 5.14 shows the distribution, which has a median of 0.57µm and a sigma of 0.109. A random distribution with 333 data points using these statistics has been generated. These values are now randomly added to 333 data points of the distance distribution of the initial flux divergence sites. The resulting 333 data points represent 66% of the total distribution. Since they show similar characteristics compared to the voids in the 1000h EM test, they have been treated similarly. The remaining 167 data points of the initial flux divergence distance distribution are taken to represent the voids, which reached the cathode end, but did not yet "turn around" to grow along the line. The distribution of 500 values containing the data points as just described represents an estimate for the effective diffusion path active during the 300h test.

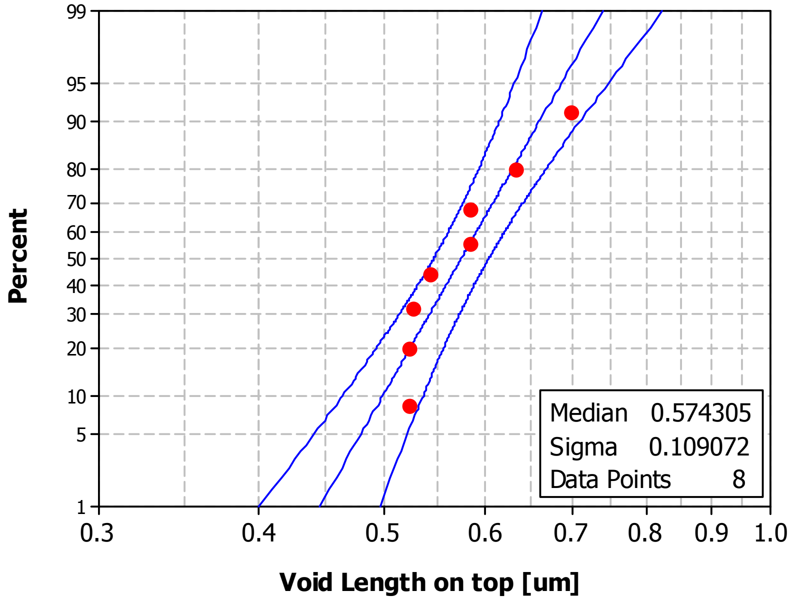

Figure 5.14 The distribution of void lengths on top of the void after 300h of EM testing.

The SEM images of voids resulting from the 150h test show that only 75% of the voids have reached the cathode end. For instance, the SEM images corresponding to DUTs 1 and 22 shown in Figures 4.25 and 4.26 display voids away from the cathode end, whereas the images of the other DUTs show the voids at the end of the line. For 25% of the voids after 150h, not the entire distance towards the cathode end has been significantly participating in forming the void. This observation can be included by analyzing the remaining distance to the cathode end. Unfortunately, imaging has been performed on only 12 samples, only 3 of which have not reached the end of the line. Still, the remaining distance to the cathode end has been measured. A distribution with 125 data points has been fit to the experimental data using the measured median and sigma values. Figure 5.15 shows the experimental data as well as the simulated distribution. Now, these 125 data points have been randomly subtracted from the distance distribution of the initial flux divergence sites. It has been assured that only positive values result from this calculation. These data points represent the shorter effective diffusion paths for the 25% of voids, which have not reached the cathode end. 375 data points remain in the distance distribution of the initial void formation site after performing the subtraction process. These values are used to represent the effective diffusion path for the 75% of voids, which reached the end of the line within 150h. The combined distribution provides an estimate of the distribution of interface lengths participating actively in void formation during a 150h EM experiment.

Figure 5.16 shows three graphs corresponding to the distributions of the effective diffusion paths during EM tests for 150h, 300h and 1000h. It can be seen that the median value increases with time, simply because more interfaces are active at longer times. Furthermore, the sigma value decreases with increasing test time. The total interface area, which participates actively in void formation, has been calculated by multiplying every length value with the line width. Here, a constant value of 0.162μm has been assumed, which is the average line width resulting from 122 measurements as listed in Table 3.5. Obviously, the line width in itself has a variation resulting from process variations. However, it is small compared to the variation in effective diffusion lengths, and has thus been neglected here.

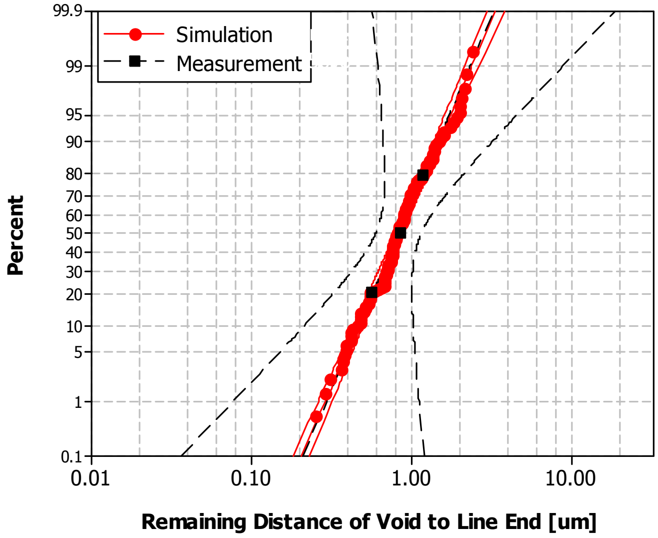

Figure 5.15 Simulated and measured distributions of the remaining distance to the cathode end of voids, which have not reached the end of the line after 150h of EM testing.

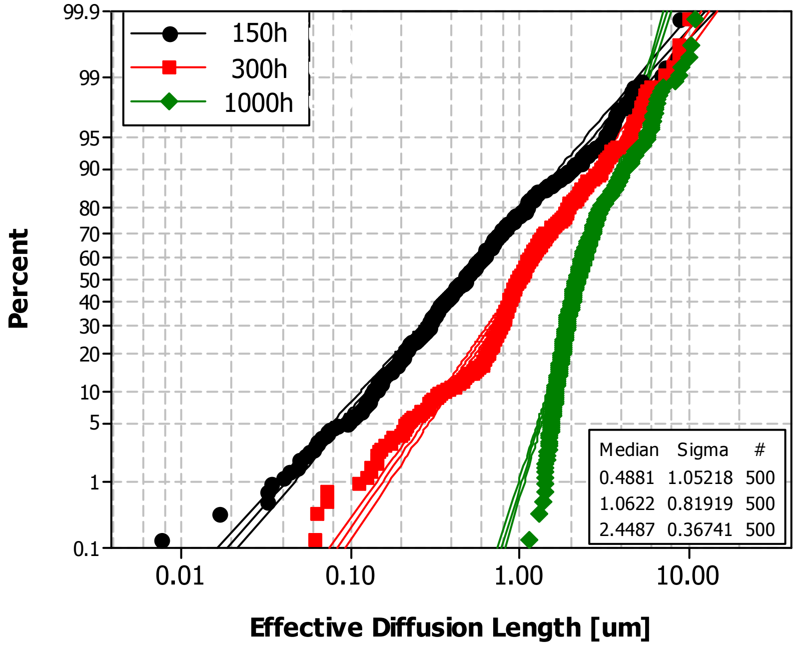

Figure 5.16 An estimate of the distributions of effective diffusion lengths active during 150h, 300h and 1000h of EM testing.

Now, the variations in active interface area as a function of time and the microstructure in the Cu lines as represented by the grain pool can be used to estimate the statistics of the effective diffusivity as a function of testing time. A program to perform the diffusivity simulation has been written in MATLAB [MathWorks, Inc.]. For each interface area distribution, grains have been randomly picked out of the grain pool, so that their areas add to the individual values for the active top surface. Approximately 10, 16 and 29 grains are needed for EM tests lasting 150h, 300h and 1000h, respectively. Subsequently, the average diffusivity has been calculated for only these grains leading to a value for the diffusivity at the cathode end of each line. Since each interface area distribution contains 500 data points, this procedure allows the calculation of the effective diffusivity of 500 interconnects at each time. Thus, the diffusivity distributions are statistically relevant.

It needs to be remembered that certain assumptions were made for this model. Some of them were already discussed in the previous chapter, such as the uncertainty in the relation between orientation and diffusivity and the difference between slowest and fastest diffusivity. Furthermore, the distributions of the active interface areas are based on some simplifications. First of all, they were derived from only limited data, since only approximately 12 SEM images were available per test condition. Furthermore, the addition and subtraction procedures do not represent the physics of void evolution properly. Basically, the effective diffusion path during void evolution has been treated as two separate parts with one being active before the void reaches the cathode end and the other afterwards. Obviously, it is still the same line with the same microstructure after the void “turns around”. Hence, treating the two parts as completely unrelated is not perfectly accurate. However, for the sake of simplicity, this treatment is probably reasonable.

Several cases have been examined for the ratio of fastest to slowest diffusivity, namely the fastest diffusivity is twice, 2.5 times and 3 times faster compared to the slowest. Figure 5.17 shows the sigma values of the diffusivity distributions as a function of time for different assumptions. It is obvious that the sigma values show a strong dependence on the input parameter. Hence, for a more quantitative analysis a more careful examination of the assumptions is necessary. However, the trend in sigma as a function of time remains identical for all examined cases, i.e. the sigma values of the diffusivity distributions decrease with increasing test time. Since the diffusivity is averaged over more grains with increasing failure criterion, the diffusivity variation from line to line decreases.

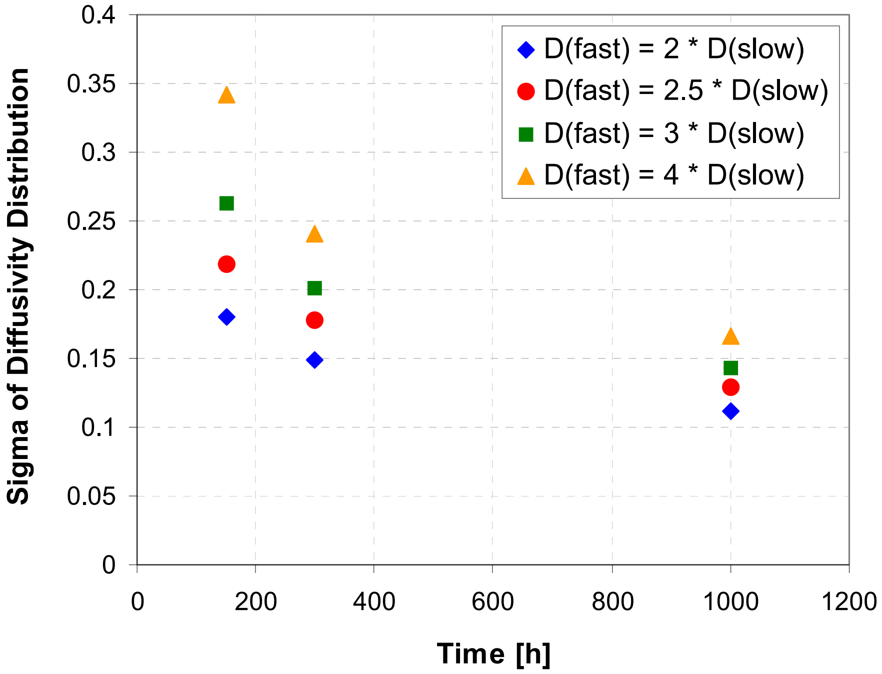

Figure 5.17 Sigma values of diffusivity distributions as a function of the ratio between fastest and slowest diffusivity. The value of sigma depends significantly on the input parameter, however, the trend of decreasing sigma over time is identical for all cases.

The diffusivity distribution can be included into Equation (5.15) together with the temperature and Cu cross-sectional area distributions to obtain the statistics of the time-based void areas. The results of the simulation together with experimental data are shown in Figure 5.18. The plot displays the evolution of sigma values of time-based void sizes over time. The experimental values as well as simulated values for different ratios of fast to slow diffusivity are included. The variation of the initial voids has been included in this graph. Experimental and simulated sigma values agree very well under the assumption that the fastest diffusivity is 2.5 times higher than the slowest one. In general, it is observed that the evolution of sigma with time is reproduced very well with this simulation.

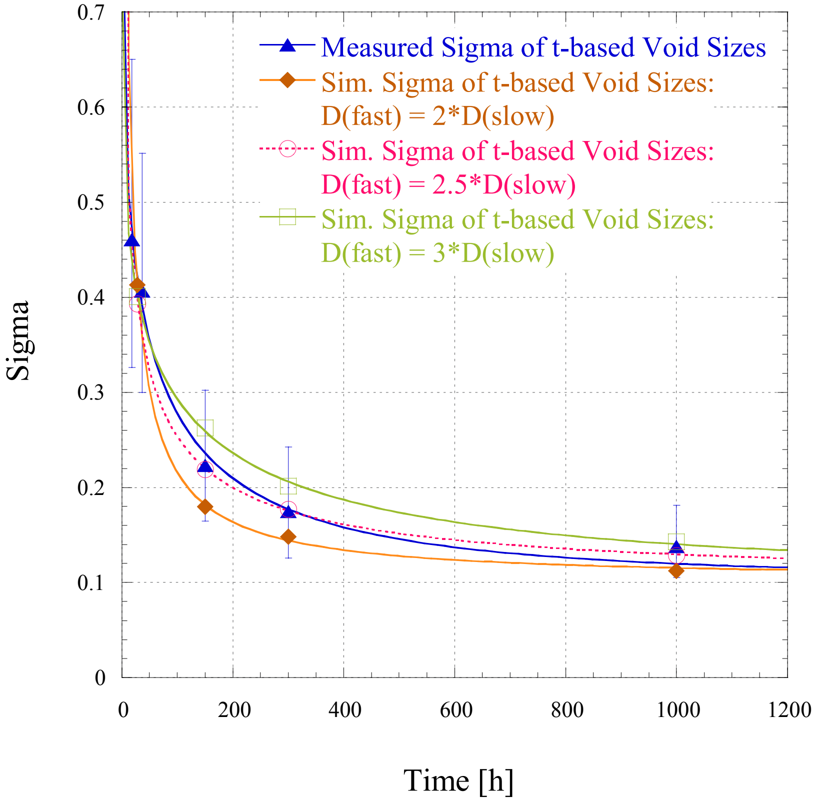

Figure 5.18 The evolution of sigma in time for time-based void size distributions. The experimental values as well as simulated values for different ratios of fast to slow diffusivity are included.

5.5 DISCUSSION OF SIMULATION RESULTS

This study has outlined the parameters influencing the sigma value of EM lifetime distributions. The impact of some parameters can be influenced. For instance, a tight temperature distribution in the EM oven is necessary for a good final sigma value. Likewise, it is necessary to have good process control in order to keep the variation in Cu cross-sectional areas as small as possible. Once these two conditions are fulfilled, the impact of these parameters on the variations of EM lifetimes is small as seen above.

Furthermore, the sigma values of EM lifetimes are influenced by the statistics of resistance-based void size distributions. These can be improved as well by good process control for the line geometry. However, the variation in void inclination angle contributes significantly to the void size distribution characteristics. This variation appears to be difficult to improve. Apart from the void size distribution, the diffusivity variation from line to line at the cathode end seems to induce a rather large effect on the sigma value of EM lifetimes. This result indicates that the Cu microstructure in the trenches does have an influence on the EM performance. Hence, an improved control of the grain size as well as the orientation distribution could potentially decrease the sigma values of the EM lifetime distributions. An exact control and possible modification of the microstructure in 0.18µm Cu interconnects, however, is challenging.

This study allows an estimate of the EM statistics for future interconnect generations. Understanding the origin of the lognormal sigma for a certain process technology and design enables the prediction of the expected sigma value for smaller and smaller interconnect lines. In the case that the EM mechanism is identical or similar to the one described in this study, i.e. the top interface is the major diffusion path and the final failure voids are at the cathode end above the via, the parameters influencing EM characteristics remain the same as identified in this work. Thus, by assessing their statistics as a function of technology generation, the EM lifetime statistics can be predicted. The geometrical parameters can be gauged through an analysis of tool capabilities, such as line width control, barrier deposition uniformity, and post-CMP thickness variability. Void area statistics can be obtained using the geometrical model described in Section 5.3 once the geometric variations have been examined. This procedure was seen to provide adequate results for resistance increases exceeding 30%. If the examination of smaller resistance increases is required, the systematic deviations as mentioned in Section 5.3 need to be considered. There is no definite statement on which resistance increase should be used, since different companies use different criteria for their reliability assessment. In general, the critical void volume leading to appreciable resistance increase is easily accessible through the knowledge of metal line target width and thickness values and via sizes for each technology node. The evolution of the Cu microstructure as a function of geometry and the effect of growth restriction can be estimated through experimental analysis of very fine line patterns, utilizing TEM analysis. Initial results showing the grain size distribution in 0.12μm lines were already discussed in Chapter 3. It was observed that the characteristics of the grain size distribution scale with line width reflecting the growth restrictions imposed by finite line dimensions. Considering this result simulation work can be performed to predict the Cu grain size distribution as a function of interconnect dimensions. Utilizing the model developed in this study, the diffusivity variation as a function of technology node can then be examined. Subsequently, the diffusional void growth mechanism can be simulated and the corresponding lognormal sigma value of EM lifetimes can be predicted. The change in median lifetime as a function of technology generation can be estimated using the observation that the lifetime of Cu interconnects scales with the height of the line [for instance: Rosenberg 2000]. Combining both analyses, the maximum sustainable operational current density for a certain metallization scheme such as the Cu/SiN$_x$ system can be estimated following the extrapolation methods described in Chapter 1. This procedure can then be repeated as a function of scaling factor between each future technology node. A comparison of estimated maximum sustainable current densities with the values given in the ITRS roadmap [ITRS 2004] or with company-specific expected transistor drive currents, frequencies and supply voltages enables a decision about the insertion of a novel metallization scheme. Once the extrapolated maximum current density falls below the required specification, an enhancement of the EM performance is needed. As mentioned earlier, most promising candidates are overlayers such as CoWP or Cu alloys. Here, the substantial enhancement in lifetimes can be offset by a degradation of the lognormal sigma value, due to a profound change in the EM failure mechanism such as the activation of the Cu/barrier interface. This change will need careful analysis and attention to achieve a thorough understanding of the new mechanisms at hand.

Chapter 6: Effect of Process Parameters on EM Statistics

It has been observed that the EM lifetime statistics depend on experimental parameters of the EM test, such as temperature variation in the oven, process induced variables, namely variations in line dimensions, and void size and mass transport statistics. Mass flux characteristics have been analyzed assuming a variation in diffusivity at the cathode ends of different interconnects due to the local microstructure. In order to provide additional support for this model, the effect of several processing parameters on EM statistics will be examined in this chapter. First, the EM characteristics of interconnects with smaller line height will be compared to the data originating from "regular" height samples. Secondly, the influence of a different passivation layer, namely SiC instead of SiN_x, will be analyzed. Finally, the effect of dual damascene technology on the EM mechanism will be examined and compared to the single damascene integration. Again, the analysis of these process parameters focuses on their influence on the EM lifetime distribution statistics.

6.1 ANALYSIS OF VARYING LINE HEIGHT

In order to produce samples with smaller line height, some wafers were exposed to additional chemical mechanical polishing. These wafers were taken from lot D76814. Figure 6.1 shows SEM images of two cross sections of the interconnect line with (a) displaying a sample with reduced height and (b) a sample with regular height. It can be seen that the line width is similar, whereas the height is significantly smaller in the sample shown in Figure 6.1(a). Distributions of Cu cross-sectional area, Ta cross-sectional area and Cu line height for these samples as well as samples from lot D62375.1 are shown in Figures 6.2-6.4. For simplicity, the dimensional distributions corresponding to only one lot with regular height were chosen for these plots. Lot D62375.1 was selected, since the dimensions of the baseline samples from D76814 appeared to be quite comparable to this lot. The statistics of the dimensional parameters of the reduced height samples are listed in Table 6.1. In addition to the cross-sectional areas of Cu and Ta and the Cu line height, the average line width and the line width on top of the line are included in Table 6.1. All measurements are obtained as described in Chapter 3 for the baseline samples. Likewise, a normal distribution function with 80% two-sided confidence bounds has been used to fit the distributions. It can be seen that the cross-sectional areas of Cu and Ta and the line height are significantly smaller. Comparing them to the mean values of all baseline data, the areas of Cu and Ta and the line height are approximately 26%, 20% and 26% smaller than the regular height samples. The observation that the Ta cross-sectional area is reduced less compared to the other dimensional parameters can be attributed to the fact that less Ta is on the side walls of the trench compared to the bottom. Thus, proportionally, less Ta is being removed during the additional CMP step. This difference impacts the ratio of Cu to Ta cross-sectional areas, which is reduced to about 4.64 in reduced height samples from an average of 5.05 for baseline samples. The Cu line widths on top as well as the average value are very similar for all samples. The measured mean values are within 1% to 2% of each other. When examining the sigma values of the dimensional parameters of the reduced height samples, it appears that they are approximately 5% of the corresponding mean values. This is very comparable to the baseline samples, for which the sigma values were about 4% to 8% of the respective mean value. This observation is important, since it indicates that the statistical variation in dimensional parameters is comparable for reduced and regular height samples.

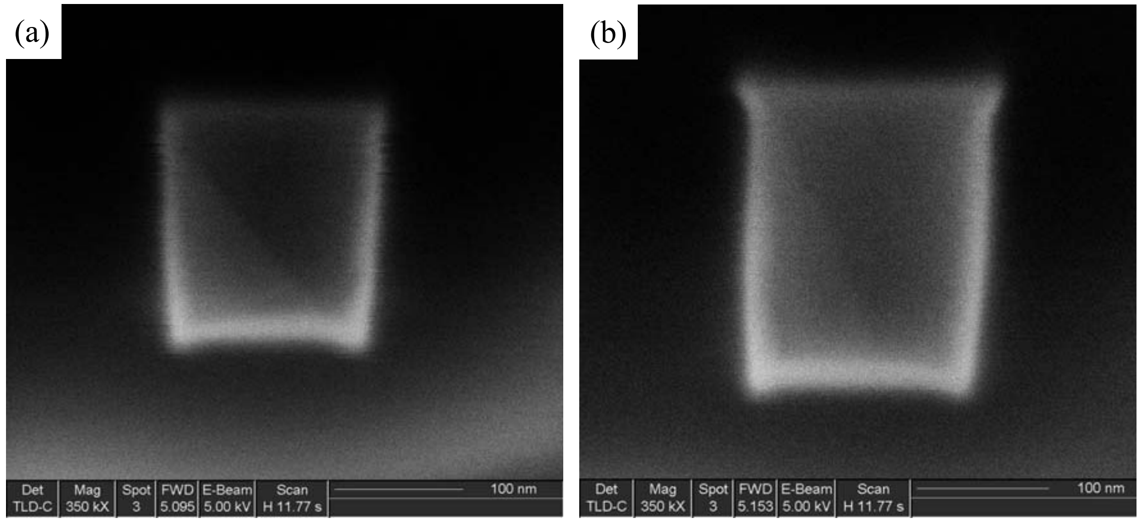

Figure 6.1 SEM images showing the cross-section of interconnect lines for (a) a reduced height sample and (b) a regular height sample.

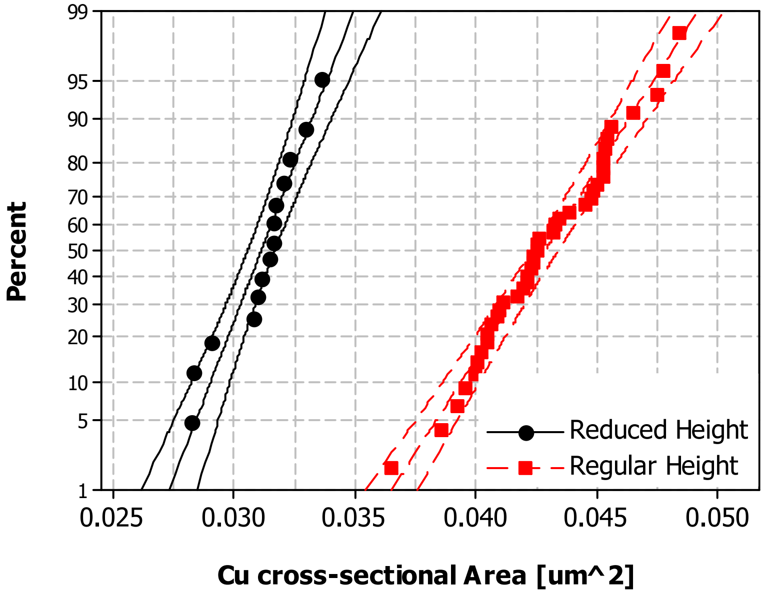

Figure 6.2 Distributions of the Cu cross-sectional area for reduced and regular height samples. For simplicity, only the data from D62375.1 is shown for the baseline case.

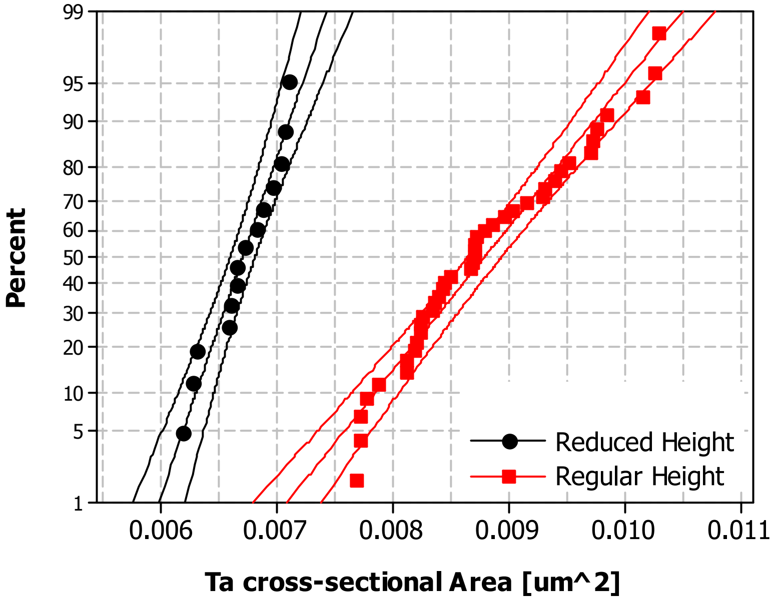

Figure 6.3 Distributions of the Ta cross-sectional area for reduced and regular height samples. For simplicity, only the data from D62375.1 is shown for the baseline case.

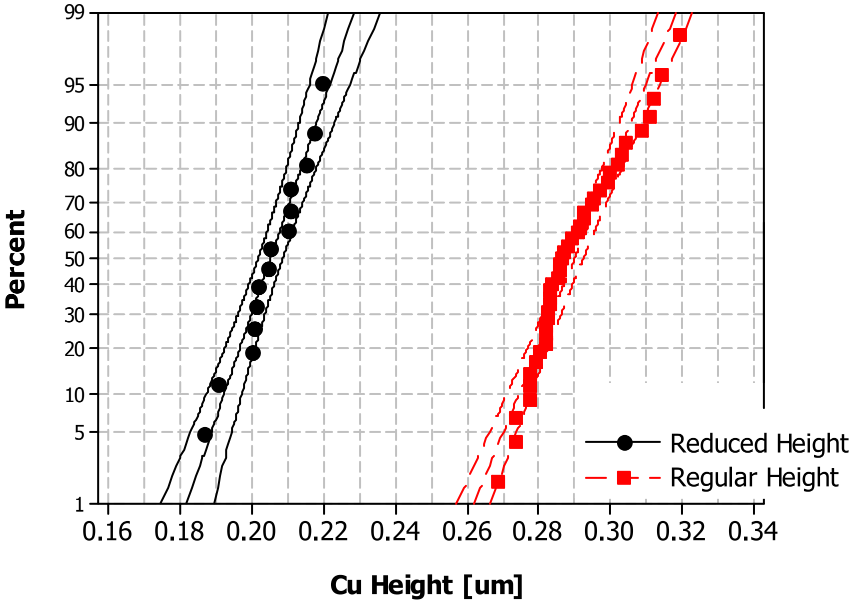

Figure 6.4 Distributions of the line height for reduced and regular height samples. For simplicity, only the data from D62375.1 is shown for the baseline case.

Table 6.1 Statistics of dimensional parameters for reduced height samples. 14 samples were measured. The mean and sigma values of the cross-sectional areas are measured in μm^2, whereas the height and width measurements are in μm.

Reduced Height Samples	Mean	Lower Mean	Upper Mean	Sigma	Lower Sigma	Upper Sigma
Cu X-sectional Area	0.0311	0.0306	0.0317	0.00164	0.00125	0.00214
Ta X-sectional Area	0.0067	0.0066	0.0068	0.00031	0.00024	0.00041
Cu Line Height	0.205	0.202	0.209	0.01004	0.00760	0.01326
Cu Line Width (av.)	0.158	0.157	0.160	0.00361	0.00272	0.00478
Cu Line Width (top)	0.148	0.147	0.149	0.00301	0.00228	0.00398

As mentioned in Chapter 3, the current applied in the EM test of reduced height samples was decreased, so that the current density in all samples was comparable. All other EM test conditions were identical, i.e. the temperature and the test structure. EM lifetime distributions for the reduced and regular height samples are shown in Figure 6.5. The failure criterion used in this case was a 10% resistance increase. It can be seen that the median time-to-failure decreases with line height, whereas the sigma value appears to be comparable. Table 6.2 and 6.3 list the EM statistics of both sample types as a function of resistance increase failure criterion. For all resistance increase criteria, the above observation can be obtained, i.e. the median time-to-failure decreases with line height, while the sigma value remains comparable. The ratios of median lifetimes indicate that the samples with reduced height fail about 30% earlier than the baseline samples. This is in good agreement with the dimensional reduction of approximately 26% for the line height as well as the Cu cross-sectional area. It can be seen in Equation (2.10) that the effective drift velocity in an interconnect has an inverse relationship with the Cu line height. Due to the decrease in line height, the effective drift velocity increases leading to earlier failure. Intuitively, this can be understood by examining the active diffusion mechanism. As analyzed in detail, Cu ions move away from the cathode end along the top interface. The interface area available for transport remains identical upon changing the line height. However, less Cu ions have to leave and diffuse through that interface when the line height is decreased. Thus, the time needed to obtain a certain resistance increase decreases. This effect has to be considered when scaling to future technology nodes [Rosenberg 2000].

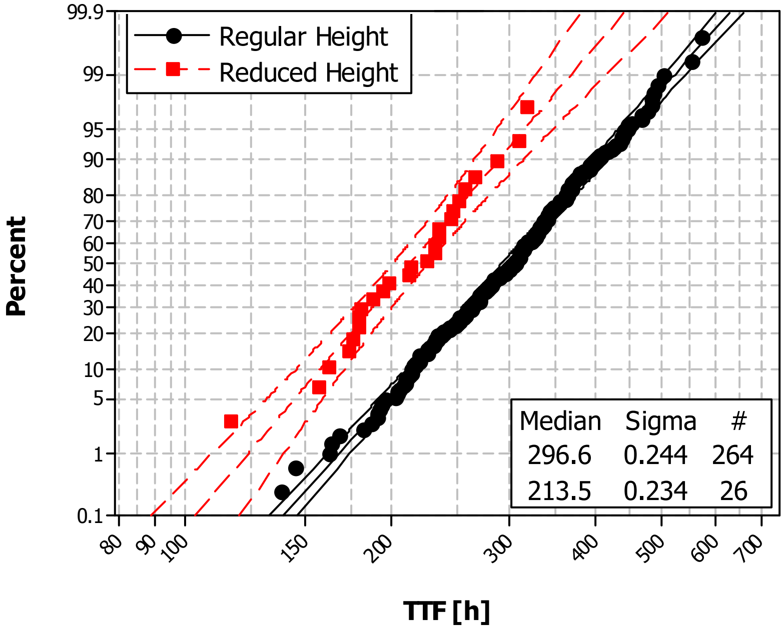

Figure 6.5 EM lifetime distributions for the reduced and regular height samples corresponding to a 10% resistance increase failure criterion.

Table 6.2 Statistics of EM lifetime distributions for reduced height samples as a function of resistance increase failure criterion.

Reduced Height Samples	Median	Lower Median	Upper Median	Sigma	Lower Sigma	Upper Sigma	Data Points
1% R Change	173.7	162.3	186.0	0.270	0.223	0.328	26
5% R Change	204.2	191.6	217.7	0.254	0.210	0.307	26
10% R Change	213.5	201.3	226.5	0.234	0.194	0.284	26
20% R Change	264.1	250.9	278.0	0.204	0.169	0.246	26
30% R Change	315.7	301.3	330.8	0.185	0.154	0.224	26

Table 6.3 Statistics of EM lifetime distributions for regular height samples as a function of resistance increase failure criterion.

Regular Height Samples	Median	Lower Median	Upper Median	Sigma	Lower Sigma	Upper Sigma	Data Points
1% R Change	267.4	261.5	273.3	0.279	0.264	0.296	263
5% R Change	282.1	276.5	287.9	0.255	0.241	0.270	264
10% R Change	296.6	291.0	302.4	0.244	0.231	0.258	264
20% R Change	351.4	345.4	357.5	0.210	0.198	0.223	246
30% R Change	413.1	406.5	419.8	0.198	0.187	0.210	245

As already mentioned, the sigma values of EM lifetime distributions of reduced and regular height samples are comparable for all resistance increase failure criteria. This can be understood when examining the resulting void sizes in detail and following the analysis method described in Chapter 5. SEM images showing 4 reduced height interconnects with voids at the cathode end, together with their resistance traces are displayed in Figure 6.6. These samples were tested to a 30% resistance increase failure criterion. In general, the failures appear to be similar to the baseline samples with all final failure voids being located at the line end. This is expected, since the change in line height should not alter the active diffusion mechanism controlling the void evolution behavior. A total of 15 samples were cross-sectioned to obtain their void size statistics. The distributions of void area, void length on top and void length adjacent to the via are shown in Figures 6.7-6.9 together with the corresponding distributions of the baseline samples tested to a 30% resistance increase. The respective statistics of void area, void length on top and void length adjacent to the via are included in Table 6.4 for the reduced height samples. For comparison, Table 6.5 contains the equivalent values for the baseline. Due to the decrease in line width, the median void area in the reduced height samples is smaller, however, only by about 15%. Likewise, the void length adjacent to the via deviates from the baseline by approximately 15%, showing a larger value for the reduced height data. Interestingly, the void length on top of the line is very similar for both types of samples. Furthermore, the sigma values of the reduced height samples agree well with the baseline values for all void measurements.

The observed statistics can be understood when examining the void sizes following the approach of the geometrical model described in Chapter 5.3. Using Equation (5.21), the void length adjacent to the via can be calculated. As mentioned above, the ratio of Cu to Ta mean cross-sectional areas is reduced by about 10% for the smaller line height samples. Thus, from Equation (5.21) it can be expected that the void length adjacent to the via needs to be about 10% larger to reach the same resistance increase value. Due to the small sample size, this is in reasonable agreement with the observed 15%.

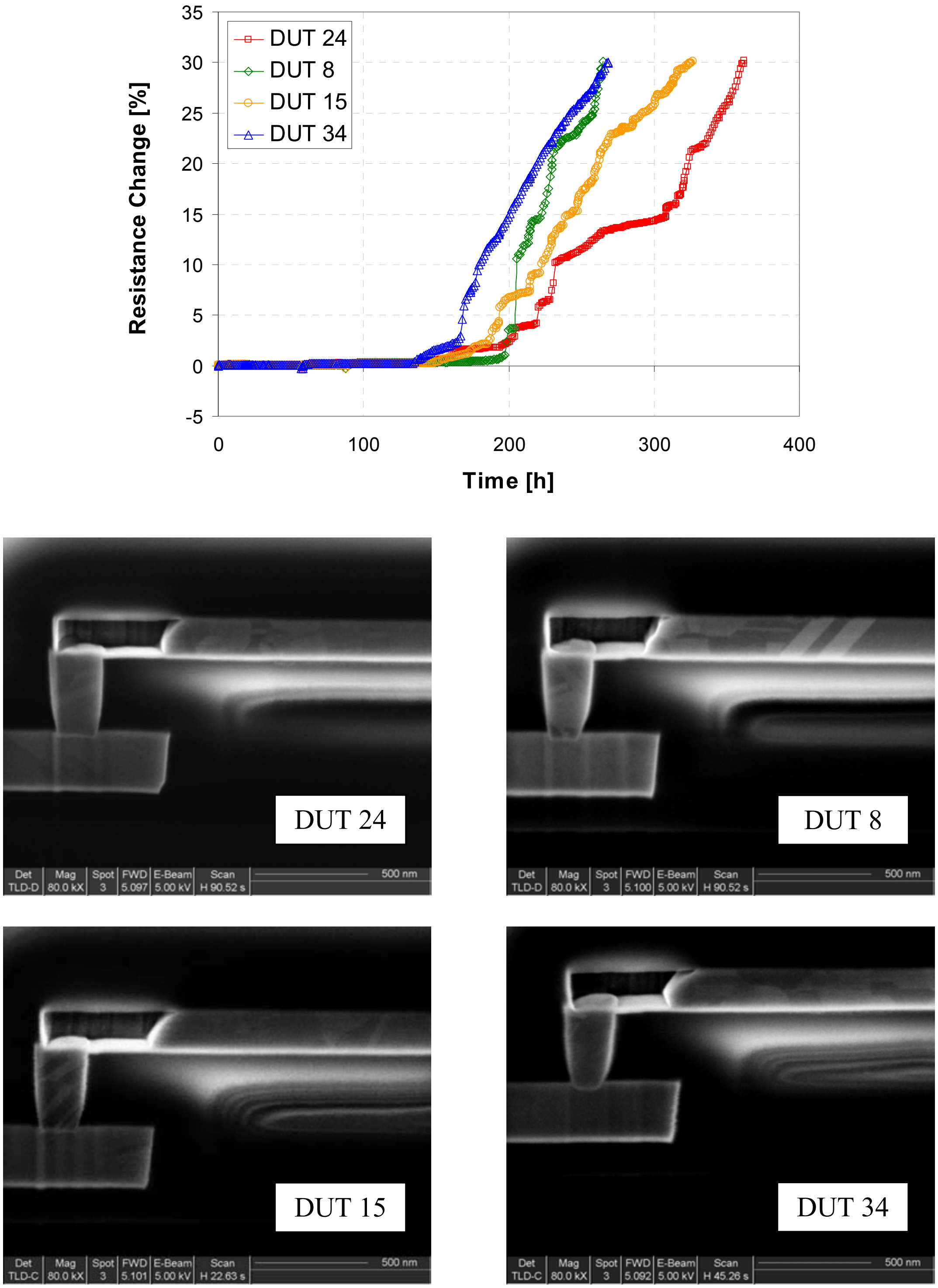

Figure 6.6 Resistance traces and corresponding SEM images for selected reduced height samples tested to a 30% resistance increase.

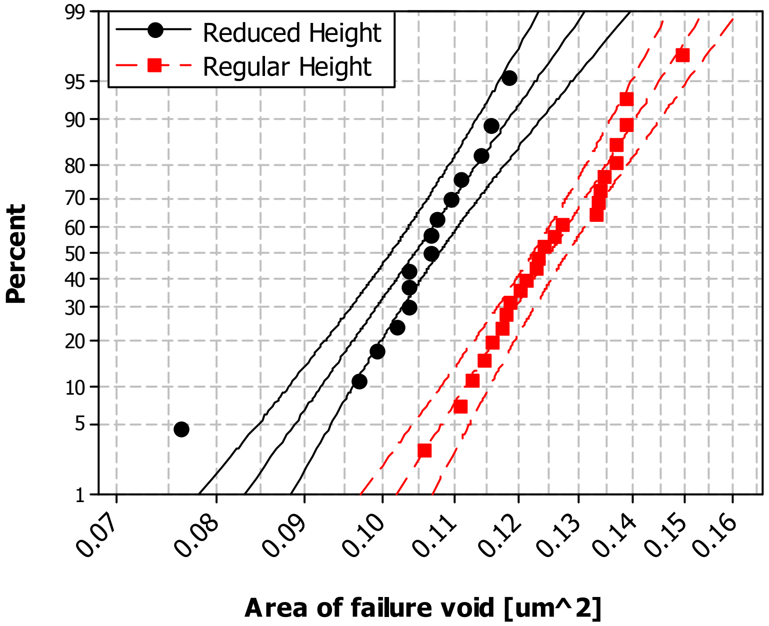

Figure 6.7 Distributions of the void area corresponding to the failure void for reduced and regular height samples tested to 30% resistance increase.

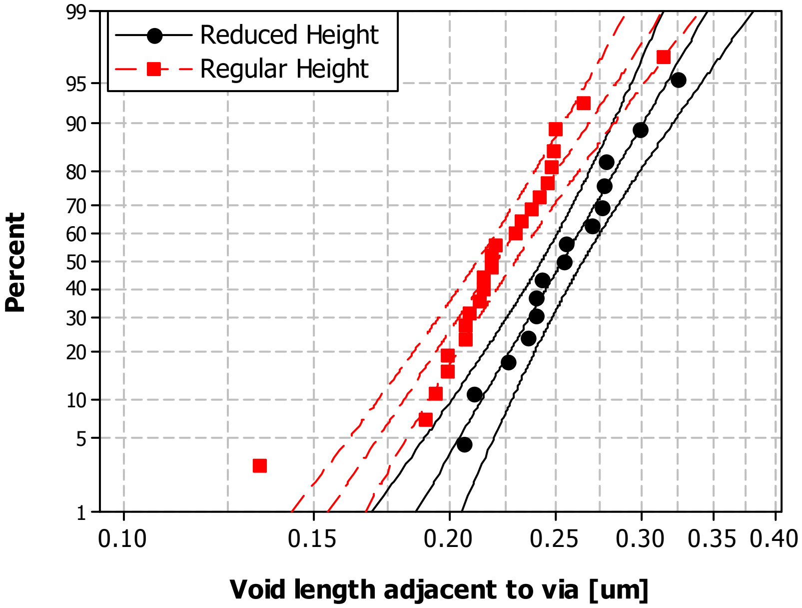

Figure 6.8 Distributions of the void length adjacent to the via for reduced and regular height samples tested to 30% resistance increase.

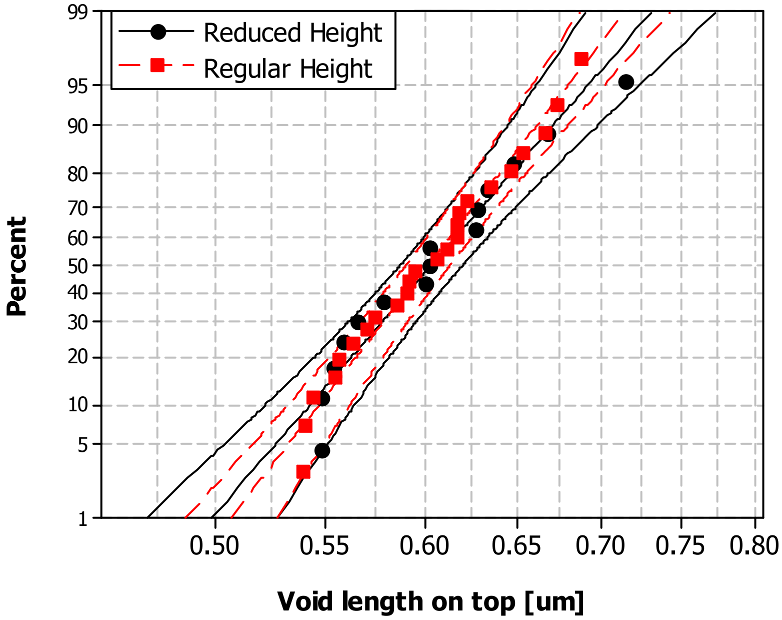

Figure 6.9 Distributions of the void length on top of the interconnect for reduced and regular height samples tested to 30% resistance increase.

Table 6.4 Statistics of void dimensions for reduced height samples. 15 samples were measured. The mean and sigma values of the void area are measured in µm^2, whereas the lengths measurements are in µm.

Reduced Height Samples	Median	Lower Median	Upper Median	Sigma	Lower Sigma	Upper Sigma
Failure Void Area	0.104	0.101	0.108	0.098	0.078	0.123
Void Length (adjacent to via)	0.254	0.243	0.265	0.133	0.102	0.175
Void Length (top)	0.604	0.587	0.620	0.082	0.063	0.107

Table 6.5 Statistics of void dimensions for regular height samples. 24 samples were measured. The mean and sigma values of the void area are measured in µm^2, whereas the lengths measurements are in µm.

RegularHeight Samples	Median	Lower Median	Upper Median	Sigma	Lower Sigma	Upper Sigma
Failure Void Area	0.125	0.122	0.128	0.089	0.072	0.109
Void Length (adjacent to via)	0.221	0.212	0.230	0.153	0.127	0.184
Void Length (top)	0.602	0.590	0.613	0.074	0.060	0.090

The reason for the similarity of the void length values on top of the interconnect is schematically illustrated in Figure 6.10. The void inclination region, part 3 of the total void area as defined in Chapter 5, simply extends less in samples with reduced line height compensating for the larger void length adjacent to the via on the bottom of the line. A simple calculation can be performed to support the experimental data using only the mean values of geometric parameters instead of the entire statistical data set. First, the values of the void lengths adjacent to the via, labeled Δl in Figure 6.10, can be obtained as mentioned in the previous paragraph. Table 6.6 contains the calculated values for the reduced and regular height samples showing good agreement to the measured values listed in Tables 6.4 and 6.5. A smaller value for the baseline samples is clearly observed. When examining the void inclination angles of both sets of samples, the dimension l' in Figure 6.10 can be calculated using basic trigonometry and the mean values of the measured line heights of the corresponding samples. The distribution of void inclination angles is shown in Figure 6.11 comparing the reduced line height data with the baseline. No statistically significant difference can be observed. Thus, a median inclination angle of about 56° has been used for the calculation of l'. Results for both data sets are included in Table 6.6. The sum of the calculated values for Δl and l' for each data set are shown in the fourth column of Table 6.6. It can be seen that the obtained values are comparable. The total void length on top can now be calculated by adding the via length. A mean via length of approximately 0.21μm was assumed for both sample sets. Again, the calculated values are included in Table 6.6. They show excellent agreement with the measured values of the top void lengths in both cases. The implication of this result on the EM lifetime statistics will be discussed further in a later paragraph.

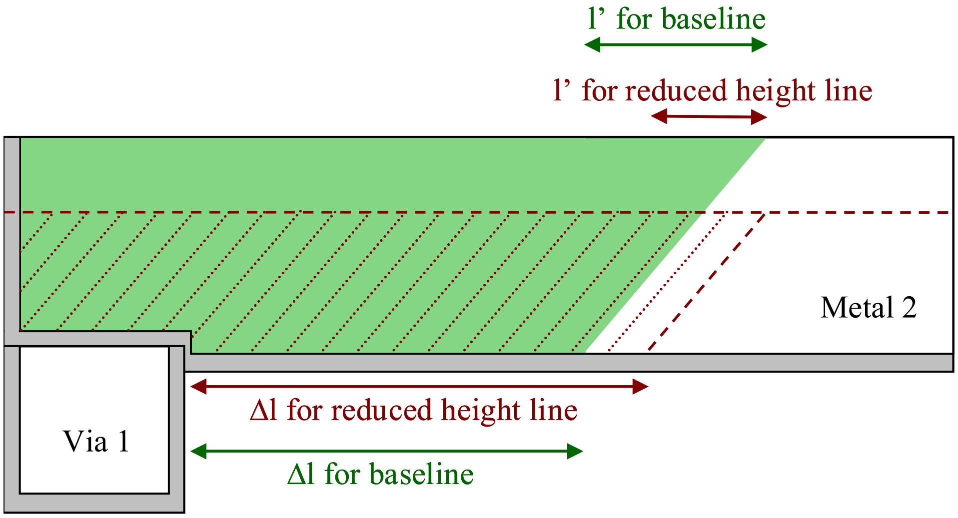

Figure 6.10 Schematic illustrating the effect of reduced line height on void dimensions. *Δl* denotes the void length adjacent to the via at the bottom of the interconnect, while *l'* represents the part of the void length on top of the void induced by the inclination angle.

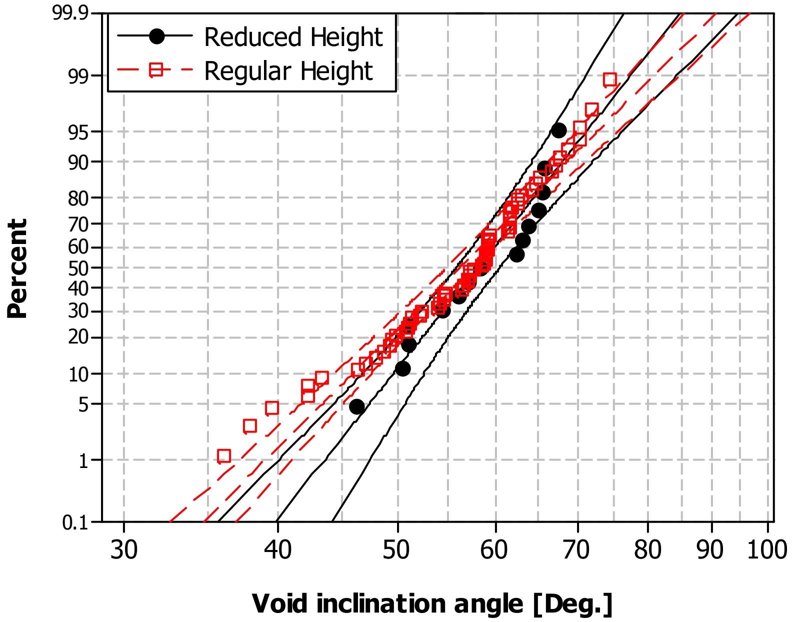

Figure 6.11 Distributions of void inclination angles for reduced and regular height samples.

Table 6.6 Results of the calculation of void dimensions for regular and reduced height samples using the geometrical model in Chapter 5.3. Δl and l' denote the void length adjacent to the via at the bottom of the trench and the part of the void length on top of the void induced by the inclination angle, respectively. A constant via length of 0.21μm was assumed. All values are in μm.

	Δl	l'	$\Delta l+l'$	Void length on top ($\Delta l+l'$+via length)
Reduced Height	0.257	0.137	0.394	0.604
Regular Height	0.219	0.174	0.392	0.602

The calculation can now be extended to obtain the void area statistics for the reduced height samples. Using the observed statistical variations for Cu and Ta cross-sectional areas and void inclination angles, the void area statistics can be calculated following the geometrical model in Chapter 5.3. Since the procedure has been examined in detail in Chapter 5.3, only the results of the calculation will be mentioned here. Good agreement between experiment and simulation was obtained for both the median void area as well as the sigma value. The concurrence of the sigma values of experiment and calculation is expected for the reduced line height data, since the sigma values of the input parameters were similar for reduced and regular height samples, and the latter showed good agreement already.

Using the results of the above discussion, the observation that the sigma values of EM lifetime distributions are similar for reduced and regular height samples can be easily understood. In Chapter 5, it has been argued that the EM lifetime statistics depend on variations in void areas and Cu cross-sectional areas, the distribution of temperature in the EM oven as well as mass transport variations. The statistics of void area and Cu cross-sectional area have been examined above appearing to be comparable for reduced and regular height samples. Obviously, the temperature variation in the EM oven is identical for both data sets. Furthermore, the fact that the median top void length for the same resistance increase failure criterion is similar for both types of samples indicates that the effective diffusion path is comparable. The microstructure in both sets of lines is expected to be identical, since it was defined prior to the CMP step. Hence, the grain area distribution at the top of the line is anticipated to be similar, influencing the mass transport alike in both sample types. As a consequence, the diffusivity variations are expected to show comparable statistics. Therefore, all the parameters which are believed to significantly contribute to variations in EM lifetimes, as examined in Chapter 5, appear to have comparable statistics for reduced and regular height samples. As a result, the observed similarities in sigma values of EM lifetime distributions can be explained.

This result provides support for the applicability of the model developed in Chapter 5 to explain EM lifetime statistics. It appears to explain the observed lifetime characteristics well for both regular and reduced height samples. An important conclusion from this experiment is the fact that the volume which is being removed during the EM experiment does not appear to influence the variations in EM lifetimes significantly. While the need to remove a smaller Cu volume led to the reduction of the median lifetime for the reduced line height samples, the sigma value was not affected. This observation supports the result of Chapter 5 that the influence of microstructure on EM lifetimes is related to the grain area distribution along the diffusion path, but not to the volume or number of grains which need to be removed.

6.2 INFLUENCE OF PASSIVATION LAYER

In the second study conducted to examine process effects on the EM lifetime statistics, the behavior of samples coated with SiC instead of SiN_x were examined. These samples, also taken from lot D76814, had identical line dimensions as the baseline SiN_x samples. EM tests were performed on identical structures under the same temperature and current stressing conditions. EM lifetime distributions comparing the SiC coated samples with SiN_x capped test structures are shown in Figure 6.12. As in the case of thinner metal trenches discussed above, a 10% resistance increase failure criterion is used. The median lifetime of the SiC samples is significantly smaller compared to the baseline samples, with the latter failing about 12 times later. The sigma values are 0.32±0.09 for SiC and 0.24±0.01 for SiN_x. Due to the fact that the SiC experiment was conducted with only 23 samples, the error bars for the sigma value of this distribution are relatively large. Thus, within the statistical confidence limits, the sigma values appear to be identical.

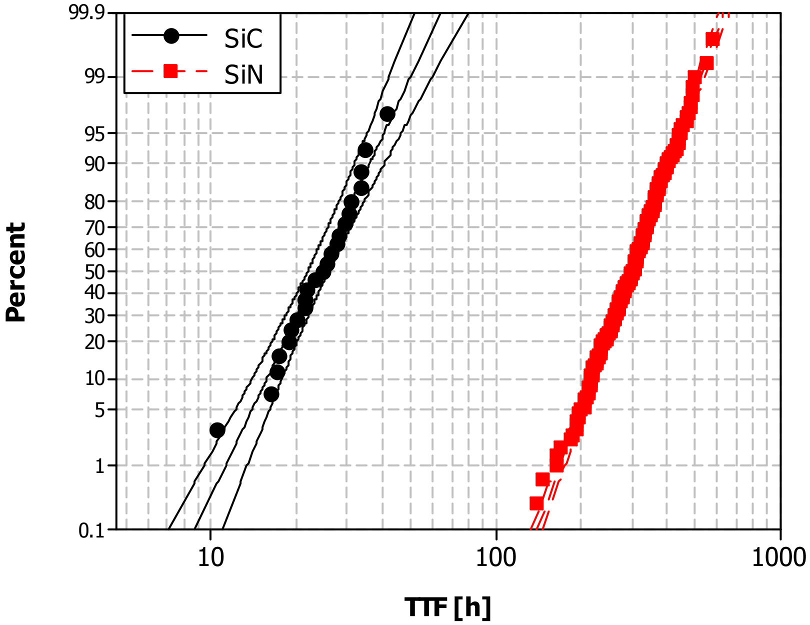

Figure 6.12 EM lifetime distributions for the SiC and SiN_x capped samples corresponding to a 10% resistance increase failure criterion.

Lane *et al.* [2003] reported as well that the median lifetime is significantly reduced for SiC coated samples compared to SiN. Furthermore, they observed a reduction in interfacial debond energy by about 40% for the SiC capped samples. Hence, the interfacial properties, such as bond character or purity, appear to be significantly worse allowing for an increase in mass transport along that interface. As a consequence, the time to EM failure is shortened.

The EM mechanism is expected to be identical in SiC and SiN_x capped samples, since in both cases the interface appears to be the fastest diffusion path. Hence, the model developed in Chapter 5 linking the EM failure statistics to experimental, process and mass transport variations should be applicable here. As mentioned above, the target line dimensions for SiC and baseline samples are identical. Thus, their variations can be assumed to be comparable leading to similar statistics for Cu cross-sectional area as well as void size distributions. Obviously, the temperature variation in the EM oven is the same for all samples. From Equation (5.14), the variation in diffusivities between different lines under test remains to be examined. As already mentioned, the mean value of the interface diffusivity is significantly larger in SiC coated samples compared to the baseline. However, the variation in diffusivity at the cathode ends of lines is a result of the microstructure. The grain size as well as orientation distributions in both sets of samples are expected to be comparable, since the same processing procedure was used to create the trenches. Furthermore, due to identical line dimensions, similar void lengths are anticipated for SiC and SiN_x capped samples. Thus, the effective diffusion paths influencing the EM lifetime behavior at a certain resistance increase failure criterion should be alike. Hence, the variation in diffusivity at the cathode end is expected to be comparable. Henceforth, it seems that the statistics of all parameters identified as influencing EM characteristics are similar for SiC and SiN_x coated samples, explaining the comparable sigma values observed for the EM lifetime distributions of both data sets. Similar to the conclusion of the study of reduced line height samples, this result provides support for the applicability of the proposed model to adequately describe EM statistics for interconnects failing by the EM mechanism described in this work.

As mentioned in the introduction as well as the background chapter, a variety of studies focus on improving the top interface to reduce EM-induced mass flux. [Hu 2002, Hu 2003a, Hu 2003b, Hu 2004, Zschech 2004, Meyer 2004]. The major focus of these studies is the effect of an interface change on the EM mass transport mechanism. However, Hu *et al.* indicated that the sigma value increases significantly with the use of a CoWP cap layer instead of the SiN_x over-coat. This observation deserves some attention, especially since an increase in sigma counteracts an increase in lifetime when extrapolating to operating conditions. Obviously, depending on their absolute values, this effect might be tolerable. It needs to be mentioned here that the mass transport mechanism under EM in interface-strengthened samples appears to be different than the SiN_x capped samples analyzed in this study. Zschech *et al.* [2004] and Meyer *et al.* [2004] observed void formation not only at the top interface, but also along the Cu/barrier layer interface indicating that this interface is now as well an active diffusion path. The mixture of diffusion paths and the distribution of void formation sites, as well as final failure void locations, need to be examined carefully with respect to their influence on the EM lifetime statistics. When multiple failure mechanisms are active, the EM failure distributions are expected to broaden, leading to a higher sigma and worse extrapolations to very small failure percentiles. This effect has to be outweighed by a significant increase in lifetimes, as mentioned above.

6.3 COMPARISON OF SINGLE AND DUAL DAMASCENE STRUCTURES

In this section, the influence of a dual damascene (DD) process scheme on the EM lifetime statistics will be examined and compared to the effect of the single damascene (SD) integration discussed in the major part of this study. As indicated in Chapter 2, the DD technology is preferred by industry due to a reduction in processing steps, leading to faster turnaround time and improved cost.

Samples were prepared as indicated in Chapters 2 and 3. The materials as well as line dimensions were similar to the baseline SD samples, i.e. the target line height is 0.3μm and the cap layer is SiN_x. Likewise, the EM tests were conducted under identical conditions with 300°C as the target temperature and an approximate current density of $1.5MA/cm^2$. Samples were taken from lots D67250, D67667 and D67654, which all show comparable EM behavior.

The resistance traces of several DD samples tested to a 100% resistance increase failure criterion are shown in Figure 6.13. Comparing this plot with Figure 4.1, which displayed the resistance change over time for selected SD samples, no obvious differences can be discerned. Initially, the resistance decreases slightly, followed by a period of slight increase and a jump in resistance of a few percent. Subsequently, the resistance increases approximately linearly with time.

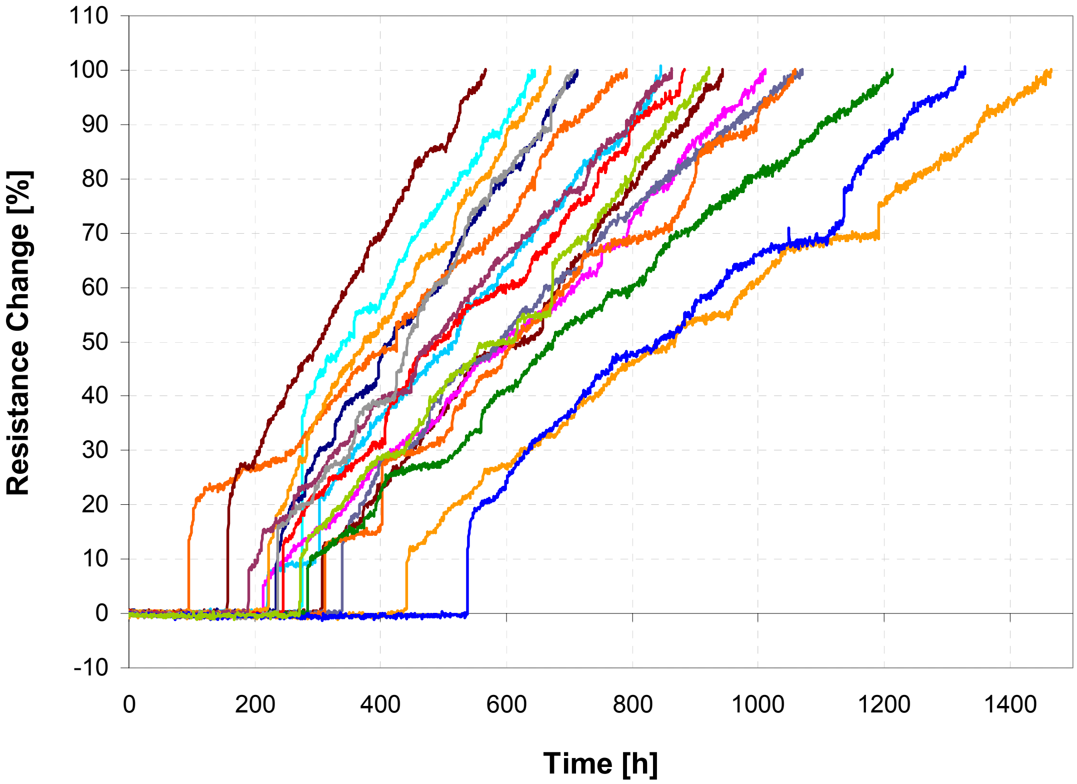

Figure 6.13 The resistance change of DD samples as a function of time as measured during an EM test.

EM lifetime distributions of DD and SD samples for a 10% resistance increase failure criterion are compared in Figure 6.14. The median lifetimes seem to be similar. However, a direct comparison of the median lifetimes needs to be treated with caution as slight processing variations could influence the median times. As pointed out previously, the SD samples are all taken from lots with comparable EM behavior. While the three lots used to obtain the DD samples all show similar EM behavior, it is still not necessarily directly comparable to the SD samples, since processing was not performed at the same time. Furthermore, Figure 6.14 seems to indicate that the distribution corresponding to DD samples deviates from the straight line in the lognormal plot for small percentage values suggesting an early failure population of about 6%. These data points are most likely due to void formation in the via, which requires only a small void to fail the line as discussed in several publications [for instance: Ogawa 2001, Ogawa 2002a, Gill 2002, Lai 2001]. However, they prohibit fitting a monomodal distribution to the measured data to obtain the median and sigma values.

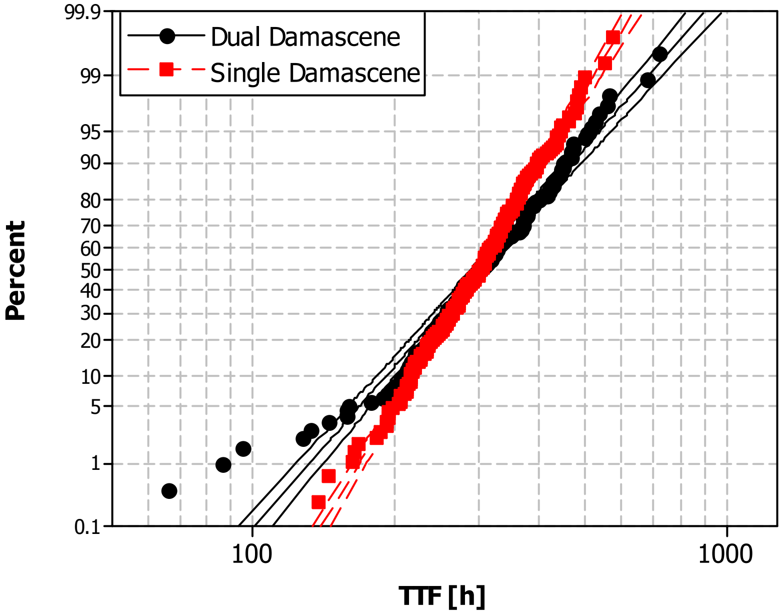

Figure 6.14 EM lifetime distributions for dual and single damascene samples corresponding to a 10% resistance increase failure criterion.

Figure 6.15 displays the EM lifetime distributions of DD samples as a function of resistance increase failure criterion. Similar to the SD samples, an increase in median time-to-failure can be observed with increasing resistance increase failure criterion. However, a clear trend in sigma values comparable to the trend in SD structures is not obvious. Due to the early failures, it is more difficult to quantify the magnitude of the lifetime variation. Results for sigma as a function of median lifetime using a monomodal lognormal fit to the experimental data are included in Figure 6.16 together with the results for SD interconnects. A slight trend of decreasing sigma with increasing time might be discerned, however a significantly larger samples size is needed to draw a more definite conclusion. Furthermore, it needs to be kept in mind that a monomodal distribution fit is not an accurate representation of the data. Since this study is mainly concerned with the major part of the failure population, the data points below about 6% have been removed in order to obtain sigma values of the remaining data points. Figure 6.17 shows the EM lifetime distributions without the early failures. Again, no clear trend of sigma values as a function of the resistance increase failure criterion can be observed. The evolution of sigma as a function of median time-to-failure is included in Figure 6.16 supporting this observation. It is important to mention that it is possible that a similar trend as observed for SD samples could exist in DD samples, however the number of data points might need to be increased significantly to be able to observe it. Interestingly, the sigma values of DD samples are consistently higher than the SD values.

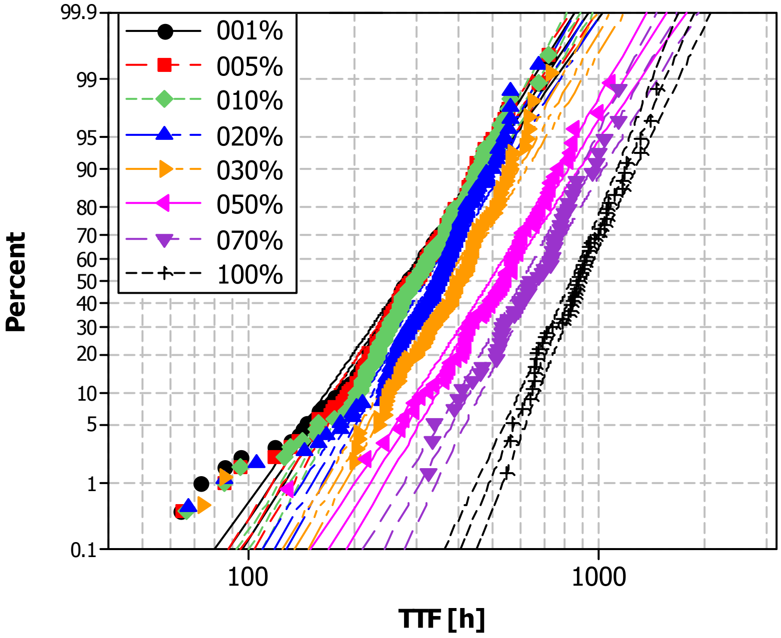

Figure 6.15 EM lifetime distributions of dual damascene samples as a function of resistance increase.

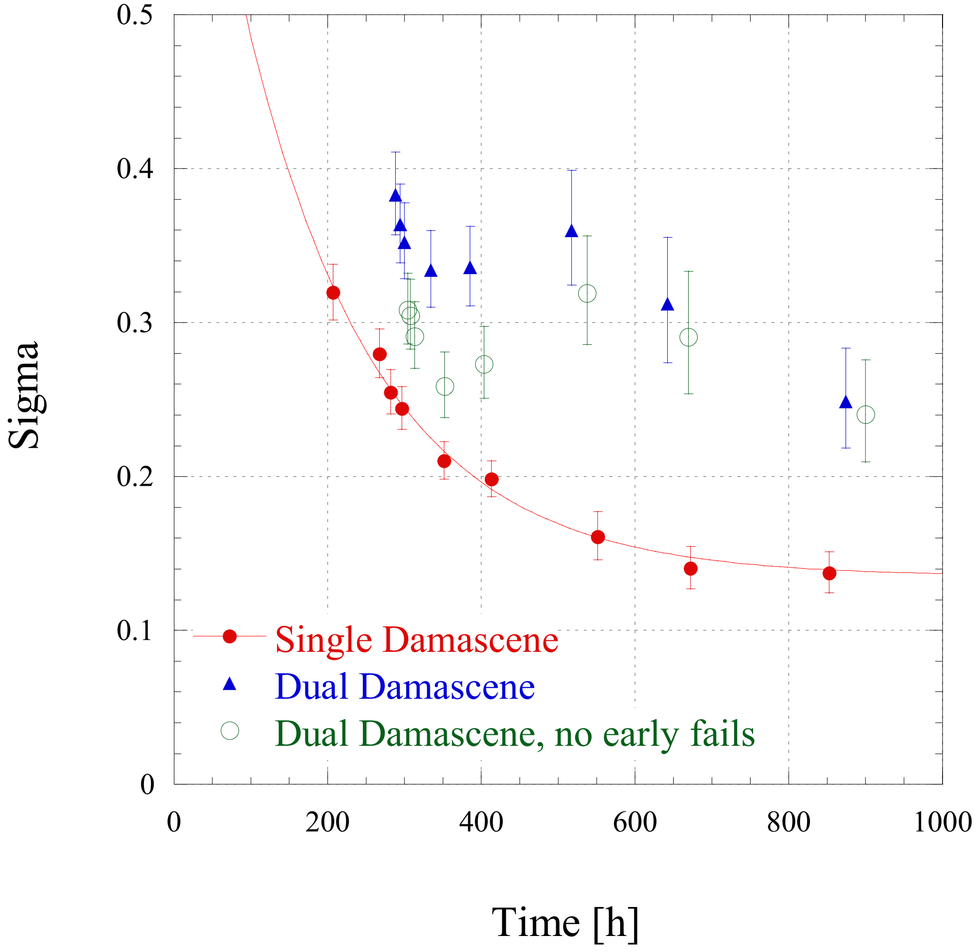

Figure 6.16 Sigma as a function of median time to failure for EM lifetime distributions of single and dual damascene structures. In the case of dual damascene, two data sets are shown. One set includes all data points, while the early failures were removed for the other.

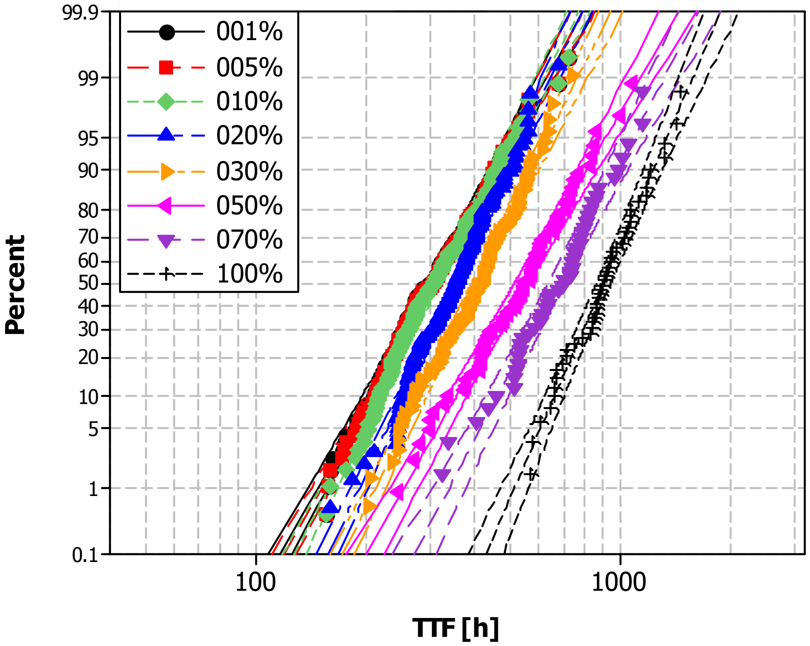

Figure 6.17 EM lifetime distributions of dual damascene samples as a function of resistance increase without early failures.

This observation can be understood when examining the void evolution behavior in DD samples in more detail. Akin to the work on SD structures, FIB cross-sectioning was performed on samples tested for only short times to examine the void evolution behavior prior to any resistance increase. The void evolution behavior appears to be quite similar to the SD case, i.e. the voids form at the interface, evolve at the interface towards the cathode end and finally grow along the line. Thus, the four stages of void evolution as described in Chapter 4 are also occurring. Figure 6.18 shows several SEM images corresponding to stages 1 and 2 of void evolution. Voids seem to form at the top interface at intersections of grain boundaries with the interface statistically distributed away from the cathode end. Subsequently, the initial voids refill and the voids evolve towards the cathode end. Even though several samples were examined, no void formation in the via was observed. However, as seen above, only about 6% of the DD population seems to be susceptible to early failure. Thus, quite a large number of samples need to be examined to observe via failures in their early stages, i.e. before they cause a resistance increase. Figure 6.19 shows SEM images of samples which just passed the first resistance increase. The images are comparable to the ones for SD samples shown in Figures 4.11-4.13. The voids led to a significant reduction in Cu cross-sectional area, forcing the current through a rather small area. The last stage of void evolution is depicted in Figure 6.20. This last stage appears to show some differences between SD and DD structures. Some images in Figure 6.20 show that the void has grown along the line staying completely above the via, identical to the SD case, whereas in most other images the void has grown into the via, as well as along the line. Various stages of void growth into the via can be observed in the images.

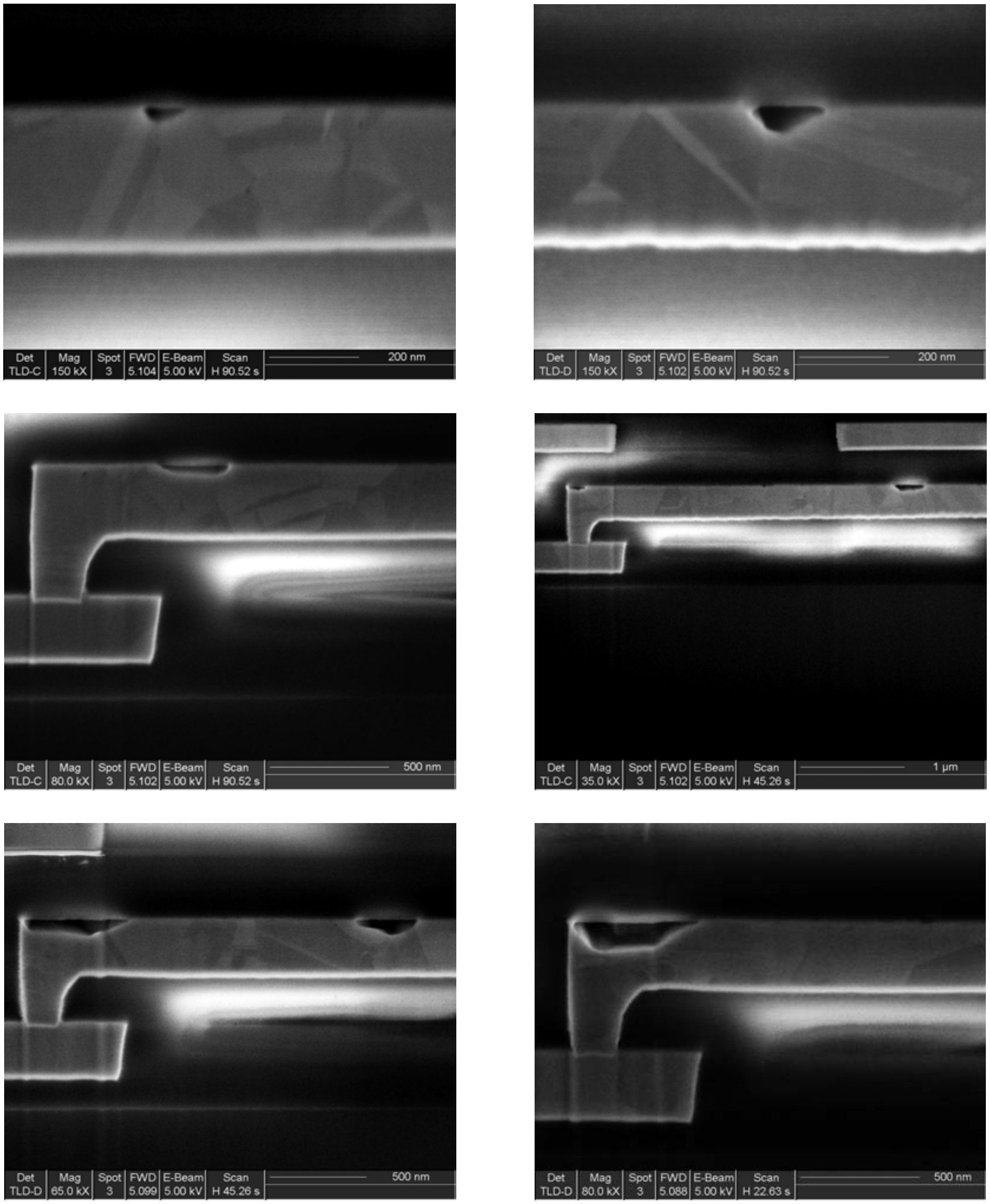

Figure 6.18 SEM images showing stages 1 and 2 of the void evolution process. Voids initially appear to form at the top of the trench at intersections of grain boundaries with the interface. Subsequently, they evolve towards the cathode end.

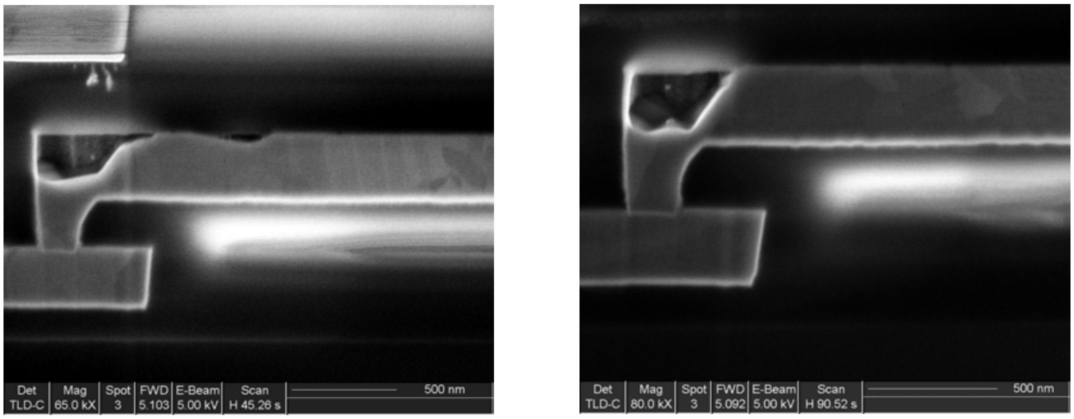

Figure 6.19 SEM images showing stage 3 of the void evolution process. The Cu cross-sectional area is being reduced to the extent that the resistance increases.

The described void evolution behavior is slightly different than the one observed by Meyer *et al.* [2002] and Zschech *et al.* [2004]. The void evolution corresponding to stages 1 and 2 has been observed to be mostly identical. However, while it seems that a significant percentage of samples examined in this study grow only slightly into the via, but mainly along the line, their samples show most voids to grow significantly into the via even removing Cu from the bottom of the via. Thus, the line fails by a sudden open caused by a void at the via bottom. It appears that the barrier layer in the via is too thin to serve as a redundant diffusion path for the high current density used in their study. Since their work is performed in-situ in an SEM, a high current density between 10 and 20MA/cm^2 was used to render the tests feasible. This is approximately 7-13 times larger than the current density used in this work. The high value of current density might be the cause of the indicated differences in void evolution.

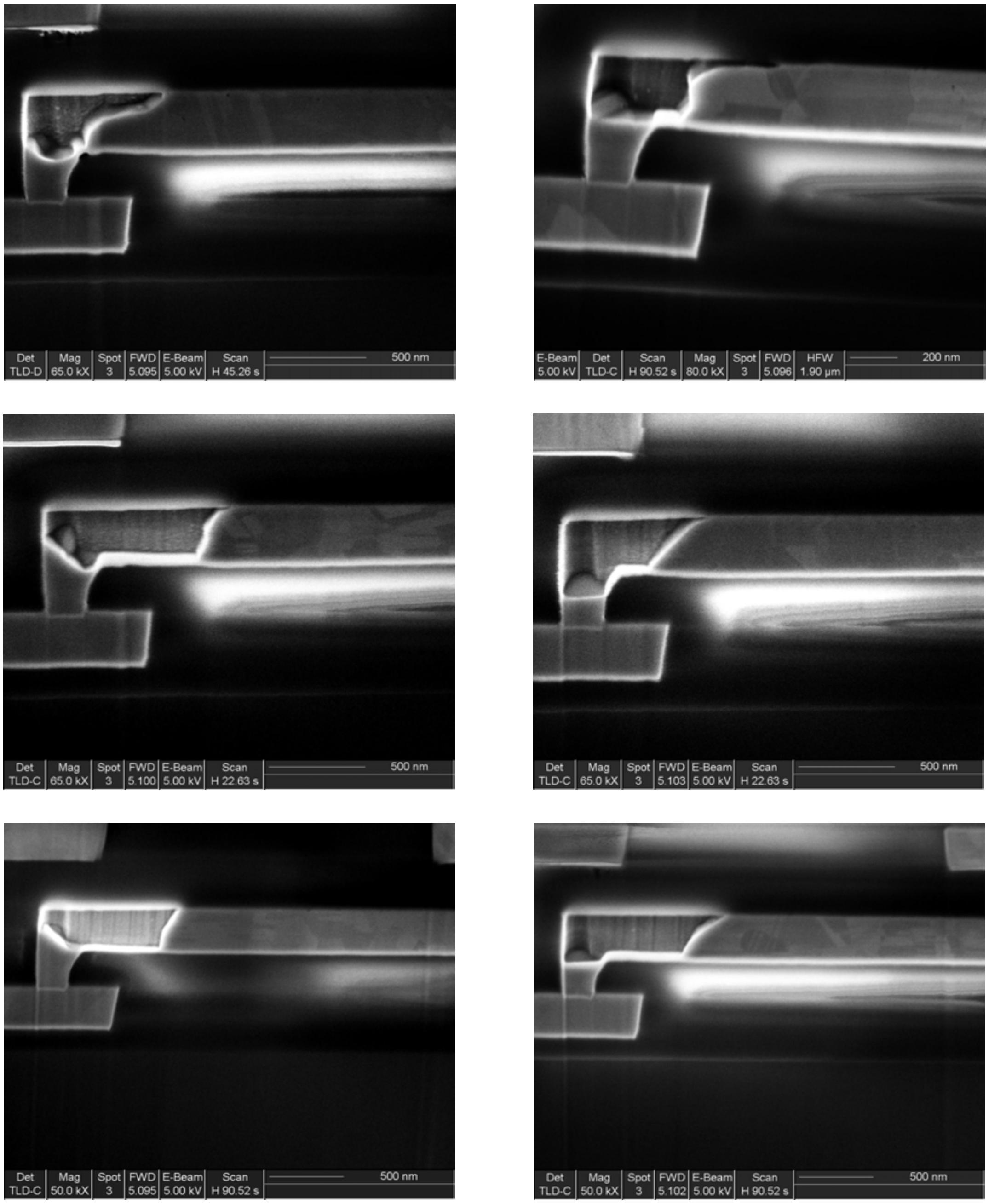

Figure 6.20 SEM images showing stage 4 of the void evolution process. The first two images correspond to a 10% resistance increase (left) and a 300h test (right). The bottom 4 images display voids, which caused a 50% resistance change.

The possibility of the void growing into the via is expected to increase the sigma value of the void size distribution. For two selected test conditions, namely a 300h test and a 50% resistance increase experiment, a larger number of void areas was measured to examine their statistics. The void area distributions are both included in the plot in Figure 6.21. The sigma values are 0.279 and 0.141 for the 300h and the 50% samples, respectively. Both values are significantly larger compared to the corresponding values for SD samples, which are 0.169 and 0.061 for the 300h and 50% experiments, respectively. This observation can be explained by the increase in possible void shapes and sizes when the void is able to grow into the via, in addition to evolving along the line. This result highlights certain limits of the model developed in Chapter 5. The geometrical model used to simulate the void size variations in SD samples as described in Chapter 5.3 is not directly applicable any longer. It needs modification which includes the void growth into the via.

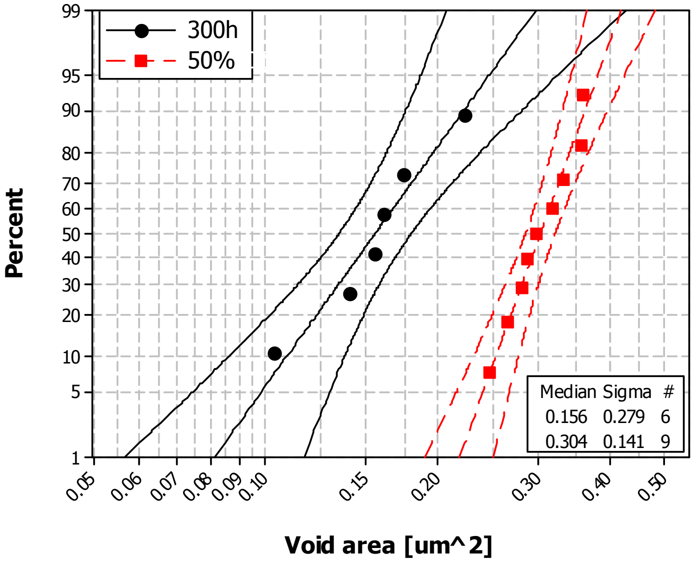

Figure 6.21 Void area distributions of dual damascene samples EM-tested for 300h or until 50% resistance change was observed.

Following this discussion, the observed larger sigma values of DD EM lifetimes might be attributed to the increase in void size variations. Since only limited void size data is currently available, the applicability and use of Equation (5.14) to describe EM statistics in DD samples will be addressed in a qualitative manner. It appears that the major diffusion mechanism in DD samples is comparable to the SD structures with the major mass transport being along the top interface of the line. Furthermore, for 94% of the population the failure void seems to be at the cathode end of the line with the void partially in the via, but mostly along the line. These observations suggest that Equation (5.14) should be applicable as well in the DD case. Since the line dimensions, metal deposition as well as annealing conditions are comparable between SD and DD samples, the microstructure in the trenches of DD samples is expected to be similar to the SD case. In addition, the void length on top of the line should be reasonably comparable for a certain resistance increase failure criterion. The limited data available for DD samples supports this statement, even though the variation in void length on top of the line appears to be larger, since some voids grow more into the via compared to others, reducing the void length needed for a certain resistance increase. Nevertheless, the diffusivity variation at the cathode end in DD samples might show similar behavior as a function of time as was observed for the SD samples. This statement is only a simplification, since during the void evolution into the via additional diffusion paths might be active, such as grain boundaries. In general, it appears, however, that the variations in Cu cross-sectional area, temperature and mass transport are comparable for DD and SD samples. Only the void size distributions appear to show significant differences, with the sigma value of the void areas of 50% DD samples about twice as large as the corresponding SD value. The sigma value of the 50% EM lifetime distribution of DD samples is also approximately twice as large as the SD value. Thus, the increased sigma values can be qualitatively attributed to the larger variation in void sizes as a result of voids being able to grow into the via, in addition to growing along the line.

Obviously, a more detailed quantitative analysis of the void size statistics of several EM test conditions remains to be done, as well as an improved analysis of active diffusion paths. However, the basic statistical EM behavior of DD samples examined in this study appears to be qualitatively understood.

Chapter 7: Conclusions and Suggestions for Future Work

The statistical details of EM lifetimes and of the corresponding void evolution in single damascene 0.18μm Cu interconnects were analyzed and the causes for the variations in lifetimes and void dimensions were identified within the course of this study. The sigma values of EM lifetime distributions were found to depend on the failure criterion used, showing a significant decrease with increasing resistance failure criterion. For long times, sigma appeared to have an asymptotic behavior with a minimum value of about 0.14. The corresponding void evolution was separated into four stages, namely void formation at the top interface, void evolution along the interface towards the cathode end of the line, first resistance increase and subsequent void growth along the line accompanied by a steady resistance change. The void sizes for various EM testing conditions were examined. The average void growth behavior was found to be linear in time. However, significant variations in void sizes were observed within each experiment. Similar to the trend in EM sigma values, the variations in time-based and resistance-based void size distributions showed a decrease with increasing test time or resistance change. Furthermore, the sigma values of resistance-based void size distributions were significantly smaller compared to the time-based case.

It was shown that the statistics of EM lifetime distributions can be adequately modeled by combining the time-based and resistance-based void area measurements. The characteristics of the latter depend on geometrical factors, while void size distributions from time-based tests depend on geometry as well as kinetics. A model was applied to simulate their statistics, including geometrical and experimental factors of the EM test, as well as kinetic aspects of the mass transport process such as differences in interface diffusivity between the lines. The variation in diffusivities at the cathode ends of the lines arises from differences in the interface structure as a result of varying Cu grain orientations. As a result, the parameters defining EM lifetime statistics were identified as variations in void sizes, experimental factors such as temperature variations in the EM oven, process parameters, which induce line dimension variations, and mass transport variations. An influence of microstructure in the Cu lines on EM lifetime variations was established, since the mass transport under EM seems to depend on individual grain interfaces and their diffusivities. The decrease in sigma with increasing resistance failure criterion was correlated to a reduction in variations in void sizes and effective diffusivities. While the former was attributed to geometrical factors, the latter is a consequence of an averaging over a larger number of grain interfaces. The combined effect adequately reproduced the trend in sigma values of EM lifetime distributions.

This study allows an estimate of the EM statistics in future interconnect generations. Understanding the origin of the lognormal sigma for a certain process technology and design enables the prediction of the expected sigma value for smaller and smaller interconnect lines. In the case that the EM mechanism is identical or similar to the one described in this study, i.e. the top interface is the major diffusion path and the final failure voids are at the cathode end above the via, the parameters influencing EM characteristics remain the same as identified in this work. Thus, by assessing their statistics as a function of technology generation, the EM lifetime statistics can be predicted.

Additional experiments were conducted to test the validity of the model developed in this study. Line thickness variation and a change in the dielectric capping layer from SiN_x to SiC left the sigma of the EM lifetime distribution virtually unchanged. Both observations were explained using the model developed in this study. The change from a single to a dual damascene processing scheme induced a significant increase in the observed sigma values. This result correlated with an increase in void size variations. Void growth into the via as well as along the line extends the possibilities of void shapes and sizes leading to identical resistance increase values. As a consequence, EM lifetime distributions are not as well controlled and a trend of decreasing sigma with increasing resistance criterion is not clearly observable. While the kinetic aspects of the model most likely remain unchanged, the geometrical analysis developed for single damascene structures cannot be applied to a dual damascene integration. A more complex model needs to be established, assessing the interaction of void growth into the via and along the line.

Future work needs to focus on the effect of new processing schemes on the EM statistics. As mentioned previously, possible new technologies could lead to significant strengthening of the top interface. Such efforts include the insertion of a thin layer of selectively deposited material between Cu and the passivation layer as well as alloying Cu with small percentages of adequate solutes. While lifetimes may improve considerably, the sigma value may deteriorate. This possibility deserves attention, especially since an increase in sigma counteracts an increase in lifetime when extrapolating to operating conditions. Obviously, depending on their absolute values, this effect might be tolerable. A possible reason for the deterioration in sigma of interface-strengthened samples might be a change in the EM mass transport mechanism compared to the SiN_x capped samples analyzed in this study. As a result, the void formation and evolution processes might alter considerably. The mixture of diffusion paths and the distribution of void formation sites, as well as final failure void locations, need to be examined carefully with respect to their influence on the EM lifetime statistics. When multiple failure mechanisms are active, the EM failure distributions are expected to broaden, leading to a higher sigma. In this case, the model describing EM lifetime statistics will have to be altered to capture the new mass transport mechanisms.

References

Arnaud L., Tartavel G., Berger T., Mariolle D., Gobil Y., Touet I., *Microelectronics Reliability* **40**, 77-86, (2000).

Arnaud L., Berger T., Reimbold G., *J. Appl. Phys.* **93** (1), 192-204, (2003).

Atakov E.M., Clement J.J., Miner B., *Proceedings of Int. Rel. Phys. Symp.*, 213-224, (1994).

Attardo M.J., Rosenberg R., *J. Appl. Phys.* **41** (6), 2381-2386, (1970).

Besser P.R., Zschech E., Blum W., Winter D., Ortega R., Rose S., Herrick M., Gall M., Thrasher S., Tiner M., Baker B., Braeckelmann G., Zhao L., Simpson C., Capasso C., Kawasaki H., Weitzman E., *J. Elec. Mat.* **30** (4), 320-330, (2001).

Black J., *IEEE Trans. Electron. Devices*, **ED-16**, 338, (1969).

Blech I.A., Meieran E.S., *Appl. Phys. Lett.*, **11** (8), 263-266, (1967).

Blech I.A., *J. Appl. Phys.* **47** (4), 1203-1208, (1976).

Buerke A., Wendrock H., Koetter T., Menzel S., Wetzig K., v. Glasow A., *Proc. Mat. Res. Symp.*, **563,** 109-114, (1999).

Demuynck S., Tokei Zs., Bruynseraede C., Michelon J., Maex K., *Proc. of Advanced Metallization Conference*, 355-359, (2003).

d'Heurle F.M., Ho P.S., in *Thin Films: Interdiffusion and Reactions*, J. Poate, K.N. Tu, J.B. Mayer, Eds: John Wiley, **Ch. 8**, 243-303, (1978).

Donohue H., Yeoh J.C., Giles K., Buchanan K., *Microelectronics Engineering*, **64**, 299-305, (2002).

Dwyer V.M., *J. Phys. D: Appl. Phys.*, **37**, 2035-2046, (2004).

Edelstein D., Heidenreich J., Goldblatt R., Cote W., Uzoh C., Lustig N., Roper P., McDevitt T., Motsiff W., Simon A., Dukovic J., Wachnik R., Rathore H., Schulz R., Su L., Luce S., Slattery J., *Proceedings of the International Electronics Devices Meeting*, 773-776, (IEEE, Washington, 1997)

Edelstein D., Uzoh C., Cabral C., DeHaven P., Buchwalter P., Simon A., Cooney E., Malhotra S., Klaus D., Rathore H., Agarwala B., Nguyen D., *Proceedings IEEE Int. Interconnect Technology Conf.*, 9-11, (2001).

Fayad W., Thompson C.V., Frost H.J., *Scripta Materialia*, **40** (10),1199-1204, (1999).

Fayad W.R., Andleigh V.K., Thompson C.V., *J. Mater. Res.*, **16** (2), 413-416, (2001).

FEI Company, 5350 NE Dawson Creek Drive, Hillsboro Oregon 97124, USA, *www.feicompany.com*.

Gall M., *Ph.D. Dissertation*, The University of Texas at Austin, 1999.

Gall M., *J. Appl. Phys*, 90 (2), 732-740, (2001).

Gill J., Sullivan T., Yankee S., Barth H., v. Glasow A., *Proceedings of Int. Rel. Phys. Symp.*, 298-304, (2002).

Hasunuma M., Toyoda H., Kaneko H., *Microelectronics Reliability*, **39** , 1631-1645, (1999).

Hau-Riege C.S., Thompson C.V., *Appl. Phys. Lett.* **78** (22), 3451-3453, (2001).

Hauschildt M., Toyoda H., Ho P.S., unpublished research, (1998).

Hauschildt M., Edwards G., Gregory R., unpublished research, (2001)

Hauschildt M., Gall M., Thrasher S., Justison P., Michaelson L., Hernandez R., Kawasaki H., Ho P.S., *Proc. of Mater. Research Soc. Symp.*, **812**, 379-384, (2004a).

Hauschildt M., Gall M., Thrasher S., Justison P., Michaelson L., Hernandez R., Kawasaki H., Ho P.S., *AIP Conf. Proc. of Stress Induced Phenomena in Metallization: 7th Int. Workshop*, **741**, 112-123, (2004b).

He J., Xu G., Suo Z., *AIP Conf. Proc. of Stress Induced Phenomena in Metallization: 7th Int. Workshop*, **741**, 15-26, (2004).

Hecker M., Fischer D., Hoffmann V., Engelmann H.-J., Voss A., Mattern N., Wenzel C., Vogt C., Zschech E., *Thin Solid Films*, **414**, 184-191, (2002).

Ho P.S., Kwok T., *Rep. Prog. Phys.* **52**, 301, (1989).

Holloway K., Fryer P.M., Cabral C., Harper J.M.E., Bailey P.J., Kelleher K.H., *J. Appl. Phys*. **71 (11),** 5433-5443, (1992) Hu C.-K., Small M.B., Rodbell K.P., Stanis C., Blauner P., Ho P.S., *Appl. Phys. Lett.*, **62** (9), 1023-1025, (1993a).

Hu C.-K., Small M.B., Rodbell K.P., Stanis C., Mazzeo N., Blauner P., Rosenberg R., Ho P.S., *Proc. Mat. Res. Symp.*, **309,** 111-120, (1993b).

Hu C.-K., Ho P.S., Small M.B., *J. Appl. Phys.* **74**, 969, (1993c).

Hu C.-K., Rosenberg R., Tu K.N., *Proc. of the Second International Workshop on Stress-Induced Phenomena in Metallization*, 195, (1994).

Hu C.-K., Rodbell K.P., Sullivan T.D., Lee K.Y., Bouldin D.P., *IBM J. Res. Develop.*, **39**, 465-497, (1995).

Hu C.-K., Rosenberg R., Rathore H.S., Nguyen D.B., Agarwala B., *Proceedings IEEE Int. Interconnect Technology Conf.*, 267-269, (1999).

Hu C.-K., Gignac L., Rosenberg R., Liniger E., Rubino J., Sambucetti C., Domenicucci A., Chen X., Stamper A.K., *Appl. Phys. Lett.* **81** (10), 1782-1784, (2002).

Hu C.-K., Gignac L., Rosenberg R., Liniger E., Rubino J., Sambucetti C., Stamper A., Domenicucci A., X. Chen, *Microelectronic Engineering* **80**, 406-414, (2003a).

Hu C.-K., Gignac L., Liniger E., Herbst B., Rath D.L., Chen S.T., Kaldor S., Simon A., Tseng W.-T., *Appl. Phys. Lett.* **83** (5), 869-871, (2003b).

Hu C.-K., Canaperi D., Chen S.T, Gignac L.M., Herbst B., Kaldor S., Krishnan M., Liniger E., Rath D.L., Restaino D., Rosenberg R., Rubino J., Seo S.-C., Simon A., Smith S., Tseng W.-T., *Proceedings of Int. Rel. Phys. Symp.*, 222-228, (2004).

International Technology Roadmap for Semiconductors, *www.ITRS.org*, 2004

JEOL USA, Inc., 11 Dearborn Road, Peabody MA 01960, USA, *www.jeol.com*.

Kang H.-K., Cho J.S., Wong S.S., *IEEE Electron. Devices Lett.*, **13**, 448-450, (1992).

Kaur I., Gust W., Eds., *Handbook of Grain and Interphase Boundary Diffusion Data*, (Ziegler Press, Stuttgart, 1989).

Knorr D.B., Rodbell K.P., *Materials Science Forum*, **157-162**, 1435-1442, (1994).

Kolawa E., Chen J.S., Reid J.S., Pokela P.J., Nicolet M.-A., *J. Appl. Phys*. **70 (3),** 1369-1373, (1991).

Korhonen M.A., Boergesen P., Tu K.N., Li C.-Y., *J. Appl. Phys*. **73,** 3790, (1993).

Kurtz K., Carpay F.M.A., *J. Appl. Phys.*, **51** (11), 5725-5744, (1980a).

Kurtz K., Carpay F.M.A., *J. Appl. Phys.*, **51** (11), 5745-5754, (1980b).

Kwon K.-W., *Ph.D. Dissertation*, Stanford, 2000

Lai J.B., Yang J.L., Wang Y.P., Chang S.H., Hwang R.L., Huang Y.S., Hou C.S., *Proceedings of International Symposium on VLSI Technology, Systems, and Applications*, 271-274, (2001).

Lane M.W., Liniger E.G., Lloyd J.R., *J. Appl. Phys.* **93** (3), 1417-1421, (2003).

Lee H.-J., Kwon K.-W., Ryu C., Sinclair R., *Acta Mater.*, **47** (15), 3965-3975, (1999).

Liniger E., Gignac L., Hu C.-K., Kaldor S., *J. Appl. Phys.* **92** (4), 1803-1810, (2002).

Longworth H.P., Thompson C.V., *Appl. Phys. Lett.*, **60** (18), 2219-2221, (1992).

Lloyd J.R., Kitchin J., *J. Appl. Phys*, **69**, 2117, (1991).

MathWorks, Inc., 3 Apple Hill Drive, Natick, MA 01760, USA, *www.mathworks.com*.

Media Cybernetics, Inc., 8484 Georgia Avenue, Suite 200, Silver Spring, MD 20910, USA, *www.mediacy.com*.

Meyer M.A., Herrmann M., Langer E., Zschech E., *Microelectronics Engineering*, **64**, 375, (2002).

Meyer M.A., Grafe M., Engelmann H.J., Zschech E., *Proc. of Materials for Advanced Metallization Conference,* Brussels, (2004).

Nicolet M.-A., *Applied Surface Science* **91**, 269-276, (1995).

Oates A.S., *Proceedings of Int. Rel. Phys. Symp.*, 164-171, (1996).

Oates A.S., *Proceedings of Int. Rel. Phys. Symp.*, 234-236, (1998).

Ogawa E.T., Lee K.-D., Matsuhashi H., Ko K.-S., Justison P.R., Ramamurthi A.N., Bierwag A.J., Ho P.S., Blaschke V.A., Havemann R.H., *Proceedings of Int. Rel. Phys. Symp.*, 341-349, (2001).

Ogawa E.T., Lee K.-D., Matsuhashi H., Ho P.S., Blaschke V.A., Havemann R.H., *Journal of Electronic Materials*, **31** (10), 1052-1058, (2002a).

Ogawa E.T., Lee K.-D., Blaschke V.A., Ho P.S., *IEEE Transactions on Reliability*, **51** (4), 403-419, (2002b).

OMEGA Engineering, Inc., One Omega Drive, Stamford, Connecticut 06907, USA, *www.omega.com*.

Proost J., Hirato T., Furuhara T., Maex K., Celis J.-P., *J. Appl. Phys.* **87** (6), 2792-2802, (2000).

QualiTau, Inc., 915 Walsh Avenue, Santa Clara CA 95050, USA, *www.qualitau.com*.

Rosenberg R., *J. Vac. Sci. Tech.*, **9**, 263, (1972).

Rosenberg R., Edelstein D.C., Hu C.-K., Rodbell K.P., *Annu. Rev. Mater. Sci.*, **30**, 229-262, (2000).

Ryu C., *Ph.D. Dissertation*, Stanford, 1998

Sommer J., Muschik T., Herzig C., Gust W., *Acta.mater.* **44** (1), 327-334, (1996).

Tao J., Cheung N.W., Hu C., *IEEE Electron. Devices Lett.*, **14**, 149-251, (1993).

Thompson C.V., Kahn H., *J. Electr. Mat.*, **22** (6), 581-587, (1993)

Towner J.M., *Proceedings of Int. Rel. Phys. Symp.*, 100-105, (1990).

Toyoda H., Wang P.-H., Ho P.S., *Proceedings of Int. Rel. Phys. Symp.*, 324-328, (1998).

Tracy D.P., Knorr D.B., *Journal of Electronic Materials*, **22** (6), 611-616, (1993).

Tu K.N., *J. Appl. Phys.* **94** (9), 5451-5473, (2003).

Vaidya S., Sinha A.K., *Thin Solid Films*, **75**, 253-259, (1981).

Vairagar A.V., Mhaisalkar S.G., Krishnamoorthy A., Tu K.N., Gusak A.M., Zaporozhets T., Meyer M.A., Zschech E., *AIP Conf. Proc. of Stress Induced Phenomena in Metallization: 7th Int. Workshop*, **741**, 135-148, (2004).

Vanasupa L., Joo Y.-C., Besser P.R., Pramanick S., *J. Appl. Phys.* **85** (5), 2583-2590, (1999).

Venkatesan S., Gelatos A.V., Misra V., Smith B., Islam R., *Proceedings of the International Electronics Devices Meeting*, 769-772, (IEEE, Washington, 1997)

Wang S.-Q., Suthar S., Hoeflich C., Burrow B. J., *J. Appl. Phys.* **73 (5),** 2301-2320, (1993).

Wong S.S., Cho J.S., Kang H.-K., Ryu S., *Mater. Chem. and Phys.*, **41**, 229-233, (1995).

Zschech E., Meyer M.A., Langer E., *Proc. of Mater. Research Soc. Symp.*, **812**, 361-372, (2004).

Vita

Meike Hauschildt was born in Neumünster, Germany, on June 4th, 1975, the second daughter of Helga and Karsten Hauschildt. After completing her Abitur at the Alexander-von-Humboldt Gymnasium in Neumünster, Germany, in 1994, she attended the Christian-Albrechts Universität in Kiel, Germany. She received her Vordiplom in Materials Science in 1996. In January 1998, she entered the Materials Science and Engineering program at The University of Texas at Austin, where she received a Master of Science degree in December of 1999. Subsequently, she continued her studies in the same program.

Permanent Address: Dorfstrasse 29
24582 Mühbrook
Germany

This dissertation was typed by the author.